Electromagnetic modeling of microstrip reflectarrays using scale changing technique

Farooq Ahmad Tahir

THÈSE

En vue de l'obtention du

DOCTORAT DE L'UNIVERSITÉ DE TOULOUSE

Délivré par :
Institut National Polytechnique de Toulouse (INP Toulouse)

Discipline ou spécialité :
Micro-ondes, Electromagnétisme et Optoélectronique
(Microwave, Electromagnetism and Optoelectronics)

Présentée et soutenue par :
FAROOQ AHMAD TAHIR

le : mercredi 14 septembre 2011

Titre :

Electromagnetic Modeling of Microstrip Reflectarrays using Scale Changing Technique

---

JURY

Pr. AUBERT Hervé , Pr. GILLARD Raphaël, Pr. MONEDIERE Thierry, Pr. TAO Jun-Wu,
Dr. PERRET Etienne, Dr. PONS Patrick

Ecole doctorale :
Génie Electrique, Electronique et Télécommunications (GEET)

Unité de recherche :
LAAS-CNRS

Directeur(s) de Thèse :

Pr. AUBERT Hervé

Rapporteurs :

Pr. GILLARD Raphaël, Pr. MONEDIERE Thierry

To my parents, brothers and sisters!

whose countless prayers, love, affection and great determination brought me to this point of honor

If you cannot be a poet, be the poem. David Carradine

Table of Contents

A man who is "of sound mind" is one who keeps
the inner mad-man under lock and key.
Paul Valéry

It takes courage to grow up and become
who you really are.
E.E. Cummings

ACKNOWLEDGMENTS

First and foremost my thanks go to Allah Almighty, the most Merciful, the most Beneficent, for He provided me with the capability and perseverance to do this job. My Lord! You have given me strength, satisfaction and joy while doing this research and blessed me since before I was born.

The subject of this thesis was performed in the Lab “Laboratoire d’Analyse et d’Architecture des Systèmes” of the “Centre National de la Recherche Scientifique” (LAAS-CNRS), Toulouse, the research team “Micro et Nanosystèmes pour les Communications sans fils” (MINC).

I am highly indebted to Hervé AUBERT, my thesis advisor, who has proposed this research topic to me and has rigorously followed and contributed to my research over the last three years of my thesis. I would like to thank him for his constant support, precious scientific discussions, providing me an excellent working environment and helping me to have better perspective in my scientific thinking. Hervé, thank you for your widespread availability throughout my thesis tenure. I offer my special thanks to you for your friendliness and good humor and the way you always focus on human relationship. In fact you have been a constant source of inspiration through both the highs and lows of my thesis. You will always be alive as a very kind and generous personality in my memories.

A lot of thanks to Prof. Robert PLANA, head of the MINC research team at the LAAS-CNRS for giving me the chance to be one of his team, for providing all needed equipments, material and software and for ensuring the harmony within the group.

I would also like to express my gratitude to Pr. GILLARD Raphaël (IETR/INSA, University of Rennes) and Pr. MONEDIERE Thierry (X Lim, University of Limoges) for agreeing to review my thesis as ‘rapporteurs’. I highly appreciate their in-depth review of this manuscript and acknowledging the work as an innovative and excellent progress in the domain of computational electromagnetics.

I am equally grateful to Jun-Wu TAO (INP-Toulouse), P.PONS (LAAS-CNRS), E. Perret (Ecole Nationale Supérieure en Systèmes Avancés et Réseaux, Grenoble) and C. Fabio (LAAS-CNRS, NovaMEMS) for accepting to be the part of the evaluation committee of my thesis defense. I highly appreciate their keen interest in my work as well as their precious comments and questions during the course of my defense.

I cannot forget the help and encouragement I got from my colleague Aamir Rashid during the first two years of my thesis. I thank him for helping me in understanding the theoretical concepts of Scale Changing Technique as well as the MATLAB code. I would also thank other colleagues Sami HEBIB, T. Euloge and Fadi for the help, discussions and collaboration regarding my research work.

I am equally indebted to Brigitte DUCROCQ (secretary Group MINC) for her excellent help in dealing with all the administrative stuff that allowed me to concentrate on my work.

I will always be grateful for the support and encouragement that I received from my colleagues of Group MINC. I am thankful to all of them for providing a healthy and friendly work environment. My special thanks go to Núria Torres, Tonio, and Badreddine and to my office mates (Aamir, Mai, Euloge, Dina, Céline and Olivier) for a great company and support.

I would like to offer my fondest regards to all my paternal and maternal family members. I am extremely grateful to my parents, my sisters and my brothers who always supported me and remained for me a constant source of courage, patience and inspiration. My father and mother have been counting days for many years for my return to home. My father will be very happy for realization of his dream for his son. Thank you my dear father for the example you have shown. You provided me with inspiration and instruction for how I live my life. My mother's continuous prayers had always given me a hidden support and confidence. I thank all those family members without whose encouragement and support, my PhD would have been an unfilled dream. A more loving thank to my younger sisters Iqra and Qurrah-tul-Ain (aka Sidra) for their funny anecdotes and family updates that kept my spirits high during the stressful times. I would not like to forget the sacrifices of my maternal uncle (RIP), if were alive, would have been very happy to see his nephew at his peak.

Special thanks to Muhammad Ali Nizamani and Tusawar Iftikhar for their hospitality and moments of relaxation and discussion I had the pleasure to share with them. I am very thankful to a number of my friends who have made my stay in Toulouse joyous and exhilarating. I would like to extend my thanks to Saif, Naveed, Saima, Hasnain, Subhani, Rameez, Saqlain, Nadeem, Saad, Kaleem, Awais, Gulfam, Usman, Inam, Abid, Tauseef, Mazhar, Tameez, Muazzam, Rashid, Zabit, Nafees, Umer, Iqbal and Khalid for such a great time. Finally, from the bottom of my heart, I thank all my friends and colleagues that were of great help to me at any stage during my stay in France.

Last but not least, I would like to acknowledge the financial support by Higher Education Commission Pakistan and National Scientific Research Center (LAAS-CNRS) France. None of this research would have been possible without their financial support.

The most exhausting thing in life is being insincere.
Anne Morrow

Originality is... a by-product of sincerity.
Marianne Moore

Abstract

Future antenna architectures especially for space applications are becoming more and more complex due to the need of reconfigurability. This reconfigurability is needed in terms of frequency, reliability, radiation pattern and power consumption. In this context, reflectarrays and frequency selective surfaces (FSSs) are particularly the hottest domains of RF design. The accurate analysis of electromagnetic (EM) scattering from such type of complex finite-sized reflectarray antenna structures is of great practical interest. However due to their large electrical size and complex cellular patterns specially when tuning elements such as RF-MEMS are also integrated within the array elements, conventional full-wave EM analysis of such multiscale structures either fail or require enormous amount of computational resources to resolve prohibitively large number of unknowns. Moreover the characterization of large structures would normally require a second step for optimization and fine-tuning of several design parameters, as the initial design procedure assumes several approximations. Therefore a full-wave analysis of the initial design of complete structure is necessary prior to fabrication to ensure that the performance conforms to the design requirements. A modular analysis technique which is capable of incorporating geometrical changes at individual cell-level without the need to rerun the entire simulation is extremely desirable at this stage.

An indigenous technique called Scale Changing Technique (SCT) addresses this problem by partitioning the cellular reflectarray geometry in numerous nested domains and sub-domains defined at different scale-levels in the array plane. Multi-modal networks, called Scale Changing Networks (SCNs), are then computed to model the electromagnetic interactions between any two successive partitions by method of moments (MoM) based integral equation approach. The cascade of these networks allows the computation of the equivalent surface impedance matrix of the complete array which in turn is utilized to compute far-field radiation patterns. Full-wave analysis of both passive and active (electronically tunable by RF-MEMS) reflectarrays has successfully been performed by the SCT while utilizing very small amount of computational resources as compared to conventional full wave methods. Moreover, to speed up the SCT modeling of the reflectarrays, equivalent electrical circuit models have been extracted and applied for individual design and optimization of the reflectarray phase shifter elements.

Man is least himself when he talks in his own person.
Give him a mask, and he will tell you the truth.
Oscar Wilde

Be who you are and say what you feel, because those
who mind don't matter and those who
matter don't mind. Dr. Seuss

Duty is what one expects from others.
Oscar Wilde

In the confrontation between the stream and the rock, the stream always wins, not through strength but by perseverance. H. Jackson Brown

1

Introduction

1.1 Reflectarray Antennas

In a great number of RF and microwave applications (both in the domains of terrestrial and satellite communications) a highly directive antenna with a main beam scanned to a certain angle is required. To achieve this, a certain aperture illumination with progressive phasing is used. The two primary ways to do this are reflectors and arrays as shown in Figure 1.1 with advantages/disadvantages of each type. Although the conventional phased arrays provide high gain and directivity, yet at the same time they need very complex beam-forming networks and costly transmit/receive modules. Also the reconfigurable antennas based on active antenna architectures are extremely handicapped by their large mass and high cost. They are therefore not well-suited especially to the telecommunication market. The reflector antenna uses its geometry to create the desired phase across the aperture, while the array employs distinct elements fed with progressive phasing. Reflector antennas are advantageous in the fact that they typically exhibit large bandwidth and low loss. The main disadvantage of the reflector is the geometrical constraint it imposes on the design. The most popular reflector, the parabolic reflector, also exhibits inherently high cross polarization levels. Obviously, it would be beneficial to combine some of the more attractive features of reflectors and arrays. This is accomplished by the reflectarray shown in Figure 1.1.

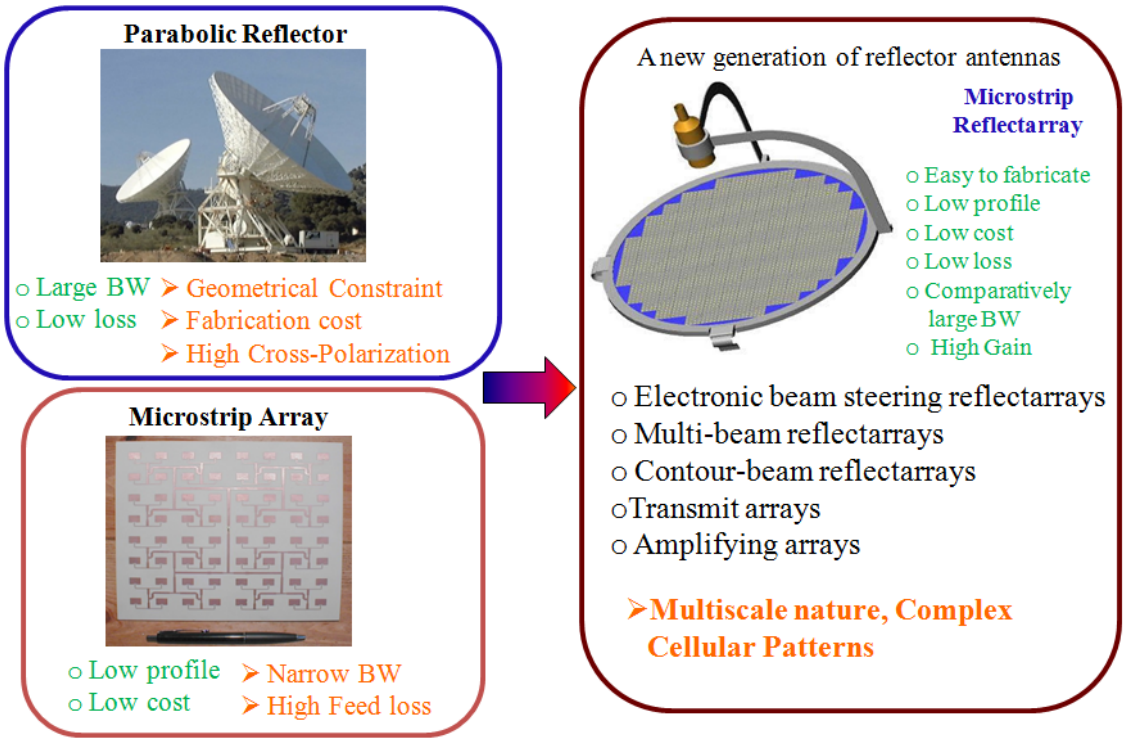

Figure 1.1: Examples of reflector, microstrip array and reflectarray antennas

Reflectarrays is a class of antennas that utilizes arrays of elementary antennas as reflecting surfaces and was first introduced in 1963 by Berry [1]. It has been found that the Reflectarray combines much of the simplicity of the reflector-type antenna with performance versatility of the array-type. A reflectarray is an array of antennas which is illuminated by a primary feed horn instead of high loss conventional transmission line feeds. The elements of the reflectarray receive and then reradiate the incident energy of the feed horn with a given phase determined by the phase-shifting device attached to the element.

1.2 Microstrip Reflectarrays

Reflectarrays in the past have used waveguides as the array elements. However waveguides or other conventional antennas are relatively bulky and expensive to manufacture. An appealing option is to use a microstrip antenna like a patch antenna as the array elements due to its compactness, simple packaging requirements, conformal abilities and low manufacturing cost. The microstrip reflectarrays can be easily mounted on roofs and

walls for wireless communications and broadcasting. Hence they are greatly being employed in spacecraft applications for their low profile and ease of deployment.

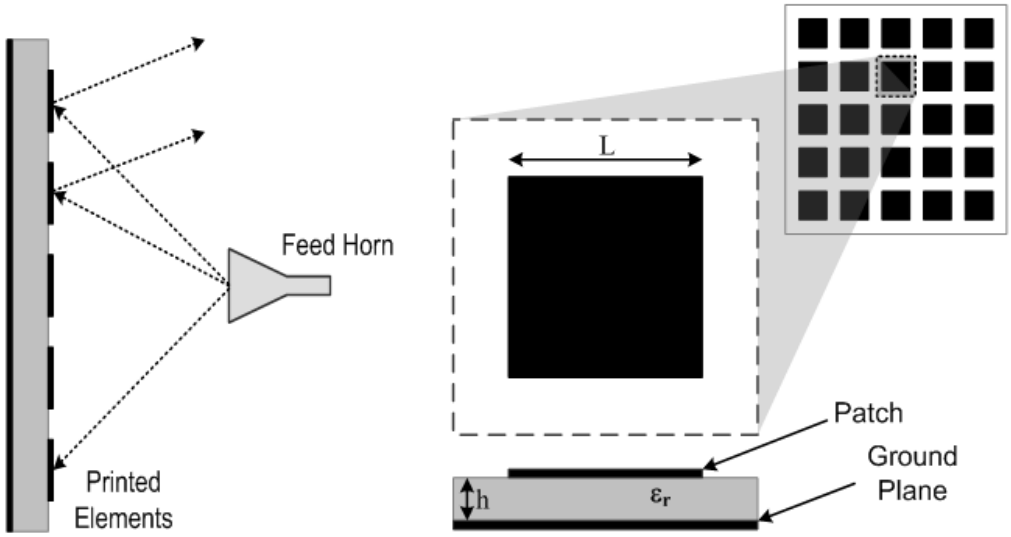

Figure 1.2: A standard microstrip reflectarray antenna

A standard microstrip reflectarray as shown in Figure 1.2 consists of array of microstrip patches printed on a thin-grounded dielectric substrate whose role is to convert a spherical wave produced by a feed, such as horn antenna, into a plane wave using a suitable phasing mechanism. Each element of the reflectarray re-radiate the incident wave with a given phase shift, that is why each unit cell of the microstrip reflectarray is called "phase shifter". The purpose behind this type of antenna is to obtain a highly directive reflected beam scanned to a certain angle without changing the position of the feed horn. This angle is controlled by the different geometrical parameters of the phase shifting cell.

1.3 Electronically Tunable Microstrip Reflectarrays

Initially developed microstrip reflectarrays consisted of only passive[1] cells, in this case the direction of the radiated beam is fixed and the desired fixed beam direction is obtained

[1]Passive in the sense that the cells do not have any incorporated electronic devices (e.g., PIN diodes, RF-MEMS) for dynamic phase control to achieve radiation pattern reconfigurability.

for example by using patches of variable sizes or identical patches with stubs of variable lengths or by varying the height of the substrate. A more recent trend to design reconfigurable reflectarrays is by employing active phase shifting cells. Figure 1.3 presents a reflectarray antenna that can be electronically reconfigured to steer the radiated beam in the desired directions. For such type of electronically tunable reflectarrays, the radiation pattern is not fixed and it is possible to achieve dynamic phase control by introducing electronic tuning elements as explained in the next section.

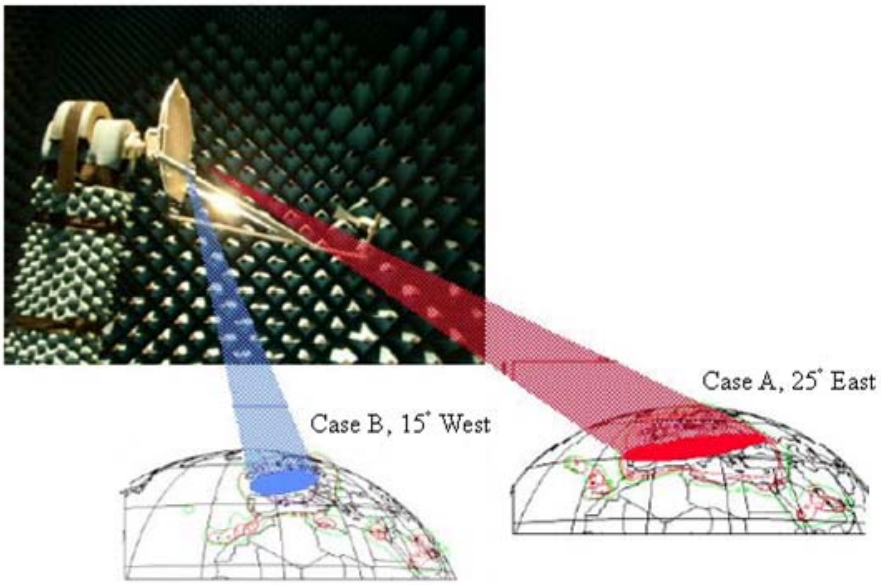

Figure 1.3: Depiction of an electronically reconfigurable reflectarray antenna [2]

From the time the microstrip reflectarray was first demonstrated [3], many different phasing schemes for a microstrip reflectarray have been introduced. These include, as shown in Figure 1.4 (a), variable size microstrip patches [4], variable size dipoles [5], identical microstrip patch elements with variable length phase delay lines with or without angular rotations [6]–[7] and patches of variable size loaded with slots of different sizes [8].

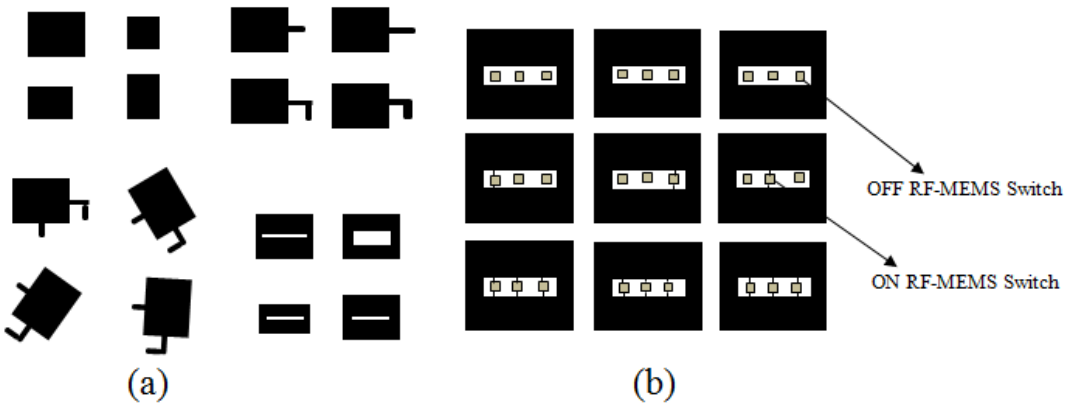

Figure 1.4: (a) Various approaches for phase tuning of the reflectarray. (b) Reflectarray implementation with RF-MEMS switches as phase tuning elements (all the reflectarray elements have similar physical structure and orientation)

In all the above mentioned approaches, the steering of the reflected beam (in a particular fixed direction) is achieved by changing the physical size (geometry) of the structure and/or orientation, hence dynamic phase control is not possible by these techniques. This is where the concept of reconfigurability (dynamic beam steering) enhances the design of a microstrip reflectarray. Different electronic techniques have been recently investigated for microwave reconfigurability such as, using PIN diodes [9], varactor diodes [10], ferroelectric thin films [11], liquid-crystals [12], photonically controlled semiconductors [13] and RF-MEMS [14-16]. Among the above techniques, the most promising technology is of RF-MEMS due to their excellent RF properties such as low power consumption, high linearity, low loss and high isolation. By having similar physical structure for all the reflectarray elements as shown in Figure 1.4(b), different reflection phases can be obtained by electronic manipulation of the MEMS switches. MEMS technology can be integrated into reflectarray design to achieve a higher degree of functionality in a very straight forward manner. The other advantage of such integration is that MEMS based reflectarrays can be processed at large scale with a low cost industrial process.

There is an increasing need for such electronically tunable antennas especially in satellite telecommunications systems. The first need, identified for low earth orbit (LEO) satellite systems, has been intensively considered during the past decade. Scanning beams are needed for the production of fixed spot beams on the ground from an LEO satellite. For GEO (geosynchronous earth orbit) satellite systems associated to commercial missions, the required life duration in orbit is from 15 to 18 years. It means that the antennas coverage must be frozen around 20 years before the end of their mission. During such a long time, the

demand in data traffic (TV broadcast; phone, video or data transmission, multimedia direct-to-home, etc….) are subject to significant change. An antenna able to change its coverage in-flight is therefore very attractive for operators.

The satellite antenna reconfigurability (beam scanning, adaptive radiation pattern) achieved by active phased arrays suffer from high complexity, high mass, high volume and high power consumption. Such drawbacks restrict their use to specific applications such as earth surveillance or military telecommunications, and make them not economically efficient for the telecommunication market. Novel reconfigurable antenna solutions with dramatic cost reduction may arise by integrating the MEMS technology in the radiating elements of the antenna. Thanks to the miniaturization of electronic modules provided by MEMS technology, it becomes possible to merge both electronic and radiating functions.

1.4 Computational Electromagnetics and Microstrip Reflectarrays

The accurate prediction of electromagnetic (EM) scattering from large finite-sized microstrip reflectarrays is of great practical interest in the domain of design and optimization of modern reflectarrays, transmit arrays, and frequency selective surfaces (FSSs). However, due to their large electrical size and complex cellular patterns specially when tuning elements such as RF-MEMS are also integrated within the array elements, full-wave EM analysis of such multiscale structures requires enormous amount of computational resources to resolve prohibitively large number of unknowns. Moreover the characterization of large array structures would normally require a second step for optimization and fine-tuning of several design parameters as the initial design procedure assumes several approximations. Therefore a full-wave analysis of the initial design of complete structure is necessary prior to fabrication, to ensure that the performance conforms to the design requirements. A modular analysis technique which is capable of incorporating geometrical changes at individual cell-level without the need to rerun the entire simulation is extremely desirable at this stage.

Historically several approaches have been followed when analyzing large planar structures. In the case of uniform arrays where periodicity in the geometry exists, an infinite array approach is often applied [17], [18]. In this case, the entire computation domain is effectively equivalent to solving for a single unit-cell by using set of Floquet harmonics; thus significantly reducing the number of unknowns and hence the execution times and memory

resources. Although the periodic boundary conditions take the effect of mutual coupling into account in the periodic environment, the approximation may not hold for the arrays where individual cell geometries are quite different. In addition, this is a very poor approximation for the cells lying at the edges of the array [19]. Different conventional full-wave simulation techniques based either on spatial discretization (e.g., finite element method) or spectral discretization (e.g., mode matching technique) have been applied for complex multiscale and multilayered structures [20], [21]. But all of these methods would require prohibitive execution time and memory resources for the cases where the local periodicity assumption cannot be applied. Especially, in the case of doubly truncated arrays, both the transform variables become continuous and the evaluation of the matrix elements containing integrals instead of summations becomes a considerably time consuming process [21], [22]. Moreover, any geometrical change at individual cell-level, e.g., during the design and optimization process, requires to rerun the entire EM simulation and consequently these well-known numerical techniques imply prohibitive execution times and memory resources. Although the electromagnetic coupling between unit cells in arrays can accurately be taken into account, these conventional approaches seem not to be appropriate for rapid array-design and optimization purposes.

To render large problems manageable, it is common to apply asymptotic techniques, such as the geometrical theory of diffraction (GTD) [23] or physical optics (PO) [24]. However, basic difficulties arise in using these techniques when one deals with the structures having fine details and, hence, the conditions of validity for the asymptotic methods are violated by their geometries. To overcome this limitation, hybridization of the method of moment (MoM) with asymptotic techniques, ray-based (like GTD), or current-based (like PO) methods have been proposed [25]. However, these approaches have only seen limited applications because of the difficulties in finding a systematic way to merge the two methods. Recently, promising improvements for MoM type scattering analysis of large-scale structures have been developed, e.g., the impedance matrix localization, the pre-corrected Fast Fourier Transform, the Fast Multipole Method and its extension, the Multilevel Fast Multipole algorithm [26]-[29]. Although these techniques are able to address large body problems in a highly efficient way, the convergence of numerical results remain delicate to reach systematically and also the methodology is still limited by the discretization size ranging from 10 to 20 basis functions per wavelength [30].

The generalized sparse matrix reduction technique and the characteristic basis method of moment have also been proposed for solving numerical problems generated by the electromagnetic simulation of multi-scale objects [31]-[32] however, the construction of characteristic basis functions for expanding the unknown current on such objects may be very time consuming and may require in practice large memory storage capabilities. Finally, the electromagnetic simulation of multi-scale structures may also be performed by the combination or hybridization of various numerical techniques, each technique being the most appropriate for a particular scale level. However such coupling between heterogeneous formulations or the interconnection of various simulation tools is very delicate in practice. A spectral domain immittance approach has also been applied for the full-wave analysis of a small planar dipole array along with the Galerkin procedure using entire domain basis functions [33]. But still this approach is limited to full wave modeling of microwave integrated circuits and simple arrays. Moreover, the approach has limitations, such as, it requires infinitesimal thickness for the strip conductors, the structures having finite conductivity are difficult to treat by this technique and also there should be no substrate discontinuity in the sideward direction [34]. The technique also shares the same time consuming recalculation process of Green's impedance functions when any geometrical change occurs at the unit cell level.

1.5. Scale Changing Technique (SCT)

In order to overcome the above-mentioned theoretical and practical difficulties, an original monolithic formulation called *Scale Changing Technique* (SCT) has been recently proposed and developed for handling large multiscale 2.5D structures [35]. The SCT is a very efficient technique in terms of time and memory as compared to the above discussed conventional numerical electromagnetic methods. The power of this technique comes from the modular nature of its problem formulation. Instead of modeling the whole planar-surface as a single large discontinuity problem, it is split into a set of many small discontinuity problems each of which can be solved independently using modal method (see, e.g., [36] for detailed modal analysis of discontinuities in waveguides). Each of the sub-domain discontinuity solution can be expressed in the matrix form characterizing a multiport-network called *Scale Changing Network (SCN)*. SCT models the whole structure by interconnecting all scale changing networks, where each network models the electromagnetic coupling

between adjacent scale levels. The cascade of the scale changing networks allows the global electromagnetic simulation of all sorts of multi-scale planar geometries.

The global electromagnetic simulation of multiscale structures via the cascade of scale changing networks has been successfully applied to the design and electromagnetic modeling of structures having diverse geometries such as multi-frequency selective surfaces [37], discrete self-similar scatterers [38], [39], active patch antennas [40] and MEMS-reconfigurable planar phase-shifters [41]. The SCT has also been recently applied by the author for the electromagnetic modeling of free-standing finite size planar structures under feed horn excitation [42], periodic microstrip reflectarrays [43], free-standing finite-sized reflectarrays without dielectric loading [44] and finite-sized thick frequency selective surfaces [45].

Here, it is important to mention about another modular approach based on spectral-domain Method of Moments that has been used in the case of multilayer periodic structures [46] which consists of characterizing each array layer by a generalized scattering matrix (GSM) and then analyzing the complete structure by a simple cascade of these GSMs. SCT differs from this approach because in case of SCT partitioning is applied to the same array-plane and therefore SCT is applicable for single-layer array problems. For multilayer arrays, SCT can be used in hybrid with the fore-mentioned approach for the efficient modeling of more complex electromagnetic problems e.g. in the case of variable sized stacked patch-arrays [47]-[49] and aperture-coupled arrays [50]-[51].

1.6. Objectives and Contributions

The objective of this research work is to benchmark Scale Changing Technique in cases of finite-sized uniform (with all cells identical) and non-uniform (having non-identical cells) microstrip reflectarrays. The non-uniform microstrip reflectarrays are designed to steer the beam into a specific direction. Analytical modeling of pyramidal horn has also been presented to incorporate the feed horn excitation into the electromagnetic (EM) formulation of Scale Changing Technique. The microstrip reflectarrays studied in this thesis are consisting of passive (i.e., having no built-in electronic devices for dynamic phase control) elements containing patches loaded with slots. A small reconfigurable reflectarray electronically tunable through RF-MEMS switches has also been modeled and simulated by the SCT. These RF-MEMS switches allow dynamic phase control of the re-radiated beam by

the microstrip reflectarray. The modeling and simulation of this 4-element active reflectarray will pave the way towards SCT modeling of larger 2D reflectarrays electronically reconfigurable by RF MEMS switches. The scattering parameters and far-field radiation pattern results obtained by the SCT for all the above mentioned active and passive reflectarrays are then validated using standard simulation tools based on finite element method and method of moments.

The second very important research contribution but presented in the first Section of the thesis (Section I) is the extraction of the equivalent circuit models for two types of phase shifter elements of the microstrip reflectarrays, these are:

- **Passive phase shifter cells, i.e., unit cells containing only patch and slot.**
- **Active phase shifter cells i.e., unit cells containing patch and slot loaded with RF-MEMS switches.**

These equivalent circuit models are then used as a time and memory efficient tools to design and optimize the reflectarray elements individually (Section I), and then in Section II the reflectarrays based on these optimized phase shifter elements are simulated by the Scale Changing Technique. The application of the circuit models allow rapid computation of the frequency response for the design and optimization of individual microstrip reflectarray unit cells.

In brief, this research work presents two efficient methods in the form of equivalent electrical circuit models for the design and optimization of the individual reflectarray elements (Section I) and then the Scale Changing Technique (SCT) for the electromagnetic modeling of the reflectarrays as a whole (Section II).

1.7. Structure of the Thesis

This thesis is divided into two main Sections, I and II. Section I consists of chapters 2 and 3. Chapter 2 presents the geometry of the reflectarray phase shifter cell finally loaded with RF-MEMS switches, the methodology for the extraction of its equivalent electrical circuit and then how this circuit model can be applied as a design and optimization tool for determining specific unit cell configurations that allow synthesizing a uniform distribution of a given number of phases over 360° phase range. Chapter 3 will concentrate primarily on the MEMS switch losses with in the reflectarray unit cells. In this chapter, the main focus is on the strategy of reducing the power losses in the phase shifter cells and making the circuit

model more flexible and useful regarding capacitance ratio (C_{ON}/C_{OFF}) of capacitive RF-MEMS switches. This chapter also discusses the effect of the switch position on the power losses and the advantage of the redundancy among the switch positions.

In Section II, chapter 4 explains the theory behind the Scale Changing Technique (SCT) in a general context using an example of a generic discontinuity plane. Several concepts related to the technique are introduced and elaborated. How a multiscale discontinuity problem can be expressed in terms of equivalent electromagnetic circuit components has also been demonstrated. The problem is then formulated in terms of matrix equations and solved using MoM based technique. Chapter 5 demonstrates the application of the SCT to periodic reflectarrays. In chapter 6, the Scale Changing Technique is used to model finite uniform and non-uniform planar reflectarrays under plane wave incidence and horn antenna excitation. A small electronically reconfigurable reflectarray has also been simulated by the SCT. In this chapter it has been shown that the SCT can effectively models the electromagnetic coupling between the neighboring cells of an array. The simulation results as well as the simulation times are compared to the classical simulation tools. The scattering field plots in case of SCT are compared to the results obtained by the other techniques.

God has given you one face, and you make yourself another.
William Shakespeare

Section I

Equivalent Electrical Circuit Model for Design and Optimization of Microstrip Reflectarray Unit Cells

He who trims himself to suit everyone will soon whittle himself away.
Raymond Hull

2

Extraction of Equivalent Electrical Circuit Model for Reflectarray Phase Shifters

2.1. State of the Art

In recent years electronically tunable microstrip reflectarray antennas have become a potential candidate in the domain of antenna technology. As it has been discussed in chapter 1 that the reconfigurable reflectarrays possess the advantages of both fixed beam reflectarrays (such as small size, less weight and low cost) and active phased arrays (e.g., beam scanning, adaptive radiation pattern and dynamic phase control). These attributes have made them in recent years a more significant and attractive antenna technology especially for satellite applications [2]. However, the above benefits are at the cost of high complexity in the reconfigurable microstrip reflectarray antenna structures. This complexity, in turn, becomes a severe handicap performing the electromagnetic (EM) modeling of reconfigurable reflectarrays by conventional numerical methods.

To offer an electromagnetic model for such structures that could be simple and useful for designers, equivalent circuit approaches are helpful. In the past, On the basis of basic circuit modeling equations, originally presented by Marcuvitz [52], many equivalent circuit models have been derived for different kinds of periodic non-reconfigurable frequency selective

surfaces (FFSs) and reflectarray antennas [53]-[56]. As for as the equivalent circuit approach for the design of reconfigurable reflectarrays is concerned, recently, an equivalent electrical circuit [10] based on the transmission line model [57] is presented to analyze the scattering behavior of an electronically tunable varactor-based phase shifter cell. This phase shifter cell consists of two rectangular patches separated by a slot loaded with two varactor diodes at the edges as shown in Figure 2.1.

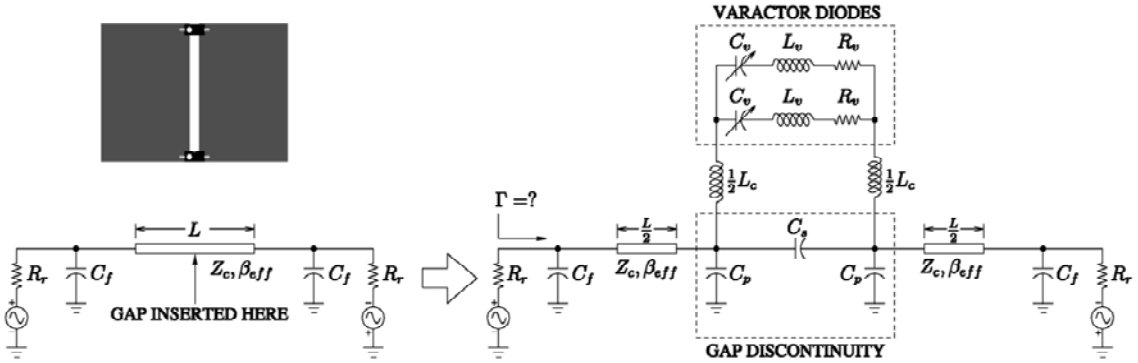

Figure 2.1: Equivalent circuit for predicting reflectarray cell scattering (a) Standard microstrip patch (b) Microstrip patch with varactor diode and discontinuities [10]

The working principle of this unit cell shown in Figure 2.1 (a) is simple; by varying the capacitance of the diodes, the resonance frequency of the unit cell is changed. In turn, this change in the resonance frequency directly controls the reflected phase of the radiating element. This principle is applied to all reflectarray elements to scan the overall reflectarray beam in the desired direction.

The equivalent circuit of Figure 2.1 (b) has its origins in the basic transmission line model of a microstrip antenna [8]. Using transmission line model a rectangular microstrip patch can be represented by two parallel radiating slots (i.e., two radiating edges of the patch) of admittance equal to the sum of the radiation resistance and the edge capacitances [57]. For the cell of Figure 2.1 (a), each patch is then represented by a line of length L/2, characteristic impedance Z_c and effective dielectric constant ε_{eff}. The slot is then seen as a discontinuity between two lines and is modeled by an equivalent π network. In parallel to this circuit, the two series RLC circuits represent the varactor diodes. Finally, an inductance is added in series to reflect the effect of the current flowing in the diodes. The extraction of model parameters has been made directly from the results of full wave electromagnetic simulations

carried out using FDTD (Finite-Difference Time-Domain) method [10].

Although the proposed circuit is simple, and its constituting elements are justified, this model does not seem much convincing, as in fact, a rectangular microstrip patch can be fed in different ways: by microstrip line, coaxial cable, or by an incident wave as is the case of a reflectarray. The transmission line model can be best suited for the first two types of excitation as compared to the case of incident wave. In fact, the incident wave first sees the patch and then propagates in the dielectric to be reflected from the ground plane; so a model is needed that represents the scattering behavior (in respect of both transmission and reception) of the phase shifter cell in a more rigorous manner. Also in the circuit model representation of the slot, the electromagnetic interactions between the patches and the slot are not evident. The slot has been considered as a gap that simply puts the two variable capacitances (varactors diodes) in parallel, whereas for such structures, the most critical aspect is the electromagnetic coupling between the patch and the slot that has to be taken into account. Moreover, this circuit model cannot be used as a dynamic design tool as the number of command elements (varactor diodes) and their position is fixed.

A detailed loss budget (as discussed in [10]) of a reflectarray surface reveals that a significant source of loss in the electronically tunable reflectarrays is the power absorption by the tuning elements (the varactor diodes in the case of this design); such losses can be reduced by utilizing tuning components with a higher Q. In this context, among different techniques (one that is used here i.e., the varactor diodes, and others like PIN diodes, ferroelectric thin films, liquid-crystals, photonically controlled semiconductors and RF-MEMS), the most promising technology is of RF-MEMS due to their excellent RF properties such as low power consumption, high linearity, low loss and high isolation [58].

2.2. MEMS-Controlled Reconfigurable Reflectarray Phase Shifter Cell

In this thesis, for the first time, an equivalent circuit model is presented to design a phase shifter cell electronically tunable by RF-MEMS switches. After a careful study and systematic evaluation of different designs of the reflectarray unit cells, it was decided that a unit cell containing a patch loaded with a slot is best suited keeping in mind the RF-MEMS implementation within the slot. The slot acts as a load on the patch and by electronically varying the length of the slot (i.e., by making MEMS switches ON/OFF) the reflection phase tuning is achieved. The phase shifters of this kind have recently been developed and used in

reconfigurable reflectarrays [16], [58]-[60]. This equivalent electrical circuit model is flexible with respect to the state (ON/OFF), position and number of the command elements (RF-MRMS) and hence can be used as a dynamic design and optimization tool for reflectarray unit cells. The reflection phase obtained from this circuit model depends on the number, the ON/OFF state and the locations of the MEMS inside the phase-shifter cell. Moreover the circuit model has been used for determining, with a little computational effort, the locations and the minimum number of the MEMS that allow synthesizing a uniform distribution of a given number of phases at a single desired frequency within the operating frequency band of the reflectarray.

2.2.1. Geometry of the Phase Shifter Cell

A complete schematic diagram of the phase shifter cell loaded with MEMS switches is shown in Figure 2.2. All the geometric details of the unit cell are given in the caption.

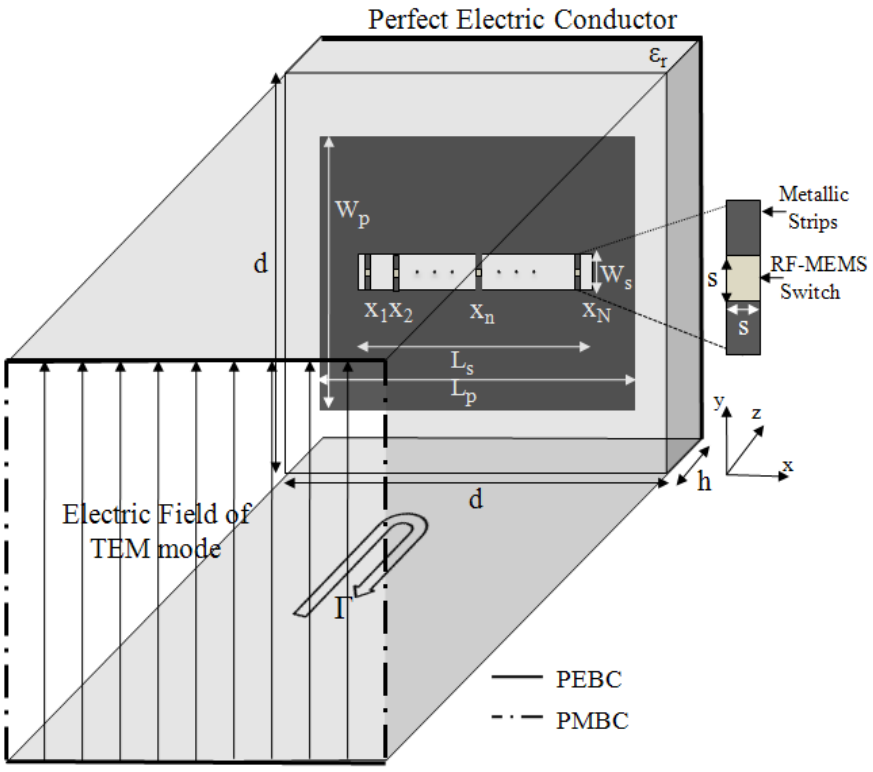

Figure 2.2: The phase-shifter cell in the TEM-mode waveguide: d=12mm, L_p=9mm, W_p=6mm, L_s=7mm, w_s=0.75mm, S=0.1mm, h=1.5mm and ε_r=2.9. MEMS switch is modeled by its equivalent surface impedance. The number of switches in the slot is denoted by N while x_n (n=1, 2… N) refers to the coordinate of the n^{th} switch in the slot. Metallic strips connect the switches to the patch. PEBC and PMBC stand for Perfect Electric and Perfect Magnetic Boundary Conditions respectively.

In the arrangement shown in Figure 2.2, the transverse electromagnetic mode (TEM) is the only one propagating mode within the frequency band from DC-14 GHz (this frequency band includes the frequencies from 11.7 GHz to 12.5 GHz which is the band at which the ultimate reflectarray has been designed under this research project). The number N and the locations x_1, x_2, x_3… x_N of the switches depend on the design requirements. The reflectarray phase shifter cell is placed at the end of a waveguiding structure of transverse dimensions d × d. The phase shift applied to the TEM mode when reflecting from the cell is assumed to be identical to that experienced by a plane wave electric field incident on a given cell [10]. The estimation of this phase shift or equivalently the phase of the reflection coefficient Γ through a simple equivalent circuit model is now presented. The dielectric and metallic losses within the unit cell are not taken into account in the present analysis.

2.2.2. Extraction Methodology of the Equivalent Circuit Model

The equivalent circuit is derived from step by step approach. First, in the set of Figure 2.2, replace the patch loaded with slot and MEMS by a simple metallic patch having the same dimensions $W_p \times L_p$ as shown in Figure 2.3.

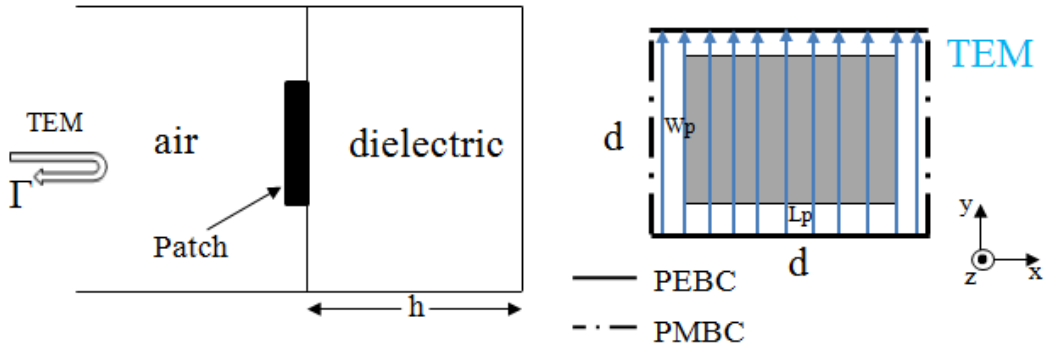

Figure 2.3: Simple Metallic Patch in d×d waveguide excited by TEM wave

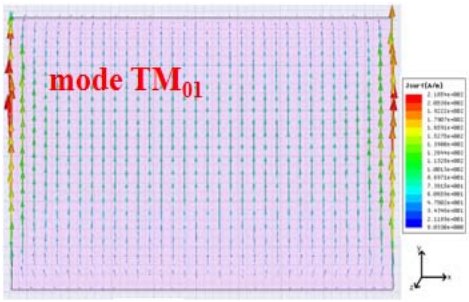

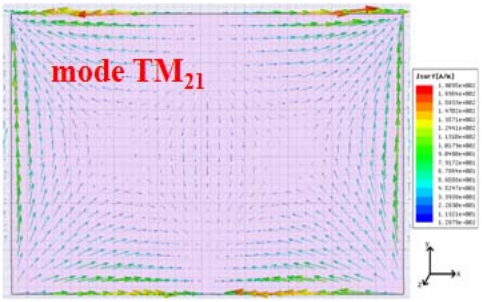

(a) (b)

Figure 2.4: Modes of patch resonances (a) Distribution of surface current at the patch surface at first resonance at 11.4 GHz (b) Distribution of surface current at second resonance at 22.8 GHz

Full-wave EM simulations of this simple patch and the analysis of surface current density on its surface (as shown in Figure 2.4) indicate that the two first resonant modes, i.e., the TM_{01} and TM_{21} contribute significantly to the value of the phase of the reflection coefficient within the frequency range (0- 25GHz).

The equivalent circuit of this simple patch is then given by two LC-series circuits (L_1C_1 and L_2C_2) connected in parallel and shunted by a short-circuited transmission line as shown in Figure 2.5.

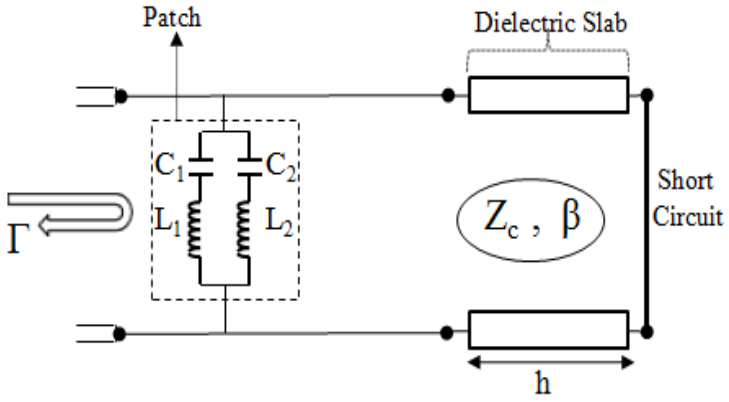

Figure 2.5: Equivalent electrical circuit model for microstrip patch

One LC-series circuit is associated with one resonant mode and the short-circuited transmission line models the dielectric slab of thickness h metalized on one side. The characteristic impedance of this line is $Z_c = Z_0/\sqrt{\varepsilon_r}$, where Z_0 denotes the free-space wave impedance and ε_r is the relative permittivity of the dielectric slab, the propagation constant β of the fundamental TEM-mode is $k_0\sqrt{\varepsilon_r}$ where k_0 is the free-space wave-number. From the above simulation results, the numerical values of the circuit elements L_1, C_1, L_2 and C_2 can be derived as follows:

(1) At 11.4GHz and 22.8GHz, the phase of the reflection coefficient is found to be zero making the magnitude of the reflection coefficient equal to 1 (i.e., open circuit, the input impedance equal to infinity). In other words we can say that the equivalent circuit resonates[1]

[1]The word "resonates" is just used as the input admittance of the circuit model is reduced to zero; do not mix up this resonance with the conventional resonance which turns the input impedance to zero.

at these frequencies turning the equivalent input admittance Y_{in} to zero (these two points can be called Zeros)

(2) At 16GHz and 24.75GHz, this phase is found to be π making the magnitude of the reflection coefficient equal to 0 (i.e., short circuit, the equivalent input impedance becomes zero). In other words the equivalent input admittance Y_{in} at these points becomes infinity (these two points can be called Poles).

From these two simulation results, a system of four independent equations combining the four unknowns (L_1, C_1, L_2 and C_2) is formulated as under:

The first two equations at first resonance and at first pole are given by:

At 1st resonance (f=11.4 GHz)

$$Y_{in} = \frac{1}{j\omega L_1 + \frac{1}{j\omega C_1}} - jY_0 \cot k_0\sqrt{\varepsilon_r}h = 0 \quad (2.1)$$

At 1st pole (f=16 GHz)

$$Z_{LC1} = j\omega L_1 + \frac{1}{j\omega C_1} = 0 \quad (2.2)$$

From the solution of these equations (2.1) and (2.2) , the values of two unknowns $L_1$and C_1 can be easily determined. Once the values of $L_1$and C_1 are known, the conditions of second resonance and second pole can be used to determine the values of L_2 and C_2 by the solution of the following two equations (2.3) and (2.4).

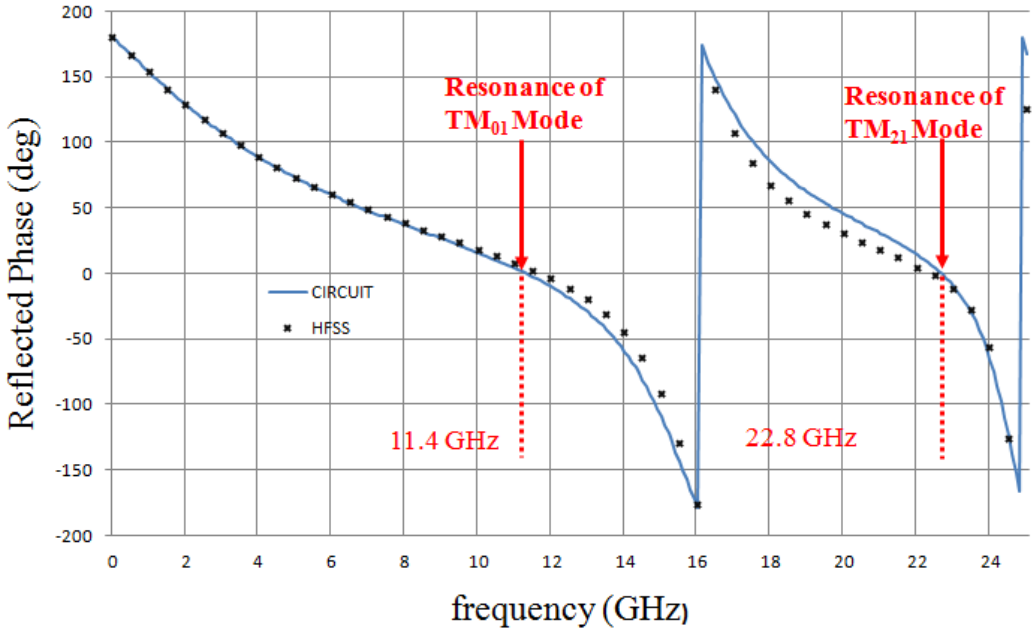

Figure 2.6: Comparison between the phases of the reflection coefficient obtained by equivalent circuit and HFSS

At 2nd resonance (f=22.8 GHz)

$$Y_{in} = \frac{1}{j\omega L_{p1}+\frac{1}{j\omega C_{p1}}} + \frac{1}{j\omega L_{p2}+\frac{1}{j\omega C_{p2}}} - j\,Y_r \cot g\, k_0\sqrt{\varepsilon_r}h = 0 \qquad (2.3)$$

At 2nd pole (f=24.7 GHz)

$$Z_{LC2} = j\omega L_{p2} + \frac{1}{j\omega C_{p2}} = 0 \qquad (2.4)$$

The values of L_1, C_1, L_2 and C_2 are reported in Table 2.1. For comparison purposes, the equivalent circuit model of Figure 2.5 and the microstrip patch backed with grounded dielectric of height h are simulated by ADS and HFSS respectively, the graphical results are in good agreement as shown below in the Figure 2.6.

Now the microstrip patch is loaded with slot. It was observed on the basis of full wave simulation results that the phase of the reflection coefficient can be accurately predicted within the frequency band of interest by connecting an LC-parallel circuit (L_sC_s) in series with the just derived simple patch circuit model of Figure 2.5. The equivalent circuit of the

patch loaded with a slot is given by the following Figure 2.7. From the simulations, it has come to know that the slot do not introduce any new resonance in phase results rather it translates the already present resonances of TM_{01} and TM_{21} modes towards lower frequencies.

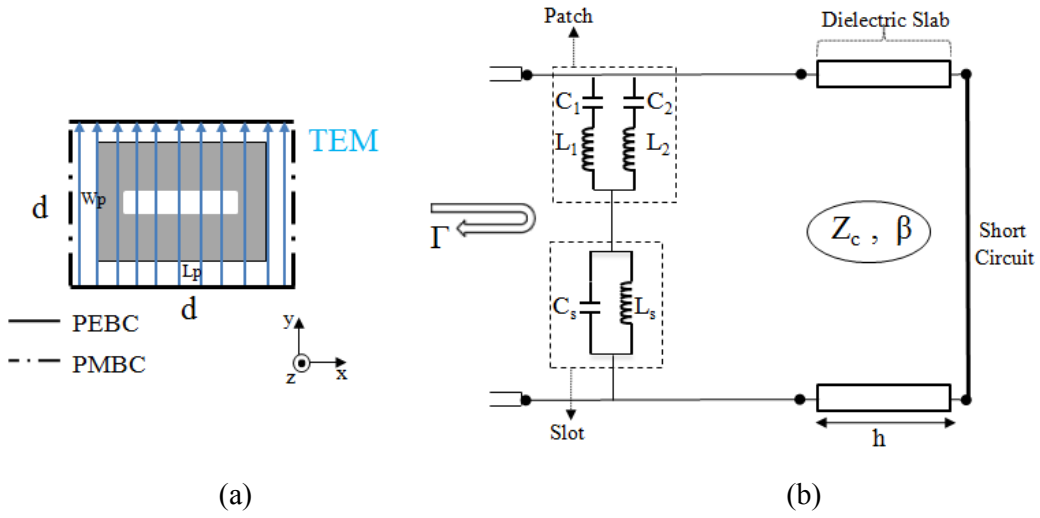

Figure 2.7: (a) Metallic Patch loaded with slot in d×d waveguide excited by TEM wave (b) Its equivalent electrical circuit model.

The values of L_s and C_s can be deduced by following two conditions:

(1) at 10.4GHz the phase of the reflection coefficient is found to be π (i.e., the equivalent circuit impedance is zero, a pole)

(2) at 18.45 GHz the phase is found to be zero (i.e., this frequency is the resonant frequency for the structure, a zero).

Applying these two conditions one can reach the values of L_s and C_s; these values are given Table 2.1.

Table 2.1

Values of the elements L_1, C_1, L_2, L_s and C_s appearing in the equivalent circuit of Figure 2.7

C_1(pF)	C_2(pF)	L_1 (nH)	L_2 (nH)	C_s (pF)	L_s (nH)
0.04	0.01	2.41	4.79	1.58	0.06

For comparison purposes, the equivalent circuit model of Figure 2.7(b) and the microstrip patch loaded with slot backed with grounded dielectric of height h are simulated by ADS and HFSS respectively, the graphical results are in good agreement as shown in Figure 2.8.

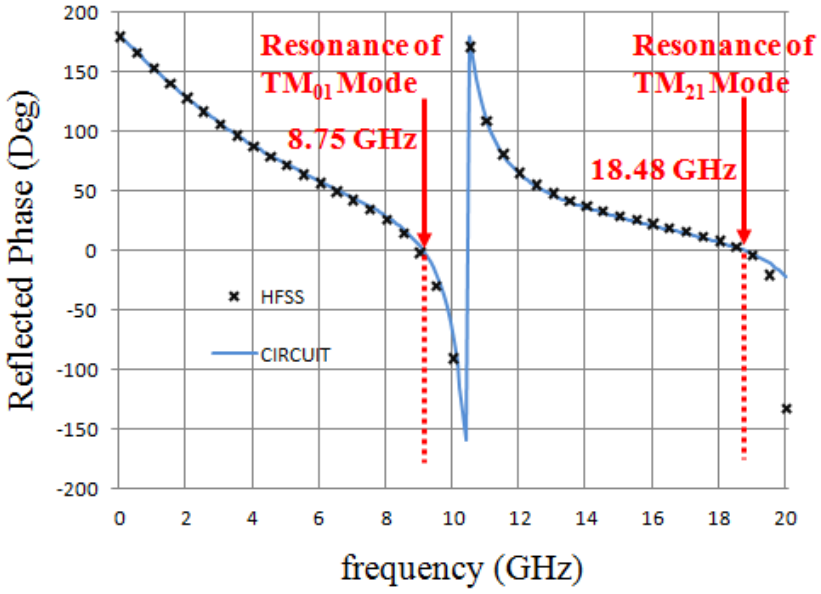

Figure 2.8: Comparison between the phases of the reflection coefficient obtained by equivalent circuit model of Figure 2.7(b) and HFSS

Next, load the slot *at its centre* by a single capacitive RF-MEMS switch. A capacitive MEMS switch generally has ON-state (C_{ON}) and OFF-state (C_{OFF}) capacitances in between 1-4pF and 20-50fF [61- 62] respectively. Moreover the typical loss resistance of such MEMS is in between 0.1 Ω and 1Ω (if such resistance is connected in series with the MEMS capacitance in the equivalent circuit, we observed that the phase diagram of the reflectarray element remains same as obtained in the lossless case). To model the MEMS including its connections, consider the MEMS *at the centre* of the slot denoted by the domain D_{MEMS} and the connections denoted by the domain D_M as shown in Figure 2.9(a).

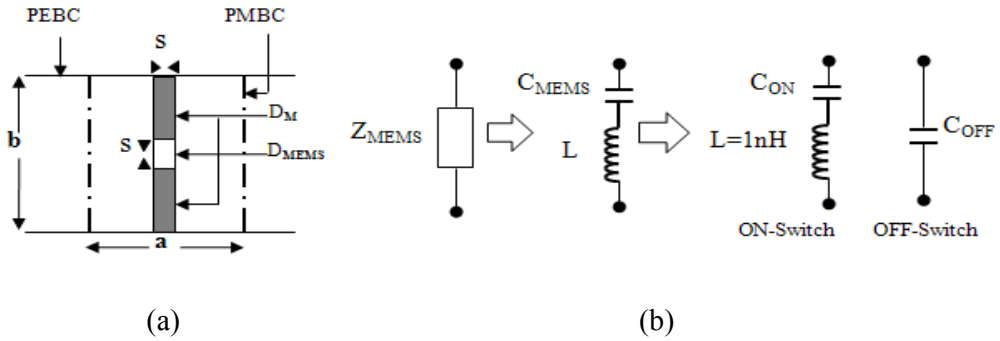

(a) (b)

Figure 2.9: (a) MEMS and its connections to the patch (b) equivalent circuit model when the MEMS switch is located at the center of the slot.

The MEMS and its connections can be modeled by purely reactive impedance Z_{MEMS} as shown in Figure 3(b), where C_{MEMS} (C_{ON} or C_{OFF}) designates the ON/OFF capacitance of the MEMS and L denotes the inductance of the domain $D_{MEMS} \cup D_{M.}$ This inductance can be estimated by equation (2.5) with b and s denote respectively the width of the slot and the width of the strip.

$$L = \mu_0 \frac{b}{a} \sum_{n=1,2,3,\dots}^{\infty} \frac{1}{\sqrt{(2n\frac{\pi}{a})^2 - {k_0}^2}} \operatorname{sinc}^2\left(n\frac{\pi}{a}s\right) \tag{2.5}$$

This approximation is derived from the application of the Integral Equation Technique using entire domain trial functions (for a description of this technique see, e.g., [63]). For deriving equation (2.5), a uniform trial function has been used for expanding the current density in the domain $D_{MEMS} \cup D_M$ and a uniform trial function has been adopted for describing the tangential electric filed in D_{MEMS}. In our application, s=100μm, a=7mm, b=750μm and central frequency is equal to 12.5GHz, where 'a' and 'b' are the dimensions of the entire domain where the trial functions are defined.

The inductance is then found to be close to 1nH. When the switch is OFF, this inductance can be neglected since $L\omega \ll 1/\omega C_{OFF}$, where C_{OFF} = 0.04pF. So the equivalent impedance Z_{MEMS} in this case is close to $1/\omega C_{OFF}$. Moreover, when the switch is ON, the impedance effect of the inductance L is not negligible and the equivalent impedance becomes equal to $\omega L + 1/\omega C_{ON}$ (see Figure 10(b)). Finally the equivalent circuit model for the phase-shifter cell when *the slot is loaded at its center by single MEMS* is then given in Figure 2.10. If the MEMS switch is located *at the edges of the slot*, it is shunted and consequently it does not participate in the phase-shift, i.e., the phase-shift in this case is provided only by the patch and slot. This situation can be modeled simply by removing the impedance Z_{MEMS} from the equivalent model of Figure 2.10.

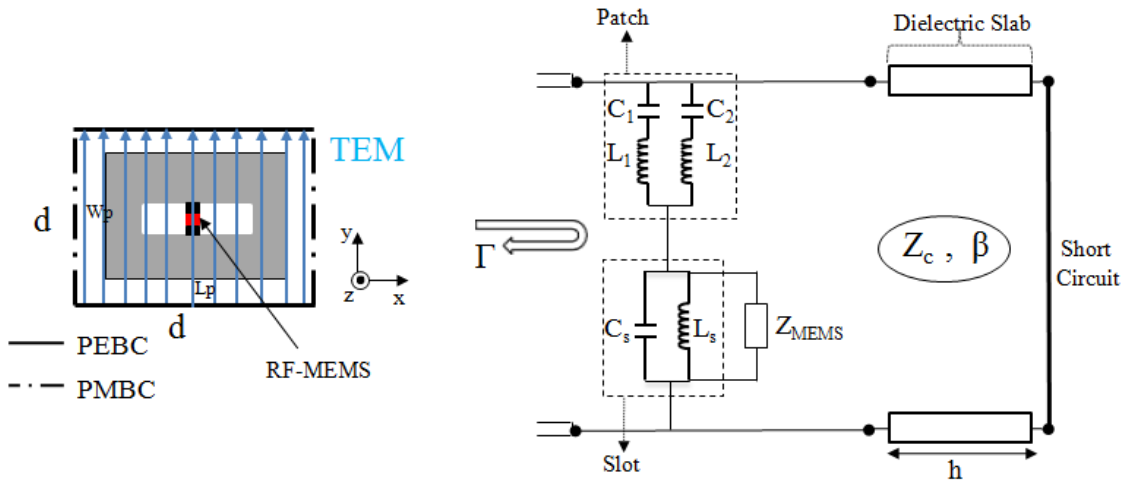

(a) (b)

Figure 2.10: (a) Metallic Patch loaded with slot with MEMS at its center (b) Its equivalent electrical circuit model.

Now in order to extract an equivalent circuit allowing the modeling of the cell having single MEMS *at an arbitrary location* between the edges and the center of the slot, we propose to connect a position-dependent impedance Z′(x) in series with Z_{MEMS} such that: (1) Z′ = 0 when the MEMS is at the center of the slot and (2) Z′ is infinite when the MEMS is at the edges of the slot. For an arbitrary location x of the MEMS between the edges and the center of the slot, the value of Z′ is extracted from full wave simulations. This impedance allows us to propose an electrical circuit that models a cell having *single MEMS* at an arbitrary location between the edges and the center of the slot. By full-wave simulations, we observe that when the MEMS is ON then,

$$Z'(x) = j\omega L'(x) \tag{2.6}$$

and when the MEMS is OFF then,

$$Z'(x) = 1/j\omega C'(x) \tag{2.7}$$

The variations of L′ and C′ versus the position x of the MEMS are reported in Figure 2.11(a) and (b) respectively. The corresponding value of L′ and C′ to a specific position is derived such that the phase of the equivalent circuit is very close to one given by full wave EM simulations. So the overall changing behavior of L′ and C′ along the length of the slot is

obtained under HFSS by taking 70 different positions of single MEMS inside the slot with the step of 0.1mm.

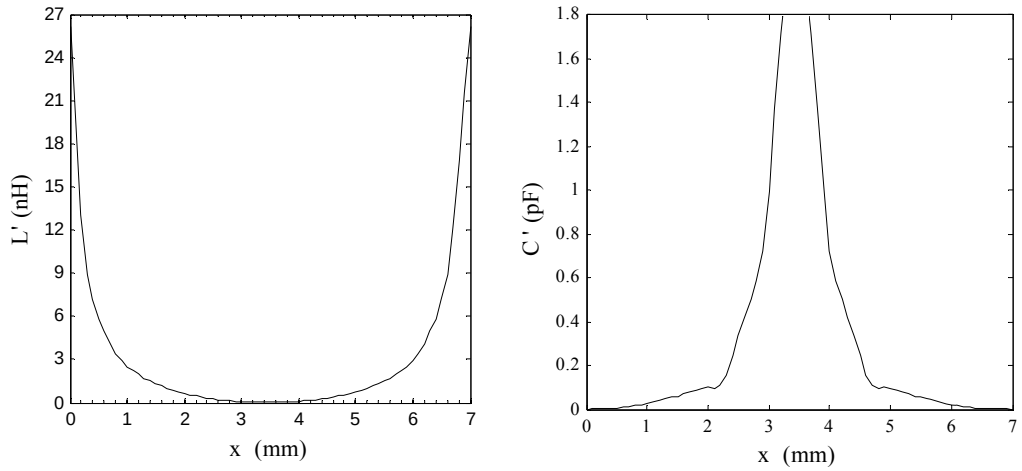

Figure 2.11: Variations of (a) inductance L′ and (b) capacitance C′ versus position of a single MEMS switch in the slot.

To generalize the one MEMS equivalent circuit model of the Figure 2.10(b) for the phase-shifter cell of Figure 2.2 having N (more than one) number of MEMS with coordinates x_1, x_2, $x_3 \ldots x_N$, we simulated the equivalent circuit on ADS taking different number of MEMS from 1 to 9 {with L_1, C_1, L_2, C_2, L_s, C_s and Z′(obtained from Figure 2.11) are those derived in case of single MEMS, i.e., no HFSS simulation involves to find circuit model for a phase shifter cell having more than one MEMS, rather it is derived from already extracted single MEMS model}. The results given by the equivalent circuit model are then compared with HFSS and are found to be in a very good agreement. As an illustration, Figures 2.13(a) and (b) give the results in case of three MEMS and five MEMS respectively.

Ultimately, the equivalent circuit of the phase-shifter cell having N number of MEMS is shown in Figure 2.12. The elements L_1, C_1, L_2, C_2, L_s, C_s and Z′ are those derived in case of single MEMS. The reflection coefficient Γ of the TEM mode when reflecting from the cell is then derived from the expression $\Gamma = (Z_L - Z_0)/(Z_L + Z_0)$, here Z_0 represents the characteristic impedance of input transmission line, we take its value equal to 50 Ω that is normally used as a standard and Z_L denotes the impedance of the one-port network of Figure 2.12(a).

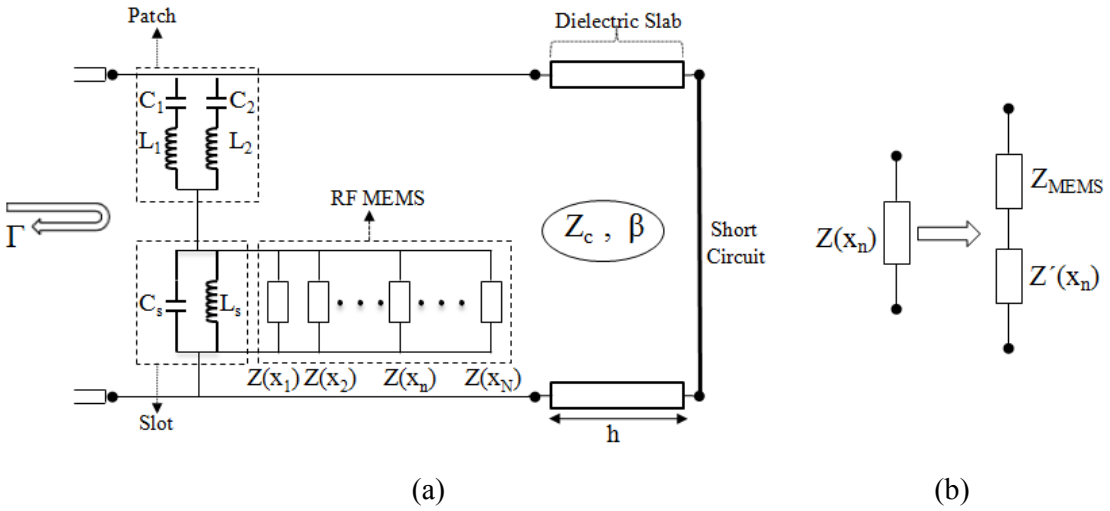

Figure 2.12: (a) Equivalent electrical circuit for a phase-shifter cell comprising of N MEMS; (b) Equivalent circuit model of the n^{th} MEMS within the slot (the total impedance $Z_{MEMS}+Z'$ depends on the ON/OFF state of the switch as well as its coordinate x_n inside the slot).

2.3. Design and Optimization based on the Equivalent Circuit Model

The equivalent circuit model extracted above is used as a tool for designing and specifically for optimization of the phase shifter cell loaded with MEMS. By using this circuit model we find such phase-shifter configurations that have 360° phase range at a single desired frequency with linear distribution of the selected phases and depend on the number N, the positions x1, x2, x3… xN and the state (ON/OFF) of the switches. To search out such phase shifter configurations out of thousands of configurations is not possible by full wave simulations due to time and memory limitations.

To find out the desired configurations, an algorithm based on the equivalent circuit model is developed, it selects the desired configurations from thousands of configurations (e.g., in case of three MEMS, the total configurations considered here are 70*69*68=328440, the switch scanning step within the 7mm slot is 0.1mm) which fulfill the criteria of the phase range and the linearity. The selected configurations then directly give the optimized values of the two important design parameters for the phase shifter cell, i.e., the number N and the locations x_1, x_2, x_3… x_N of the MEMS used.

The algorithm was first applied in two switch case (N=2) and it was observed that in this case, 360° phase range cannot be achieved within the desired frequency band (DC-14GHz). Therefore a higher number (N=3, 4, 5 …) of switches was used and found that the required conditions are now easily fulfilled. By this algorithm, a lot of configurations consisting of 3

to 9 switches have been determined which satisfy the design requirements and proves the practicality of the equivalent circuit. However in a very few configurations the equivalent circuit results are not consistent with those of HFSS (perhaps because our circuit model has some limitations and assumptions regarding boundary conditions and power losses as discussed in the previous Section), such particular cases can be rejected *a posteriori* from the selection.

Because of limited space, only the results for just four configurations selected by algorithm, two from 3-switch case (N=3) and two from 5-switch case, are presented here. The total number of phases or commands for 3 and 5 MEMS for one configuration is eight ($2^N=2^3=$ 000 … 111, the symbols "1" and "0" represent ON and OFF state of the switch respectively) and thirty two (2^5) respectively. As per design requirement, we need such configurations *at a single desired frequency within the operating frequency band* which cover linearly 360° phase range with four selected phases, i.e., about a 90° phase shift should be between each state. By using the algorithm, we found many configurations that fulfill the above criteria; here the results of four configurations are given. Table 2.2 presents the phase results at 13 GHz for 3 MEMS while Table 2.3 presents results for 5 MEMS at 11GHz. The results in both cases are in excellent agreement. Figures 2.13(a) and (b) show the response of two configurations (Table 2.2 (b) and Table 2.3 (b)) over the whole operating frequency range (DC-14 GHz).

Table 2.2

Phase-shifts at 13GHz, computed from the equivalent electrical circuit model and HFSS for phase-shifter cells loading by 3 RF-MEMS switches with (a) x_1=2.25mm, x_2=3.2mm, x_3 =6.65mm (b) x_1=0.45mm, x_2=2.25mm, x_3=6.45mm.

Command law	Phase Φ_{EC} by equivalent circuit model	Phase Φ_{HFSS} by HFSS	Linearity Check (The successive difference among four phases shifts)	Phase difference $\Phi_{EC} - \Phi_{HFSS}$
100	-164°	-175°	Reference Phase	11°
101	-77°	-80°	88°	3°
000	15°	19°	179°	4°
010	107°	100°	271°	7°

(a)

Command law	Phase Φ_{EC} by equivalent circuit model	Phase Φ_{HFSS} by HFSS	Linearity Check (The successive difference among four phases shifts)	Phase difference $\Phi_{EC} - \Phi_{HFSS}$
010	110°	104°	Reference Phase	6°
000	19°	21°	91°	2°
011	-76°	-67°	185°	9°
001	-164°	-174°	269°	10°

(b)

Table 2.3

Phase-shifts at 11GHz, computed from the equivalent electrical circuit model and HFSS for phase-shifter cells loading by 5 RF-MEMS switches with (a) x_1=0.75mm, x_2=3.45mm, x_3=6.15mm, x_1=6.45mm, x_1=6.65mm (b) x_1=1.75mm, x_2=0.25mm, x_3 =6.15mm, x_4=6.45mm, x_5=6.9mm

Command law	Phase Φ_{EC} by equivalent circuit model	Phase Φ_{HFSS} by HFSS	Linearity Check (The successive difference among four phases shifts)	Phase difference $\Phi_{EC} - \Phi_{HFSS}$
01100	166°	175°	Reference Phase	9°
00001	76°	70°	90°	6°
00010	-15°	-18°	181°	3°
00101	-105°	-95°	271°	10°

(a)

Command law	Phase Φ_{EC} by equivalent circuit	Phase Φ_{HFSS} by HFSS	Linearity Check (The successive difference among four phases shifts)	Phase difference $\Phi_{EC} - \Phi_{HFSS}$
11100	153°	154°	Reference Phase	1°
01000	63°	71°	90°	8°
11001	-27°	-28°	180°	1°
11010	-116°	-125°	267°	9°

(b)

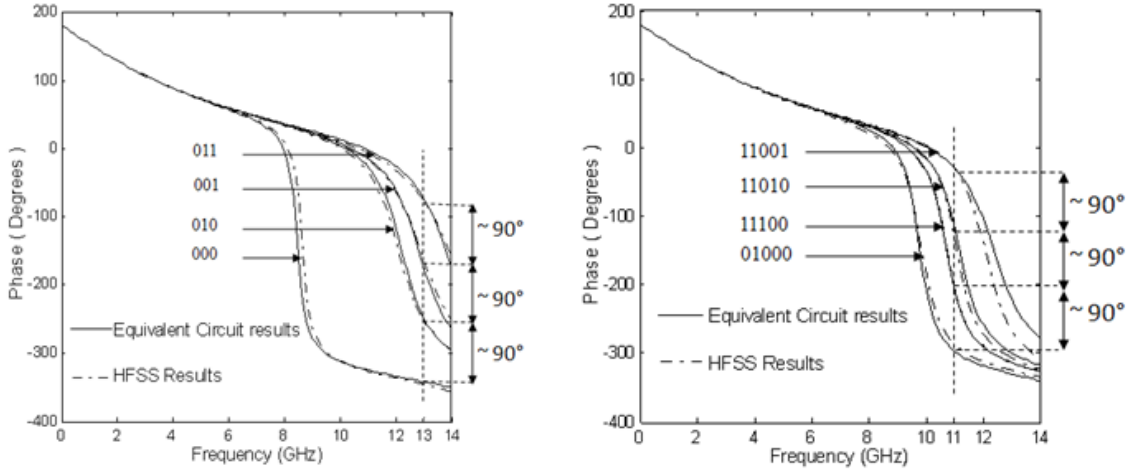

(a) (b)

Figure 2.13: (a)Comparison between equivalent circuit and HFSS results in three switch case under frequency range DC-14 GHz with x_1=0.45mm, x_2=2.25mm, x_3=6.45mm.The symbols "1" and "0" represent ON and OFF state of the switch respectively. (b) Comparison between equivalent circuit and HFSS results in five switch case under frequency range DC-14 GHz with x_1=1.75mm, x_2=0.25mm, x_3 =6.15mm, x_4=6.45mm, x_5=6.9mm. The symbols "1" and "0" represent ON and OFF state of the switch respectively.

2.4. Conclusions

This chapter presents a design and optimization tool in the form of an equivalent circuit for MEMS-controlled reflectarray phase shifter cells. The results given by the equivalent electrical circuit have excellent agreement with full-wave electromagnetic simulations. This circuit model takes three parameters as inputs that are the number, the ON/OFF state and the locations of the MEMS switches within the slot. Depending on these three parameters, it helps to search out such unit cell configurations that provide 360° phase range with linear distribution of the selected phases over this range.

If you want children to keep their feet on the ground,
put some responsibility on their shoulders.
Abigail Van Buren

3

Optimization of MEMS-Controlled Reflectarray Phase Shifters using Equivalent Electrical Circuit Model

3.1. Introduction

In this chapter, we will concentrate primarily on the MEMS switch losses with in the reflectarray unit cell. Our main focus will be on the strategy of reducing the power losses in the phase shifter cell and making the circuit model more flexible regarding the MEMS ON/OFF capacitance values. The following section 3.2 presents the design strategy for the phase shifter cell; it shows how the losses can be greatly reduced by using MEMS switches in pair and highlights the effect of the position of the MEMS switch on the power losses. For validation purposes equivalent circuit results have been compared with HFSS. Section 3.3 discusses the effect of ON/OFF MEMS capacitance ratios on the design of phase shifter cell and Section 3.4 explains how the electrical circuit model can be efficiently used to find the redundant positions of the MEMS switches within the slot. Conclusions are summarized in Section 3.5.

3.2. Electromagnetic Dissipated Power Control

3.2.1. Equivalent Circuit Model including Loss Resistance of RF MEMS Switch

As discussed in the previous chapter that the typical loss resistance of capacitive RF-MEMS switches falls in between 0.1 Ω and 1Ω. If such resistance is connected in series with the MEMS reactance in the equivalent circuit of Figure 2.12, we observed that this loss resistance have no effect on the reflected phase distribution of the unit cell and the phase diagram of the reflectarray element remains same as obtained in the lossless case. The equivalent circuit of the phase-shifter cell having N number of MEMS switches with coordinates x_1, x_2, x_3… x_N including the MEMS resistance is given in Figure 3.1(a). The numerical values for the elements L_1, C_1, L_2, C_2, L_s, C_s, $L'(x)$, $C'(x)$ and their process of extraction have been fully explained in chapter 2. The effect of MEMS switch resistance when the switch is OFF is almost negligible. It is not the case when the switch is ON.

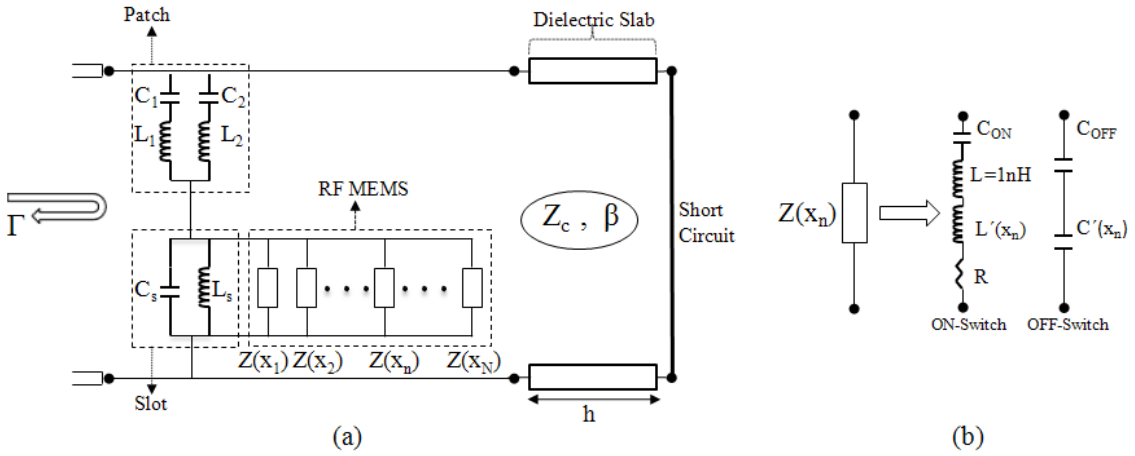

Figure 3.1: (a) Equivalent electrical circuit for the MEMS-controlled phase-shifter cell; (b) Equivalent circuit model of the n^{th} MEMS switch within the slot (the equivalent impedance Z depends on the ON/OFF state of the switch as well as its coordinate x_n inside the slot).

3.2.2. Single MEMS Topology

As it has been explained in chapter 2 that by using the equivalent circuit model we can find out such phase shifter configurations from thousands of raw configurations (containing at least three MEMS) that give required number of selected phases (two, four or more) covering 360° phase range and having linear phase distribution among them and this process can be done within much smaller time and memory resources as compared to the full wave simulations. Here first we present phase results of a unit cell configuration selected using the equivalent circuit model and then the power loss results for this configuration are presented. Here the MEMS switches are being treated on individual basis i.e., each command 1 or 0 will directly control one MEMS switch instead of two MEMS switches (as in the case of double

MEMS topology in next Section), hence this technique can be called as single MEMS topology. In the next Section, we will discuss the strategy of reducing these MEMS switches losses within the unit cell under double MEMS topology.

3.2.2.1. Power Loss Analysis

Table 3.1 shows the reflected phase results at 13GHz for a phase shifter configuration with 3-MEMS while Figure 3.2(a) presents the total power loss for the same configuration versus resistance (R) of the MEMS switch. The range of the MEMS resistance is taken from 0-2Ω. Figure 3.2(b) shows what percentage of the total phase shifter dissipated power goes to each ON-MEMS individually.

Table 3.1

Phase-shifts at 13GHz, computed from the equivalent electrical circuit model and HFSS for phase-shifter cells loading by 3 RF-MEMS switches with (a) x_1=0.45mm, x_2=2.25mm, x_3 =3.2mm

Command law	Phase Φ_{EC} by equivalent circuit model	Phase Φ_{HFSS} by HFSS	Linearity Check (The successive difference among four phase shifts)	Phase difference $\Phi_{EC} - \Phi_{HFSS}$
001	-164°	-173°	Reference Phase	9°
111	-72°	-70°	92°	2°
000	15°	18°	179°	3°
010	108°	113°	272°	5°

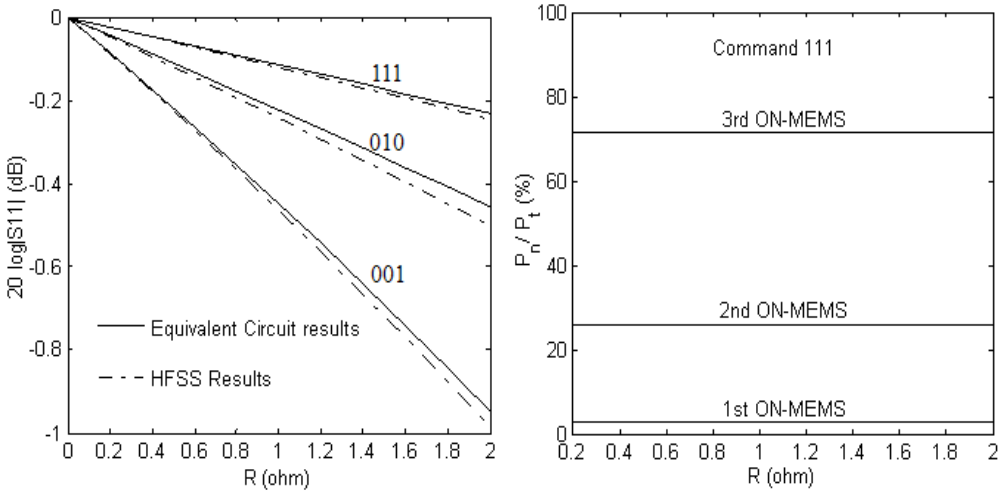

(a) (b)

Figure 3.2: (a) Results obtained by equivalent circuit and HFSS under single MEMS case (a) Comparison between power loss results obtained by HFSS and the equivalent circuit for the unit cell as a whole (b) Power dissipated within the ON-MEMS individually (P_n represents the individual power of an ON-MEMS, n denotes the number of the ON-MEMS, P_t denotes the total power dissipated within the unit cell).

Figure 3.2(a) presents the power loss within the unit cell for three commands 111,010 and 001. The power loss for the fourth command 000 is not shown because it has no ON-MEMS so power loss will be nearly zero for this command. The maximum power loss within the unit cell goes up to 1 dB (as in the case of 001 command). In the Figure 3.2(b), it has been shown that the power dissipated within the unit cell in case of 111 is distributed on three MEMS as all the three MEMS are ON in this command. While individual percentages are not shown for the commands 001 and 010 as in this case all the power goes to one MEMS because only one MEMS is ON in these commands.

From a technological point of view, the total dissipated power within the unit cell should be firstly, as small as possible and secondly quasi-equally distributed among all the ON-MEMS to ensure an identical reliability of all the MEMS. Without optimization, as shown in the Figure 2(b), 72% of the total dissipated power goes to the 3rd switch, 25% to the 2nd and 3% to the 1st one. In the next section, we see how the overall power losses can be reduced and more conveniently distributed over all the ON-MEMS by using double MEMS topology i.e., MEMS switches in pair-form.

3.2.3. Double MEMS Topology

For a given distribution of the required phase-shifts (i.e., for a fixed number of phase-shifts) at a given frequency, our main goal is to reach out to a design of the phase shifter cell having minimum number of MEMS and minimum power losses. In order to minimize the power losses and achieve the required distribution of the phase shifts by commanding the ON/OFF state of the MEMS (i.e., from 000 to 111 in three switch case) we have two strategies. First we could use those commands which consist of at least two ON-MEMS: for example, instead of using commands 001,100 or 010 (as done in the previous section) we should prefer the commands 011, 101 or 110.By using commands containing at least two ON-MEMS the overall dissipated power in the unit cell and within each MEMS switch is reduced. But this technique is not applicable as it may disturb the linearity among the reflected phases which is our primary goal. The second strategy for minimizing the dissipated power is to replace each single MEMS switch with a pair of MEMS switches. For example,

each MEMS of the cell studied in the previous section is replaced by a pair of MEMS, the same command being applied simultaneously to the pair. The total number of the MEMS is then doubled whereas the number of commands stays constant. For example, the command 110 corresponds to 11 11 00 (i.e., each 1 or 0 in the command 110 controls respectively two ON or OFF MEMS: Double MEMS Topology).

3.2.3.1. Power Loss Analysis

Now again for the double MEMS topology the equivalent circuit model is used to find such phase shifter configurations that give equal distribution of the selected number of phases. Table 3.2 shows the phase results for one phase shifter configuration found out by the equivalent circuit applying double MEMS topology. For this double MEMS topology based phase shifter cell Figures 3.3(a) and (b) give respectively the dissipated power results within the whole cell and individually within the ON-MEMS of each command.

Table 3.2

Phase-shifts at 13GHz, computed from the equivalent electrical circuit model and HFSS for the phase-shifter cells loading by 6 RF-MEMS switches actuating them in pair-form having the locations: 1st pair → x_1=0.45mm, x_2=0.56mm, 2nd pair → x_3 =5.45mm, x_4 =6.34mm, 3rd pair → x_5 =1.75mm, x_6 =1.86mm

Command law	Phase Φ_{EC} by equivalent circuit model	Phase Φ_{HFSS} by HFSS	Linearity Check (The successive difference among four phases shifts)	Phase difference $\Phi_{EC} - \Phi_{HFSS}$
110 (111100)	-164°	-162°	Reference Phase	2°
011 (001111)	-71°	-65°	87°	6°
100 (110000)	18°	18°	179°	0°
010 (001100)	109°	107°	271°	2°

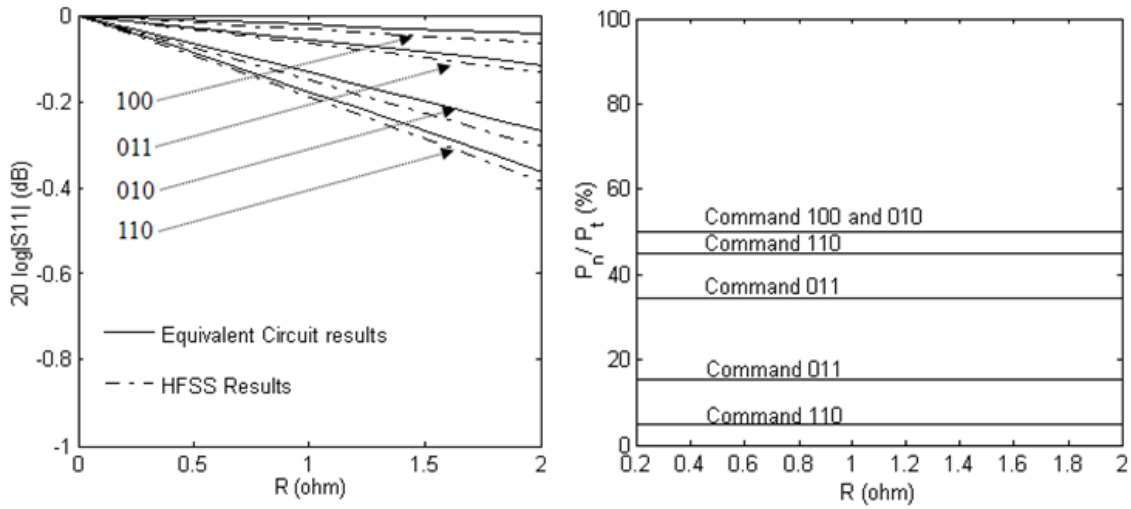

(a) (b)

Figure 3.3: (a) Results obtained by the equivalent circuit and HFSS under double MEMS case (a) Comparison between Power loss results obtained by HFSS and equivalent circuit for the unit cell as a whole (b) Power dissipated within the ON-MEMS individually.

It is clear from the results of Figure 3.3(a) that if we replace single MEMS with double MEMS, then the overall power loss decreases to even less than half of the value comes in single MEMS case. In single MEMS case the highest loss goes up to 1dB (see Figure 3.2(a)) but in double MEMS case, it reduces to less than 0.4dB. Also as in Figure 3.3(b), the ratio of the dissipated power per MEMS switch decreases greatly.

Now let see up to which extent the 2nd issue (power losses should be quasi-equally distributed among all the ON-MEMS to ensure an identical reliability of all the ON MEMS). As shown in Table 3.2, since only two MEMS are ON in both 3rd (100 → 11 00 00) and 4th (010 → 00 11 00) commands, so the dissipated power is divided equally in the two ON MEMS i.e., 50% each giving them more reliability as compared to single MEMS topology. Also in both of the 1st (110 → 11 11 00) and 2nd (011 → 00 11 11) commands the dissipated power divided among four MEMS but the part of the dissipated power for each MEMS remains less than 50%. Hence the result is if we replace single MEMS with two MEMS then the power loss among the ON MEMS is almost equally distributed reducing the chances of their breakdown. The phase distribution results of Figure 3.3 also have excellent agreement with that of HFSS as shown in Table 3.2.

Finally as expected we have found that if double MEMS technique is used, then power dissipated within the phase shifter cell and within each MEMS switch individually can be

greatly reduced. As it has been discussed in chapter 1 and 2 that the main source of the power absorption within the electronically tunable microstrip reflectarrays are the tuning elements themselves (RF-MEMS switches here) therefore by applying proposed double MEMS topology this power consumption can be effectively controlled approximately up to 60% as depicted in Figure 3.3(a).

3.2.4. Effect of the Position of the RF-MEMS Switches on the Power Losses

Power dissipated in the phase shifter cell greatly depends on another very important design parameter i.e., location of the RF-MEMS switches inside the slot. We can control the overall power losses in the cell and also reduce the individual level of the dissipated power within the ON-MEMS by finding their most suitable locations within the phase shifter cell. But to search out such locations for multiple RF-MEMS switches within the slot among hundreds of thousands of their possible locations is impossible through full wave analysis tools like CST [71], FEKO [72], IE3D [73] and HFSS [75]. This is another critical situation where the equivalent electrical circuit proves very helpful in the form of memory and time efficiency.

Figure 3.4 presents the power losses in the unit cell containing one MEMS switch versus its position inside the slot. Electric current passing through the switch versus its position inside the slot has also been shown. Power losses gradually increase as the switch moves from the edge towards the centre of the slot because the corresponding current value flowing through the switch increases as it moves from the edge towards the centre of the slot.

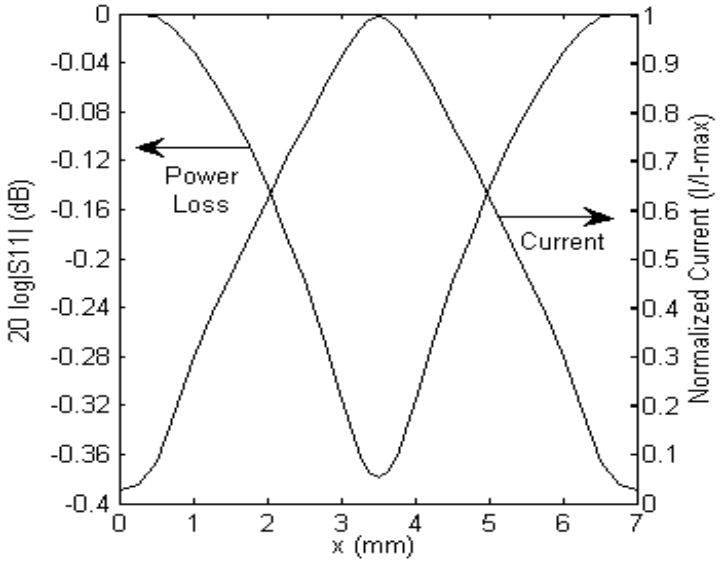

Figure 3.4: Power loss and current versus position (x) of the MEMS switch inside the slot.

From the above power loss results versus the location of the switch, it is concluded that the power dissipated in the phase shifter cell can be controlled by preferring such phase shifter configurations in which MEMS switches are situated near the edges of the slot rather than near the center of the slot. On the basis of this analysis, we have used the equivalent electrical circuit model to find the optimized cell configurations with respect to the positions of the RF-MEMS switches within the slot. These cell configurations have then been used to design a steerable reflectarray. This reflectarray will be discussed in the Section II of the thesis.

3.3. Analysis of the MEMS Switch Capacitance Ratio C_{ON}/C_{OFF}

MEMS-capacitance ratio (C_{ON}/C_{OFF}) is an important parameter and has a critical role in the design and optimization of a reflectarray unit cell incorporating RF-MEMS switches. RF-MEMS do not have high capacitance ratios (C_{ON}/C_{OFF}) as high ratios are technologically difficult to attain. So an equivalent circuit will be more representative and close to what can be manufactured if it works for small ratios. In general, the capacitance ratio of a capacitive RF-MEMS switch lies between 25 and 75 with C_{ON}=1-4pF and C_{OFF}=20-50fF [62-63]. For the equivalent circuit model of Figure 2.2 the lowest limit of C_{ON}/C_{OFF} for which it gives a

linear distribution of the phase-shifts can be easily determined by testing different values of C_{ON} and C_{OFF}. It has been found that the equivalent circuit model of Figure 3.1 efficiently works with RF-MEMS capacitance ratios (C_{ON}/C_{OFF}) as low as14.3. Therefore by using this equivalent circuit model with RF-MEMS switches having any value of $C_{ON} \geq$ 1pF and $C_{OFF} \leq$ 70fF, a successful phase shifter design holding the required linear distribution of selected phases can be easily found.

As an example, Table 3.3 presents the phase results for a phase shifter configuration with RF-MEMS capacitance ratio C_{ON}/C_{OFF} = 14.3 (C_{ON}= 1pF and C_{OFF}= 70fF). All the four phases are almost linearly distributed with successive phase difference of 90° over 360° phase range. The comparison with HFSS results is also presented.

Table 3.3

Phase-shifts at 13GHz, computed from the equivalent electrical circuit model and HFSS for the phase-shifter cell loading with 3 RF-MEMS switches with x_1=0.25mm, x_2=2mm and x_3 =2.95mm

Command law	Phase Φ_{EC} (by Equivalent Circuit Model)	Phase Φ_{HFSS} (by HFSS)	Linearity Check (The successive difference among four phases shifts)	Phase difference $\Phi_{EC} - \Phi_{HFSS}$
001	-159	-155	Reference Phase	4°
011	-71	-74	88°	3°
100	19	19	178°	0°
010	111	115	270°	4°

Similarly we have found many phase shifter configurations using the equivalent circuit of Figure 1 varying the C_{ON} from 1pF to any higher value and C_{OFF} from any lower value to 70fF. In all configurations the equivalent circuit results are in good agreement with that of HFSS. So this equivalent circuit is effectively applicable for the analysis and design of the phase shifter cell incorporating RF-MEMS having minimum C_{ON} equal to 1pF and maximum C_{OFF} equal to 0.07pF. Using the technological limits of C_{ON} and C_{OFF} and the limits set by the equivalent circuit model of Figure 3.1, we can define a design area for a phase shifter cell containing RF-MEMS switches (see Figure 3.5).

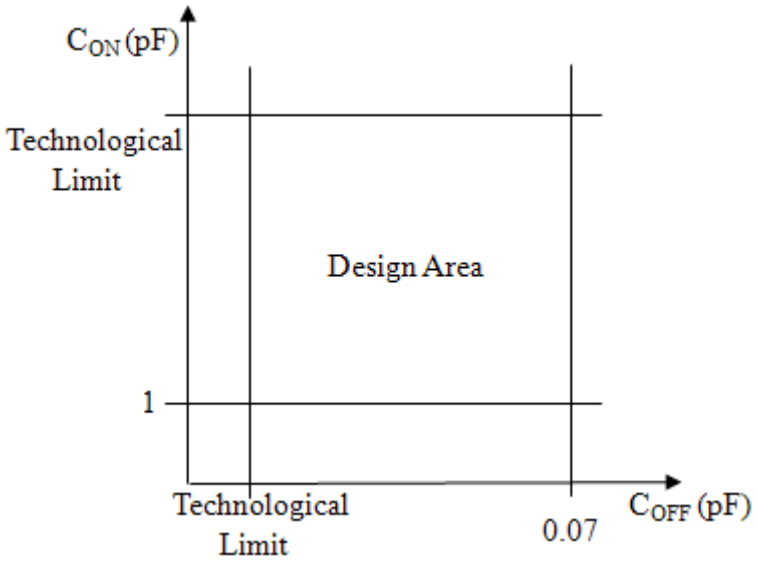

Figure 3.5: Graph for the phase shifter cell showing the design limits on the basis of C_{ON} and C_{OFF}.

3.4. Redundancy Check

Reliability is a major concern for RF MEMS switches due to which their deployment into many commercial and defense applications is still limited. As it is discussed in [64], the life time of Ohmic contact RF-MEMS switches decreases due to contact degradation and contamination while capacitive switches exhibit failures due to dielectric charging effects. The research is being done in different aspects to overcome this reliability problem by understanding specific failure mechanisms for different kind of RF MEMS switches. Here, it is worthy to mention that double MEMS topology can also play an important role to enhance the reliability and the lifetime of reflectarray antennas incorporating RF MEMS switches. If single MEMS are replaced with double MEMS without affecting linearity among the phase shifts then the 2nd MEMS switch might be used in case of first MEMS stops working without halting the whole operation of the reflectarray system.

To do so, we have to find suitable extra locations to insert redundancy MEMS without disturbing the phase linearity. This is where the equivalent circuit can be of another great interest in terms of memory and time resources as compared to conventional full wave methods. The equivalent circuit model can give us such redundant locations (i.e., position (x) of the switch with in the slot) to adjust extra RF-MEMS switches within almost negligible computational efforts. By using the equivalent circuit of Figure 3.1, we can verify that

whether, for a specific configuration, the redundant locations for one or more switches with respect to the corresponding commands exist or not. We have applied the equivalent circuit to search out such extra locations at which additional MEMS can be embedded and then used at need without deteriorating the original phase results. As an example, in Table 3.4, phase results for one configuration are given, the redundant locations for all the three MEMS also given respectively in the caption. The MEMS switches incorporated at respective redundant locations can be put into function when any of the respective operating switch is damaged, more clearly we can say that if the MEMS switch at x_1 breaks down then its respective counterpart at redundant location x_{r1} can be put into functioning, where 'r' represents redundant position.

Table 3.4

Phase-shifts at 13GHz, Phase-shifter loaded with 3 RF-MEMS with x_1=0.45mm, x_2=2.25mm, x_3 =3.2mm, alternate locations are x_{r1}=6.45mm, x_{r2}=4.65mm, x_{r3} =3.7mm

Command law	Phase Φ_{EC} by equivalent circuit model	Phase Φ_{HFSS} by HFSS	Linearity Check (The successive difference among four phases shifts)	Phase difference $\Phi_{EC} - \Phi_{HFSS}$
001	-164°	-173°	Reference Phase	9°
111	-72°	-70°	92°	2°
000	15°	18°	179°	4°
010	108°	113°	272°	5°

3.5. Conclusions

This chapter presents a time and power efficient method in the form of an equivalent circuit model used to optimize the design of a reflectarray phase shifter cell. This design method deals especially with the power losses and the ON/OFF capacitance values of MEMS switches. To reduce the power losses while maintaining linear distribution among the selected phases, double MEMS technique has been proposed. This technique reduces power losses to a great extent approximately up to 65% losses are reduced. Also it has been reported that the equivalent circuit can work within a wide range of MEMS ON/OFF capacitances. Finally it has been discussed how the power losses depend on the locations of the switches and how the reliability of the design can be enhanced using redundancy MEMS. The results given by the equivalent circuit model are in excellent agreement with that of High Frequency Structure Simulator (HFSS).

The willingness to accept responsibility for one's own life is the source from which self-respect springs.
Joan Didion

Section II

Electromagnetic Modeling of Large Microstrip Reflectarrays by Scale Changing Technique

When others, a man begins to blame He'll soon find himself alone, The same. Nigel Bloomfield

4

Theory and Formulation of Scale Changing Technique

4.1 Introduction

Electrically large structures i.e., the structures having dimensions of many orders of the wavelength e.g. finite-sized reflectarrays having identical or non-identical unit cells, reconfigurable reflectarrays, microstrip antennas containing active electronic devices and circuits, multiband devices and systems such as frequency selective surfaces, log-periodic and self-similar fractal structures are said to be complex when their geometrical dimensions vary over a large range of scale. In other words we have very fine and large collection of metallic patterns printed on the same dielectric surface. As in chapter 1 it has been explained in detail that linear meshing in these complex planar structures requires tremendous amount of computational resources and may lead to ill-conditioned matrices. Hence an original approach for solving such numerical problems linked to multiscale aspect of modern complex microstrip antennas has been proposed.

Scale Changing Technique (SCT) gets its name from scaled partitioning of the planar structure and the modeling of the electromagnetic interactions between these scale-levels. The higher the number of scale-levels the higher is the complexity. In this chapter SCT formulation in the perspective of a generic multi-scale structure consisting of metallic

patterns printed on a dielectric planar surface is presented. The procedure can be outlined in the following steps:

1) The multi-scale planar surface is partitioned into smaller and smaller sub-domains, while doing so we actually define various scale levels inside the structure.
2) The electromagnetic fields are expressed on orthogonal modal-basis defined for each of these sub-domains bounded by their respective boundary conditions.
3) Modal contributions are treated separately for lower order modes and higher order modes. Higher order modes are considered to contribute only locally where as lower order modes define coupling with the domain at the higher scales.
4) Electromagnetic coupling between two successive scales is modeled by a scale-changing network (SCN) defined by the lower order modes of the two sub-domains.
5) Electromagnetic modeling for the complete structure is obtained by a simple cascade of all these scale-changing networks.

These concepts will be explained in further detail in the subsequent sections.

4.2. Discontinuity Plane

To understand the concepts and workings of the Scale Changing Technique we will study a general case of an arbitrary discontinuity. Consider multiple metallic patterns with the dimension varying over a wide range of scale, printed on a planar dielectric surface as shown in Figure 4.1(a). Suppose that the largest patterns are several orders of magnitude bigger than the finest patterns. This discontinuity plane may be modeled by positioning it at a cross-section of a waveguide or can simply be located in the free-space. The two half-regions i.e. the left-hand region and the right hand region are assumed to be composed of multilayered and loss-less dielectric media.

4.2.1. Partitioning of the Discontinuity Plane

The starting point of the proposed approach involves the coarse partitioning of the discontinuity plane into smaller domains and sub-domains having comparable sizes (Step 1); in each sub-domain a second partitioning is performed by introducing smaller sub-domains of comparable sizes (Step 2); again, in each sub-domain introduced at the second step a third partitioning is performed by introducing smaller sub-domains (Step 3); and so on, as illustrated in Figure 4.1(b).

This procedure of partitioning the domains into smaller sub-domains is repeated until the finest dimension or smallest scale is reached. Such hierarchical domain-decomposition allows rapid focusing on increasing details of the planar geometry unlike a linear meshing approach.

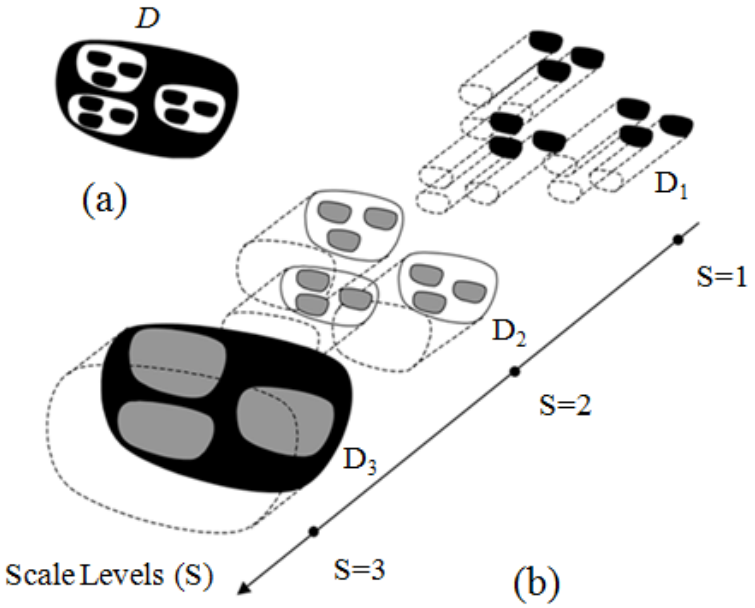

Figure 4.1: (a) An example of discontinuity plane presenting 3 scale-levels (black is metal and white is dielectric) (b) The scattered view of the various sub-domains at different scale levels generated by the partitioning process [35].

To each sub-domain is associated a scale level S: generally the largest sub-domains corresponds conventionally to the scale level $S=S_{max}$ while the smallest scale corresponds to the scale level S=1. It is important to note that the scattered representation of the domains is only for the sake of clarity, essentially all the domains and sub-domains lie in the same plane. This manner of partitioning the complex discontinuity plane (let say D) allows us to define separate scale-levels for the *co-planar* domains and sub-domains such that $D_S > D_{S-1} > D_{S-2} > \cdots > D_1$. In order to eliminate numerical problems due to ill-conditioned matrices, the partition can be chosen in order to avoid high aspect ratios: two successive scale levels may be taken such that, for instance, $D_S/D_{S-1} < 100$.

4.2.2. Choice of Boundary Conditions

Let's consider again the case of a general discontinuity plane of Figure 4.2. Assuming it to be the i^{th} domain at a general scale level S, it can be denoted for convenience as $D_i^{(S)}$, where $i = 1 - N$, N being the total number of domains at scale-level S and S ranging from 1

to S_{max}. Using the above described partitioning procedure the domain $D_i^{(S)}$ can be decomposed further into M sub-domains denoted by $D_j^{(s-1)}$, where $j = 1 - M$ defined at scale-level S-1. In addition, the discontinuity plane may contain simple metallic and dielectric domains where further partitioning may not be needed [35].

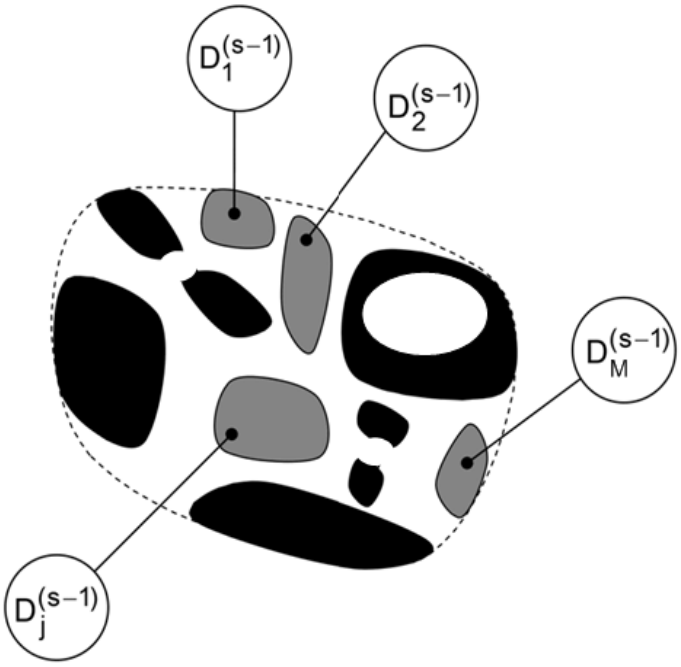

Figure 4.2: The i^{th} generic domain resulting from the partition process at scale level S (black is metal, white is dielectric and grey indicates the location of sub-domains $D_j^{(s-1)}$ (with j = 1, 2, … M) [35].

Artificial boundary conditions are introduced along the contours of all these domains and sub-domains. These boundary conditions are introduced only on the contours of the sub-domains and not in the two half-regions on each side of this discontinuity. The boundary conditions are selected from

1) Perfect Electric Boundary Conditions (PECs)
2) Perfect Magnetic Boundary Conditions (PMCs)
3) A succession of PECs and PMCs
4) Periodic Boundary Conditions (PBCs)

The physics of the problem should be considered in the choice of the boundary conditions around any domain. In practice boundary conditions have to be tried on the contours of each

sub-domain and the quality of the numerical solution in terms of accuracy, execution time and numerical convergence has to be checked subsequently.

The purpose of introducing the boundary conditions at the sub-domain level is essentially to define a new boundary value problem at a local level that can be solved independently by expressing the tangential fields in the region on the modal-basis respecting these boundary conditions. At sub-domain level each boundary value electromagnetic problem is resolved by writing the field equations in integral equation formulation and applying the Galerkin method to solve for the surface fields and currents.

Since now we have many smaller independent problems, the number of unknowns in the matrix equations are reduced and therefore much less memory resources are required to deal individual problems. It is to be noted here that due to introduction of artificial boundary condition the scale-changing technique is not an exact technique but an approximate method. And these approximations need to be chosen carefully not to significantly perturb the accuracy of the solution [65].

4.2.3. Field Expansion on Orthogonal Modes

In the sub-domain $D_i^{(S)}$ enclosed by artificial boundary conditions the modal expansion of the tangential electromagnetic field can be performed. The $\boldsymbol{n^{th}}$ mode of the modal basis $\vec{\boldsymbol{F}}_{\boldsymbol{n}}^{(\boldsymbol{i},\boldsymbol{s})}$ is solution to the following Helmholtz equation [66].

$$\left[\nabla_T^2 + k_n^{(i,s)^2}\right] \vec{\boldsymbol{F}}_{\boldsymbol{n}}^{(\boldsymbol{i},\boldsymbol{s})} = \vec{0} \tag{4.1}$$

In equation (4.1) ∇_T^2 is the transverse Laplacian operator and $k_n^{(i,s)}$ is the cut-off wave-number of the $\boldsymbol{n^{th}}$ mode of the i^{th} sub-domain at the scale-level S i.e. $D_i^{(S)}$. The $\vec{\boldsymbol{F}}_{\boldsymbol{n}}^{(\boldsymbol{i},\boldsymbol{s})}$ is the orthogonal modal-basis which satisfies the boundary conditions at the contours of the sub-domain. The condition of orthognality dictates;

$$\langle \vec{\boldsymbol{F}}_{\boldsymbol{m}}^{(\boldsymbol{i},\boldsymbol{s})}, \vec{\boldsymbol{F}}_{\boldsymbol{n}}^{(\boldsymbol{i},\boldsymbol{s})} \rangle = \iint_{D_i^{(s)}} \left[\vec{\boldsymbol{F}}_{\boldsymbol{m}}^{(\boldsymbol{i},\boldsymbol{s})}\right]^* \cdot \vec{\boldsymbol{F}}_{\boldsymbol{n}}^{(\boldsymbol{i},\boldsymbol{s})} ds = \begin{cases} 0 & for\ m \neq n \\ 1 & for\ m = n \end{cases} \tag{4.2}$$

The $*$ operator represents the complex conjugate. In the SCT formulation here, a normalized set of modes $\left\{\vec{\boldsymbol{F}}_{\boldsymbol{n}}^{(\boldsymbol{i},\boldsymbol{s})}\right\}_{n=1,2,3,\ldots}$ is used, thus $\langle \vec{\boldsymbol{F}}_{\boldsymbol{m}}^{(\boldsymbol{i},\boldsymbol{s})}, \vec{\boldsymbol{F}}_{\boldsymbol{n}}^{(\boldsymbol{i},\boldsymbol{s})} \rangle = \boldsymbol{\delta_{mn}}$ where $\boldsymbol{\delta_{mn}}$ designates the Kronecker delta function $\delta_{mn} = 1 \; if \; m = n, \; 0$ otherwise.

4.2.4. Active and Passive Modes

The field contributions due to lower-order and higher-order modes can be treated separately. As the order of the modes increases, the energy diffracted from the metal interface for that harmonic becomes more and more localized within the vicinity [66]. Therefore it is pretty safe to assume that after a certain number of modes, the higher order modes will contribute only to very fine-scale variations of the electromagnetic field that are localized to that particular sub-domain. On the other hand the lower order modes describe the large-scale variations of the field that couples with the tangential fields of the sister sub-domains.

In case of the generic sub-domain $\mathrm{D}_{\mathrm{i}}^{(\mathrm{s})}$ of Figure 4.2, it can be anticipated without any kind of calculations that the tangential electromagnetic field in $\mathrm{D}_{\mathrm{i}}^{(\mathrm{s})}$ contains smooth (large-scale) variations and highly irregular (fine-scale) fluctuations. The fine-scale variations can be described as a linear combination of an infinite number of higher-order modes of $\vec{\boldsymbol{F}}_{\boldsymbol{n}}^{(\boldsymbol{i},\boldsymbol{s})}$ which are spatially localized in the vicinity of discontinuities, sharp edges and various contours of the domain and therefore does not significantly contribute to the electromagnetic coupling between the various sub-domains $\mathrm{D}_{\mathrm{j}}^{(\mathrm{s}-1)}$. For this reason these higher-order modes are called *passive modes* in SCT formalism.

The large-scale contribution to the field in the domain $\mathrm{D}_{\mathrm{i}}^{(\mathrm{s})}$ is due to the electromagnetic coupling between the constitutive sub-domains $\mathrm{D}_{\mathrm{j}}^{(\mathrm{s}-1)}$. These couplings can be modeled as the combination of only a limited number of lower-order modes in the spectral domain. As these lower-order modes are involved in the description of electromagnetic coupling between different domains and sub-domains so in SCT formalism they are called *active modes*. Finally, due to their largely different spatial frequencies, any active mode in $\mathrm{D}_{\mathrm{i}}^{(\mathrm{s})}$ weakly interacts with any passive mode in the constitutive sub-domains $\mathrm{D}_{\mathrm{j}}^{(\mathrm{s}-1)}$.

It follows from the above-mentioned physical considerations that the electromagnetic coupling between two subsequent scale-levels, e.g. the scale-level S and the lower scale S-1,

can be modeled by describing that how any active mode in the domain $D_i^{(s)}$ interacts with the active modes in the sub-domains $D_j^{(s-1)}$.

4.2.5. Scale Changing Network (SCN)

The mutual coupling of the active modes described in the previous section can be represented by a multiport of Figure 4.3. Each port in the network represents an active mode. The ports on the left hand side models the active modes in domain $D_i^{(s)}$ whereas the M set of ports on the right hand side denote the active modes of M sub-domains $D_j^{(s-1)}$(where$j = 1 - M$) at scale level S-1. As this multiport allows to relate the fields at scale S to the fields at the lower scale S-1, it is named the *Scale-Changing Network (SCN)*.

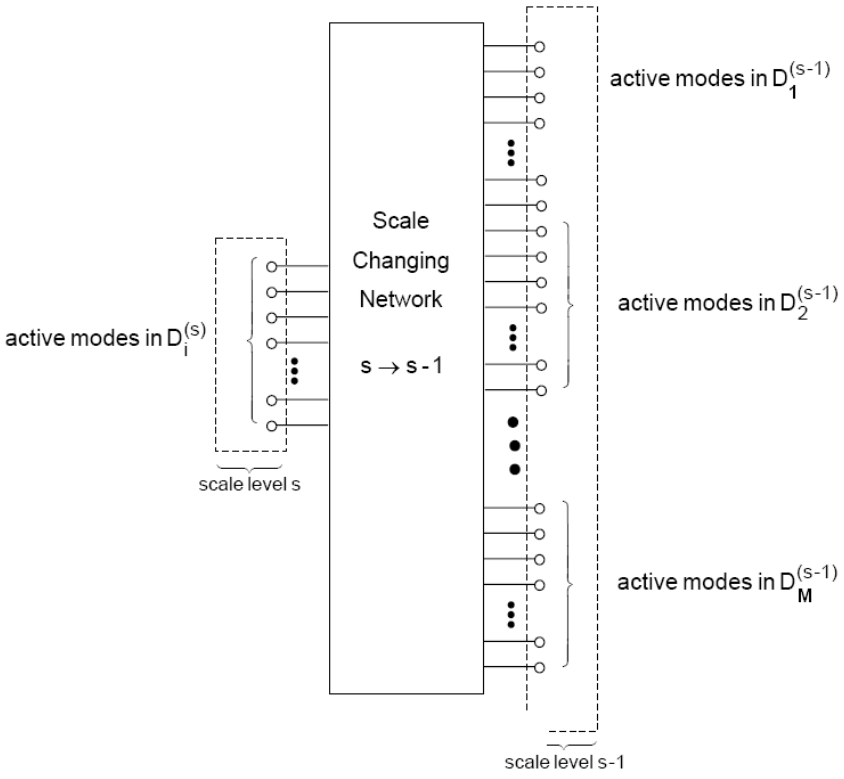

Figure 4.3: The Scale Changing Network coupling the active modes in the domain $D_i^{(s)}$ (scale level s) and its constitutive sub-domains $D_j^{(s-1)}$ (scale level s–1) [35].

For relating the electromagnetic fields at scale S to that of another scale S-2, the interconnection of scale-changing networks may be performed as shown in Figure 4.4, each network being previously computed separately. Consequently, the modeling of interaction among the multiple scales of a complex discontinuity plane is reduced to simple cascade of appropriate scale-changing networks, where each network models the interaction between two scales.

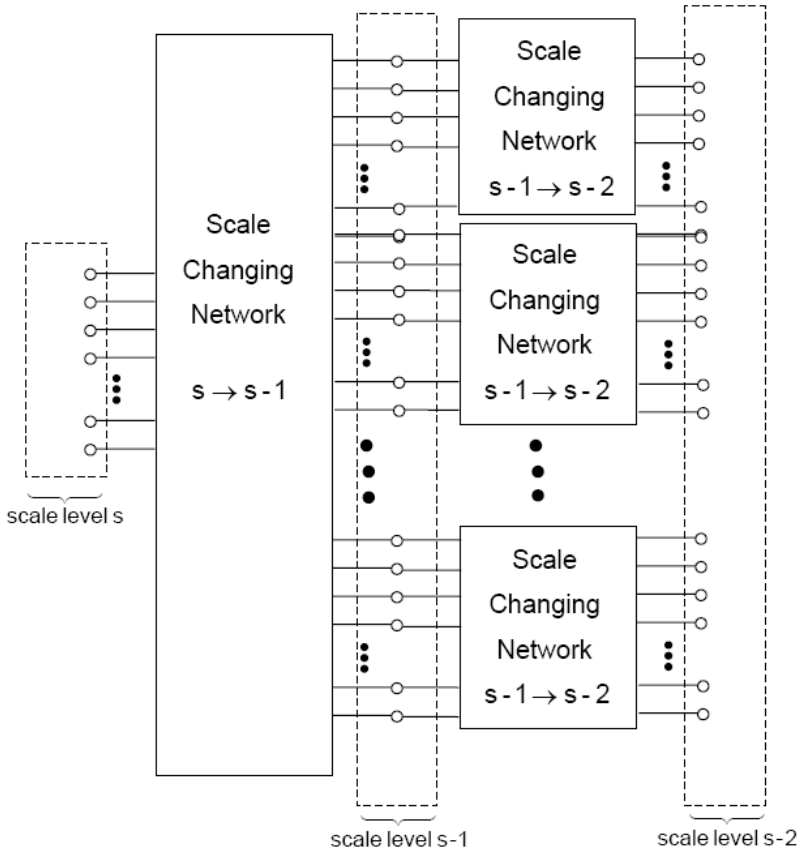

Figure 4.4: The cascade of Scale Changing Networks allows relating the transverse electromagnetic field at scale level S to that of at scale level S–2 [35].

It is important to note that the computation of these scale-changing networks is mutually independent. Therefore each network can be computed by using a separate processing node. This modular nature of scale-changing technique can be exploited in multiprocessing environments to cut simulation times in case of very large and complex structures. Moreover any single change at any scale-level will only need the re-computation of two scale-changing networks and not the SCNs for all other scales. This means that small geometric changes will not require the entire simulation of the structure all over again. This feature is an essential

quality of a good parametric tool. Therefore SCT designs will have the capability of rapid simulations in the case where when the effects of certain modifications are studied on the design.

The derivation of scale-changing network's characterization matrix requires the definition of artificial electromagnetic sources named the *scale-changing sources* in various sub-domains obtained from the partitioning process. The following Section defines these sources.

4.3. Scale Changing Sources

The derivation of scale-changing network that couples the scale S to the adjacent scale S-1 requires the resolution of a boundary value problem in which active modes act as the actual sources called the modal *Scale Changing Sources* for the problem. When cascading the SCN for the global simulation of the multi-scale discontinuity plane, the two half regions on both sides of this plane has to be taken into account. In order to formulate a non redundant approach the SCN computation incorporates the two half-regions at larger scale S only (and not at the smaller scale S-1). It follows that the modal *Scale Changing Sources* at scale S differs from those at the smaller scale S-1.

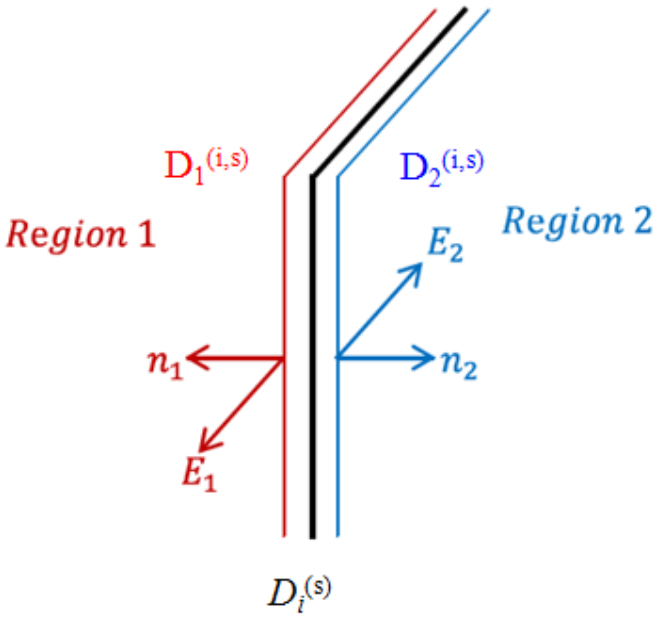

Figure 4.5: The discontinuity plane $D_i^{(s)}$ along with two infinitely close parallel side-planes $D_\alpha^{(i,s)}$ with $\alpha = 1,2$ representing the two half-regions.

To derive the mathematical expressions for scale changing sources lets once again consider the generic sub-domain $D_i^{(s)}$ as shown in Figure 4.5. At both sides of this general domain the two half regions 1 and 2 are composed of multilayered and lossless dielectric media. Let $D_\alpha^{(i,s)}$ with $\alpha = 1,2$ denote the two planes in the two half regions 1, 2. These planes are positioned infinitely close to the domain $D_i^{(s)}$. The unit-vectors $\vec{n}_1$ and $\vec{n}_2$ are the normal vectors to $D_\alpha^{(i,s)}$. Finally, let $\vec{\boldsymbol{E}}_{\boldsymbol{\alpha}}^{(\boldsymbol{i},\boldsymbol{s})}$ and $\vec{\boldsymbol{H}}_{\boldsymbol{\alpha}}^{(\boldsymbol{i},\boldsymbol{s})}$ be respectively the tangential electric and magnetic fields on the two domains $D_\alpha^{(i,s)}$. The set of modes $\left\{\vec{\boldsymbol{F}}_{\boldsymbol{n}}^{(\boldsymbol{i},\boldsymbol{s})}\right\}_{\boldsymbol{n}=\boldsymbol{1},\boldsymbol{2},\ldots}$ introduces in Section 4.2.3 is now used for the expansion of the tangential electromagnetic fields on the domains $D_1^{(i,s)}$ and $D_2^{(i,s)}$ as follows:

$$\vec{\boldsymbol{E}}_{\boldsymbol{\alpha}}^{(\boldsymbol{i},\boldsymbol{s})} = \sum_{\boldsymbol{n}=\boldsymbol{1}}^{\infty} V_n^{(i,s,\alpha)}\, \vec{\boldsymbol{F}}_{\boldsymbol{n}}^{(\boldsymbol{i},\boldsymbol{s})} \tag{4.3}$$

$$\vec{\boldsymbol{J}}_{\boldsymbol{\alpha}}^{(\boldsymbol{i},\boldsymbol{s})} = \vec{\boldsymbol{H}}_{\boldsymbol{\alpha}}^{(\boldsymbol{i},\boldsymbol{s})} \times \overrightarrow{\mathbf{n}_{\boldsymbol{\alpha}}} = \sum_{\boldsymbol{n}=\boldsymbol{1}}^{\infty} I_n^{(i,s,\alpha)}\, \vec{\boldsymbol{F}}_{\boldsymbol{n}}^{(\boldsymbol{i},\boldsymbol{s})} \tag{4.4}$$

$V_n^{(i,s,\alpha)}$ and $I_n^{(i,s,\alpha)}$ denote respectively, the voltage and current amplitudes of the n^{th} mode in $D_\alpha^{(i,s)}$. Following the considerations of Section 4.2.4, the tangential electric field $\vec{\boldsymbol{E}}_{\boldsymbol{\alpha}}^{(\boldsymbol{i},\boldsymbol{s})}$ and the surface current density $\vec{\boldsymbol{J}}_{\boldsymbol{\alpha}}^{(\boldsymbol{i},\boldsymbol{s})}$ on $D_\alpha^{(i,s)}$ can be expressed separately with active and passive modes defining the large scale and fine scale variation of these quantities respectively.

$$\begin{cases} \vec{\boldsymbol{E}}_{\boldsymbol{\alpha}}^{(\boldsymbol{i},\boldsymbol{s})} = \sum_{\boldsymbol{n}=\boldsymbol{1}}^{\boldsymbol{N}_{\boldsymbol{\alpha}}} V_n^{(i,s,\alpha)}\, \vec{\boldsymbol{F}}_{\boldsymbol{n}}^{(\boldsymbol{i},\boldsymbol{s})} + \sum_{\boldsymbol{n}=\boldsymbol{N}_{\boldsymbol{\alpha}}+\boldsymbol{1}}^{\infty} V_n^{(i,s,\alpha)}\, \vec{\boldsymbol{F}}_{\boldsymbol{n}}^{(\boldsymbol{i},\boldsymbol{s})} \\ \vec{\boldsymbol{E}}_{\boldsymbol{\alpha}}^{(\boldsymbol{i},\boldsymbol{s})} = \vec{\boldsymbol{E}}_{\boldsymbol{\alpha}}^{(\boldsymbol{i},\boldsymbol{s})}\Big|_{\boldsymbol{large}} + \vec{\boldsymbol{E}}_{\boldsymbol{\alpha}}^{(\boldsymbol{i},\boldsymbol{s})}\Big|_{\boldsymbol{fine}} \end{cases} \tag{4.5}$$

where $\boldsymbol{N}_{\boldsymbol{\alpha}}$ is the number of active modes $D_\alpha^{(i,s)}$. Similarly for surface current density we can write.

$$\begin{cases} \vec{\boldsymbol{J}}_{\boldsymbol{\alpha}}^{(\boldsymbol{i},\boldsymbol{s})} = \sum_{\boldsymbol{n}=\boldsymbol{1}}^{\boldsymbol{N}_{\boldsymbol{\alpha}}} I_n^{(i,s,\alpha)}\, \vec{\boldsymbol{F}}_{\boldsymbol{n}}^{(\boldsymbol{i},\boldsymbol{s})} + \sum_{\boldsymbol{n}=\boldsymbol{N}_{\boldsymbol{\alpha}}+\boldsymbol{1}}^{\infty} I_n^{(i,s,\alpha)}\, \vec{\boldsymbol{F}}_{\boldsymbol{n}}^{(\boldsymbol{i},\boldsymbol{s})} \\ \vec{\boldsymbol{J}}_{\boldsymbol{\alpha}}^{(\boldsymbol{i},\boldsymbol{s})} = \vec{\boldsymbol{J}}_{\boldsymbol{\alpha}}^{(\boldsymbol{i},\boldsymbol{s})}\Big|_{\boldsymbol{large}} + \vec{\boldsymbol{J}}_{\boldsymbol{\alpha}}^{(\boldsymbol{i},\boldsymbol{s})}\Big|_{\boldsymbol{fine}} \end{cases} \tag{4.6}$$

The passive modes being highly evanescent are shunted by their purely reactive modal admittances ($Y_n^{(i,s,\alpha)}$). Consequently,

$$I_n^{(i,s,\alpha)} \approx Y_n^{(i,s,\alpha)} V_n^{(i,s,\alpha)} \qquad \text{for } n > N_\alpha \tag{4.7}$$

Using the formulation of equation (4.6) we obtain:

$$\vec{\boldsymbol{J}}_{\boldsymbol{\alpha}}^{(\boldsymbol{i},\boldsymbol{s})} \approx \vec{\boldsymbol{J}}_{\boldsymbol{\alpha}}^{(\boldsymbol{i},\boldsymbol{s})}\Big|_{\boldsymbol{large}} + \sum_{\boldsymbol{n=N_\alpha+1}}^{\infty} Y_n^{(i,s,\alpha)} V_n^{(i,s,\alpha)} \vec{\boldsymbol{F}}_{\boldsymbol{n}}^{(\boldsymbol{i},\boldsymbol{s})} \tag{4.8}$$

This can be formally written as in the operator form:

$$\vec{\boldsymbol{J}}_{\boldsymbol{\alpha}}^{(\boldsymbol{i},\boldsymbol{s})} = \vec{\boldsymbol{J}}_{\boldsymbol{\alpha}}^{(\boldsymbol{i},\boldsymbol{s})}\Big|_{\boldsymbol{large}} + \hat{Y}_\alpha^{(i,s)} \vec{\boldsymbol{E}}_{\boldsymbol{\alpha}}^{(\boldsymbol{i},\boldsymbol{s})} \tag{4.9}$$

with $\hat{Y}_\alpha^{(i,s)} = \sum_{\boldsymbol{n=N_\alpha+1}}^{\infty} \left|\vec{\boldsymbol{F}}_{\boldsymbol{n}}^{(\boldsymbol{i},\boldsymbol{s})}\right\rangle Y_n^{(i,s,\alpha)} \left\langle \vec{\boldsymbol{F}}_{\boldsymbol{n}}^{(\boldsymbol{i},\boldsymbol{s})}\right|$ where $\hat{Y}_\alpha^{(i,s)}$ is an admittance operator.

Now the tangential electric field and surface current density on the discontinuity plane $D_i^{(s)}$ can be determined from using the following boundary conditions.

$$\begin{cases} \vec{\boldsymbol{E}}_{\boldsymbol{i}}^{(\boldsymbol{s})} = \vec{\boldsymbol{E}}_{\boldsymbol{1}}^{(\boldsymbol{i},\boldsymbol{s})} = \vec{\boldsymbol{E}}_{\boldsymbol{2}}^{(\boldsymbol{i},\boldsymbol{s})} \\ \vec{\boldsymbol{J}}_{\boldsymbol{i}}^{(\boldsymbol{s})} = \vec{\boldsymbol{J}}_{\boldsymbol{1}}^{(\boldsymbol{i},\boldsymbol{s})} + \vec{\boldsymbol{J}}_{\boldsymbol{2}}^{(\boldsymbol{i},\boldsymbol{s})} \end{cases} \tag{4.10}$$

Using the above equations we can solve for the field quantities on the discontinuity plane as follows:

$$\sum_{\boldsymbol{n=1}}^{\infty} V_n^{(i,s)} \vec{\boldsymbol{F}}_{\boldsymbol{n}}^{(\boldsymbol{i},\boldsymbol{s})} = \sum_{\boldsymbol{n=1}}^{\infty} V_n^{(i,s,1)} \vec{\boldsymbol{F}}_{\boldsymbol{n}}^{(\boldsymbol{i},\boldsymbol{s})} = \sum_{\boldsymbol{n=1}}^{\infty} V_n^{(i,s,2)} \vec{\boldsymbol{F}}_{\boldsymbol{n}}^{(\boldsymbol{i},\boldsymbol{s})} \tag{4.11}$$

$$\Rightarrow V_n^{(i,s)} = V_n^{(i,s,1)} = V_n^{(i,s,2)}$$

Similarly $\vec{\boldsymbol{J}}_{\boldsymbol{i}}^{(\boldsymbol{s})}$ can be written as

$$\vec{\boldsymbol{J}}_{\boldsymbol{i}}^{(\boldsymbol{s})} = \vec{\boldsymbol{J}}_{\boldsymbol{i}}^{(\boldsymbol{s})}\Big|_{\boldsymbol{large}} + \hat{Y}_i^{(s)} \vec{\boldsymbol{E}}_{\boldsymbol{i}}^{(\boldsymbol{s})} \tag{4.12}$$

where

$$\begin{cases} \vec{J}_i^{(s)}\Big|_{large} = \sum_{\alpha=1,2} \vec{J}_\alpha^{(i,s)}\Big|_{large} = \sum_{n=1}^{N_1} I_n^{(i,s,1)} \vec{F}_n^{(i,s)} + \sum_{n=1}^{N_2} I_n^{(i,s,2)} \vec{F}_n^{(i,s)} \\ \hat{Y}_i^{(s)} = \hat{Y}_1^{(i,s)} + \hat{Y}_2^{(i,s)} = \sum_{\alpha=1,2} \sum_{n=N_\alpha+1}^{\infty} \left|\vec{F}_n^{(i,s)}\right\rangle Y_n^{(i,s,\alpha)} \left\langle \vec{F}_n^{(i,s)}\right| \end{cases} \quad (4.13)$$

If the same number of active modes are taken in the domains $D_1^{(i,s)}$ and $D_2^{(i,s)}$ i.e. $N_1 = N_2 = N_i$, the current scale changing sources at scale-level S and domain $D_i^{(s)}$ can be rewritten in the simplified form as under:

$$\begin{cases} \vec{J}_i^{(s)}\Big|_{large} = \sum_{n=1}^{N_i} I_n^{(i,s)} \vec{F}_n^{(i,s)} \\ \hat{Y}_i^{(s)} = \sum_{n=N_i+1}^{\infty} \left|\vec{F}_n^{(i,s)}\right\rangle Y_n^{(i,s)} \left\langle \vec{F}_n^{(i,s)}\right| \end{cases} \quad (4.14)$$

where $I_n^{(i,s)} = I_n^{(i,s,1)} + I_n^{(i,s,2)}$ is the amplitude of the n^{th} active mode in $D_i^{(s)}$ and $Y_n^{(i,s)} = Y_n^{(i,s,1)} + Y_n^{(i,s,2)}$ is the total modal admittance viewed by $D_i^{(s)}$ in case of passive modes. The electromagnetic expression given in equation (4.12) can be symbolized by a Norton equivalent Network shown in Figure 4.6(a).

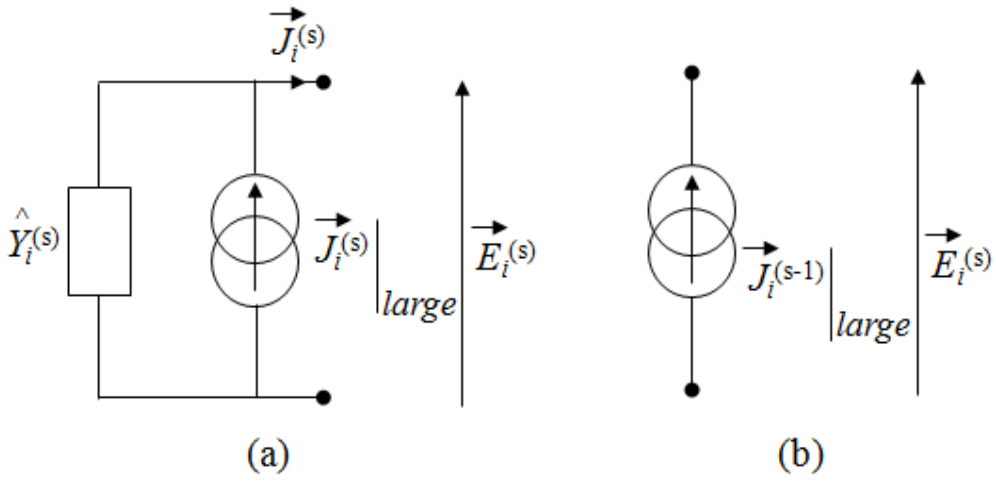

Figure 4.6: Symbolic representations of the current Scale Changing Sources: (a) In the domain $D_i^{(s)}$ (scale level *S*); (b) In the sub-domain $D_j^{(s-1)}$ (Scale level S-1). These sources allow deriving impedance matrix characterizing the Scale-Changing Network that models the electromagnetic coupling between the scale S and the scale S-1.

The *current* Scale-Changing source shown in Figure 4.6 (b) in the sub-domain $D_j^{(s-1)}$ (scale S-1) is defined as the linear combination of $N_j^{(s-1)}$ active modes as follows:

$$\vec{\boldsymbol{J}}_{\boldsymbol{j}}^{(\boldsymbol{s-1})} = \vec{\boldsymbol{J}}_{\boldsymbol{j}}^{(\boldsymbol{s-1})}|_{\boldsymbol{large}} = \sum_{\boldsymbol{n=1}}^{\boldsymbol{N_j^{(s-1)}}} \boldsymbol{I_n^{(j,s-1)}} \vec{\boldsymbol{F}}_{\boldsymbol{n}}^{(\boldsymbol{j,s-1})} \tag{4.15}$$

where $\boldsymbol{I_n^{(j,s-1)}} \vec{\boldsymbol{F}}_{\boldsymbol{n}}^{(\boldsymbol{j,s-1})}$ denotes the current density of the n^{th} active mode in the sub-domain $D_j^{(s-1)}$. Modelling the coupling between the scale *S* and scale *S-1*, the contribution $\vec{J}_j^{(s-1)}|_{fine}$ of passive modes to the total current density $\vec{J}_j^{(s-1)}$ in $D_j^{(s-1)}$ does not act as an actual source. The symbolic representation of the current Scale Changing Source at scale S-1 is shown in Figure 4.6 (b). At this smaller scale, the admittance operator that models the half-regions located on both sides of the discontinuity plane is not taken into consideration unlike at the higher scale level S: this choice allows eliminating redundancies in the theoretical formulation when cascading the Scale-Changing Networks.

Your religion is what you do when the sermon is over.
Quoted in P.S. I Love You

5

Electromagnetic Modeling of Periodic Microstrip Reflectarrays using Scale Changing Technique (SCT)

5.1. Introduction

In the previous chapter, we have developed the basic theoretical and mathematical concepts needed to understand the scale changing approach. Now we will apply these concepts for electromagnetic modeling of a periodic reflectarray. The radiation pattern and the phase shift introduced to a plane wave under any arbitrary incidence at the reflector plane obtained by the Scale-Changing Technique are then validated using a finite element method (FEM) and method of moments (MoM) based commercial simulation tool. By using the set of Floquet harmonics the entire computation domain of a periodic reflectarray is effectively equivalent to solving for a single unit cell of the array.

5.2. Geometry of the Periodic Reflectarray

An infinite planar reflectarray [67] consisting of periodic arrangement of microstrip patches loaded with slots along with its enlarged unit cell is shown in Figure 5.1(a) and (b) respectively. The enlarged unit-cell of the periodic array is depicting the plane wave incidence at the center of the unit cell with propagation vector **k**. The working frequency band for this analysis is 11.7-12.5 GHz. The unit-cell is of square dimensions and is

considered to be bounded by Floquet boundary conditions (i.e., periodic boundary conditions) to simulate an infinite array. All dimensions are assumed to be constant except the width of the metallic patch (W_p) and the length of the slot (L_S) which vary and therefore result in five configurations having distinct geometries (Table 5.1). This planar periodic array unit cell is placed on a 2.17mm thick dielectric with a ground plane at the bottom. All the design parameters of this periodic array phase shifter cell have been selected on the basis of a very comprehensive scattering parameters study using the equivalent electrical circuit model fully explained in chapter 2 and shown in Figure 2.12. This equivalent electrical circuit model is proved to be very practical and fast parametric design tool for the reflectarrays unit cells as compared to the full wave simulation tools.

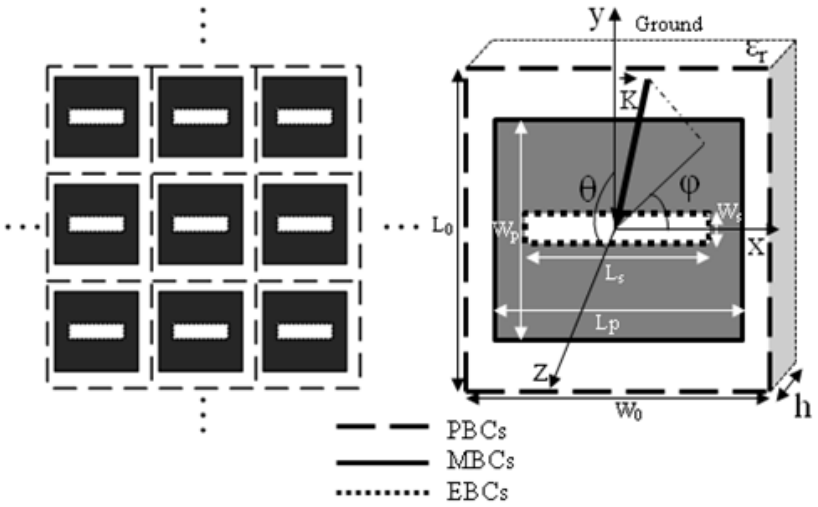

(a) (b)

Figure 5.1: (a) A two dimensional periodic reflectarray (b) Enlarged unit-cell of the array with dimensions: $L_0=W_0=15$mm, $W_p=12$mm, $L_s=1$mm, W_p and L_s are variable. Substrate thickness h=2.17mm (εr=3.38), PBCs, MBCs and EBCs stand for periodic, magnetic and electric boundary conditions respectively.

Table 5.1

Five distinct geometries by varying patch width (Wp) and slot length (Ls)

Configuration	1	2	3	4	5
Wp (mm)	2	4	8	10	12
Ls (mm)	7	6	8	6	12

The computation of phase-shift introduced to an incident plane-wave by unit-cell reflectors when bounded by periodic boundary conditions is an essential step of a reflectarray design process. Characterization of each unit-cell under infinite array environment is considered as an approximation of the behavior of that cell in the real finite-sized array. Therefore we will consider here the problem of finding the scattering matrix of a planar reflector under infinite array conditions.

5.3. Application of Scale-Changing Technique

5.3.1. Partitioning of the Discontinuity Plane

Application of the scale changing technique requires the partitioning of the discontinuity plane. In this case of modeling a single unit cell, simplicity of the cell geometry allows us to define three nested scales as shown in Figure 5.2. In this simple case we have only one domain at each scale-level. Domain $D_1^{(3)}$ of scale-level 3 encompasses the entire reflector plane. Domain $D_1^{(2)}$ at second scale-level consists of patch and slot whereas the domain $D_1^{(1)}$ on the bottom scale is comprised of slot only.

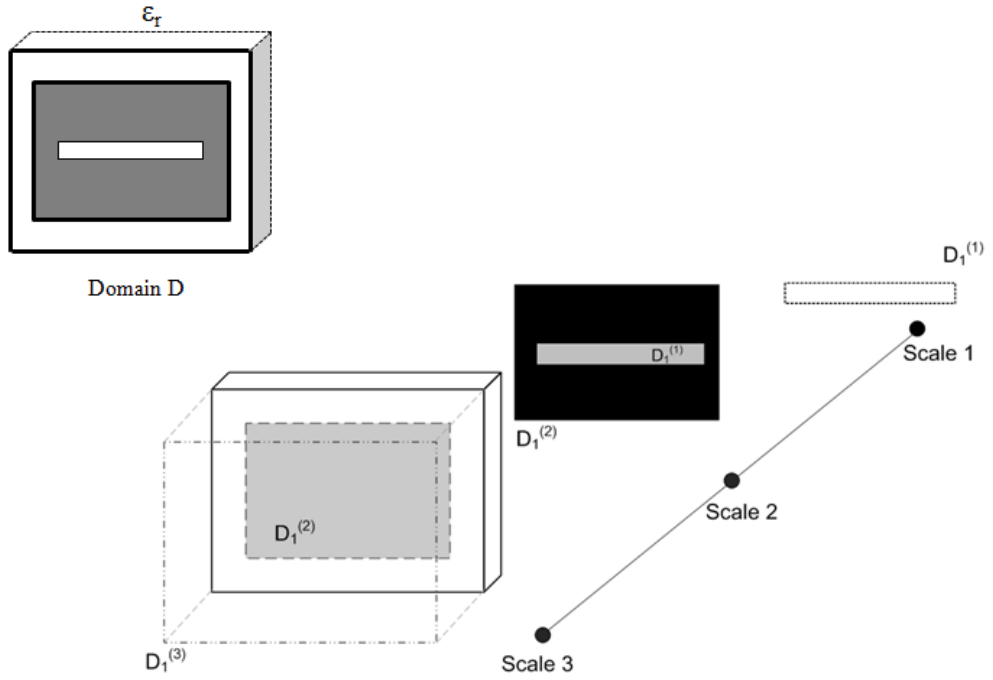

Figure 5.2: Partitioning the discontinuity plane D of the planar reflector in its constituent domains and sub-domains at three scales, white portions represent dielectric, black represents metal and grey parts are mere projections of the immediate sub-domains.

This problem requires the computation of one scale-changing network i.e. between the scale-level 3 and scale-level 2 modeling the interaction between the active modes of $D_1^{(3)}$ and $D_1^{(2)}$ and a multi-modal surface impedance network (or surface impedance multipole) between Scale level 2 and 1. The SCN will be cascaded with the surface impedance multipole computed on the active modes of $D_1^{(2)}$. This cascading is depicted in Figure 5.3.

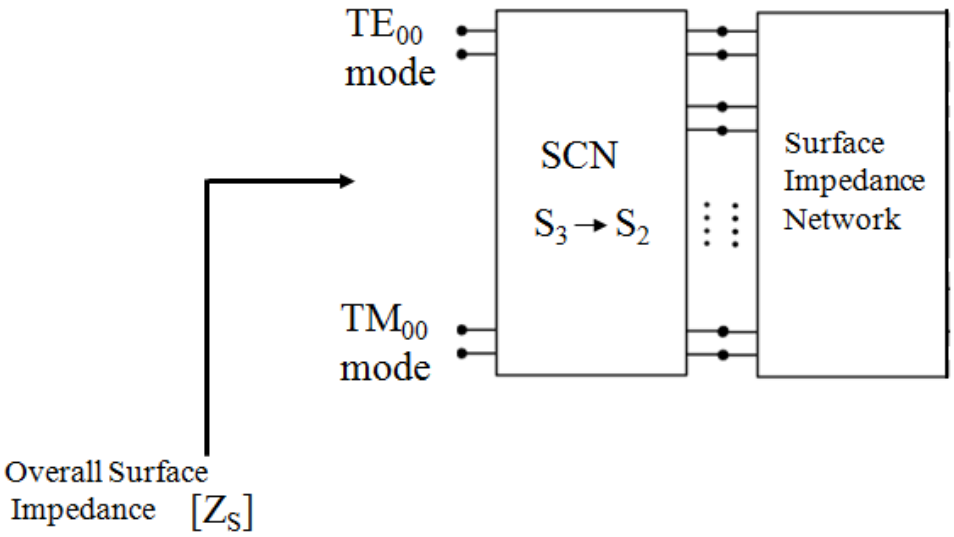

Figure 5.3: Global simulation of the planar reflector involves the cascade of the scale-changing network multipole and the surface impedance multipole.

The two multipoles can be computed separately by decomposing the original problem in two separate problems each modeling two successive scale-levels as shown in the Figure 5.4. The resolution of the structure in Figure 5.4 (a) will give the scale changing network multipole while the surface impedance network can be obtained from the structure of Figure 5.4 (b).

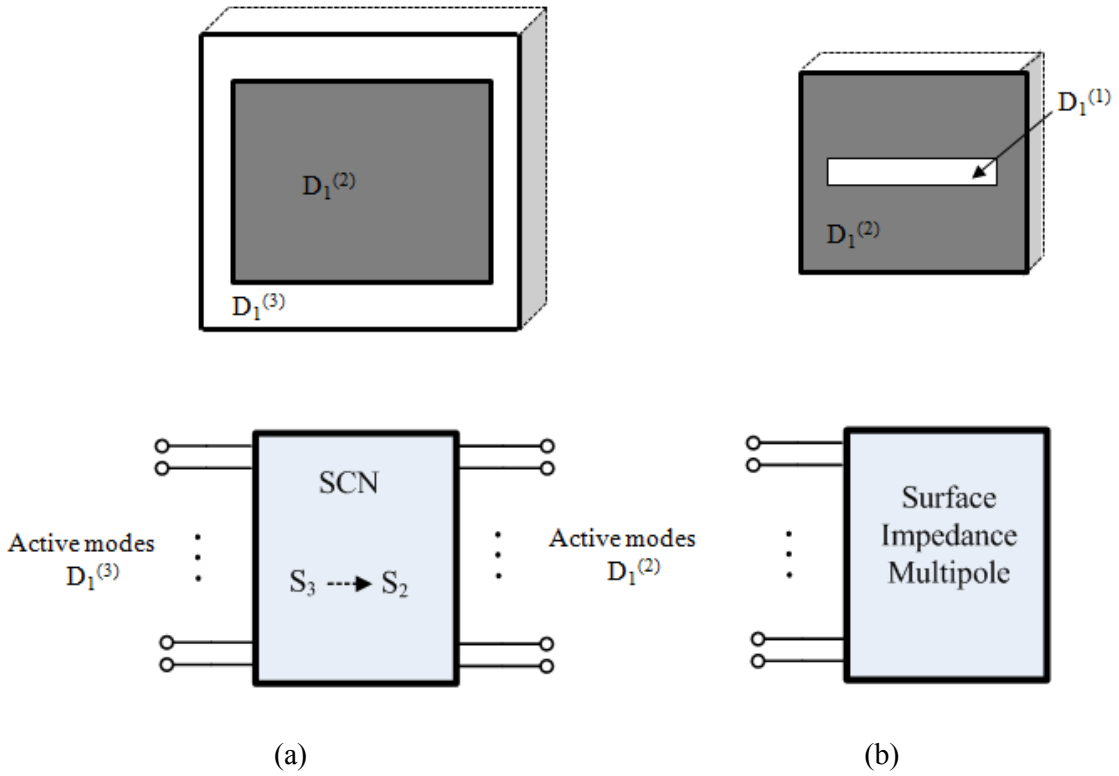

Figure 5.4: Decomposition of the problem in two sub-problems. (a) SCN is computed from the structure shown above (b) Surface Impedance Multipole is computed from the problem involving patch and slot domain only.

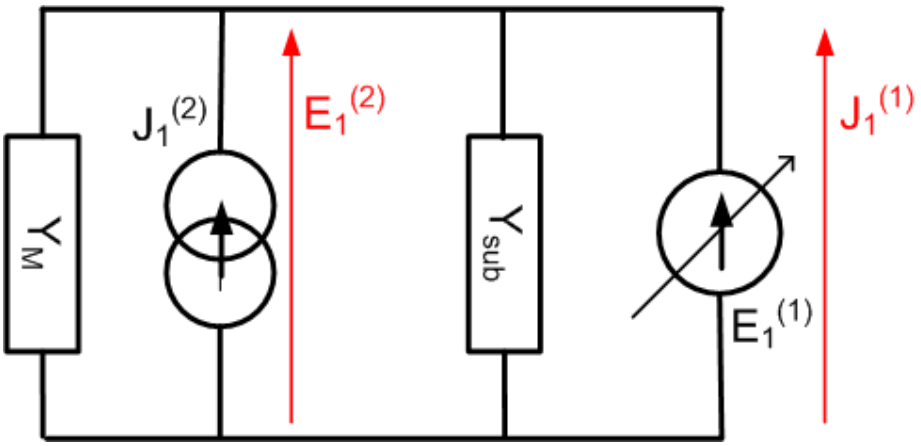

Figure 5.5: Equivalent circuit diagram to compute the surface impedance multi-modal network of Figure 5.4(b).

5.3.2. Surface Impedance Multipole Computation

In the surface impedance multipole presented in Figure 5.4 (b), the ports on the LHS represent the active modes in domain $D_1^{(2)}$ of scale-level 2. The boundary value problem in this case is shown in the same figure above the surface impedance multipole. Here we have

the slot domain $D_1^{(1)}$ nested inside the patch domain $D_1^{(2)}$, both resting on a dielectric slab of relative permittivity $\boldsymbol{\varepsilon_r}$. This boundary value problem can be represented in terms of the equivalent circuit of Figure 5.5.

The left part of the circuit i.e. the source $J_1^{(2)}$ along with the admittance operator $\hat{Y}_M$ is the Norton equivalent excitation defined on the discrete orthogonal modal-basis of $D_1^{(2)}$ ($\vec{\boldsymbol{F}}_{\boldsymbol{n}}^{(1,2)}$).

$$\begin{cases} \vec{\boldsymbol{J}}_1^{(2)} = \vec{\boldsymbol{H}}_1^{(2)} \times \vec{\mathbf{n}} = \sum_{\boldsymbol{n=1}}^{\boldsymbol{N}^{(1,2)}} I_n^{(1,2)} \vec{\boldsymbol{F}}_{\boldsymbol{n}}^{(1,2)} \\ \vec{\boldsymbol{E}}_1^{(2)} = \sum_{\boldsymbol{n=1}}^{\infty} V_n^{(1,2)} \vec{\boldsymbol{F}}_{\boldsymbol{n}}^{(1,2)} \end{cases} \tag{5.1}$$

$$\hat{Y}_M = \sum_{\boldsymbol{n=N}^{(1,2)}+\boldsymbol{1}}^{\infty} \left| \vec{\boldsymbol{F}}_{\boldsymbol{n}}^{(1,2)} \right\rangle Y_n^{(1,2)} \left\langle \vec{\boldsymbol{F}}_{\boldsymbol{n}}^{(1,2)} \right| \tag{5.2}$$

$\boldsymbol{N}^{(1,2)}$ is the number of active modes of the domain $D_1^{(2)}$. $\boldsymbol{I}^{(1,2)}$ and $\boldsymbol{V}^{(1,2)}$ are the column vectors of size $\boldsymbol{N}^{(1,2)}$ listing the coefficients in the matrix form.

$$I^{(1,2)} = \begin{bmatrix} I_1^{(1,2)} \\ \vdots \\ I_{N^{(1,2)}}^{(1,2)} \end{bmatrix} \quad , \quad V^{(1,2)} = \begin{bmatrix} V_1^{(1,2)} \\ \vdots \\ V_{N^{(1,2)}}^{(1,2)} \end{bmatrix} \tag{5.3}$$

$Y_n^{(1,2)}$ is the admittance of nth mode. The expressions for the modal admittances for TE and TM modes are as follows:

$$Y_n^{(i)} = \begin{cases} \dfrac{\gamma_n^{(i)}}{j\omega\mu_0} & TE\ modes \\ \dfrac{j\omega\varepsilon}{\gamma_n^{(i)}} & TM\ modes \end{cases} \tag{5.4}$$

with $\gamma_n^{(i)}$ the propagation constant of nth mode in medium i, The expression of $\gamma^{(i)}$ for a TE or TM mode is

$$\gamma^{(i)} = \sqrt{k_c^2 - k_0^2 \varepsilon_r^{(i)}} \tag{5.5}$$

The dielectric side of the discontinuity plane is modeled as a shorted dielectric waveguide. Therefore the operator $\hat{Y}_{sub}$ represents the modes of the domain $D_1^{(2)}$ short circuited by ground through the dielectric. If h is the thickness of the dielectric and γ_{nsub} the propagation constant of nth mode in the substrate then the admittance operator can be written as

$$\hat{Y}_{sub} = \sum_{n=1}^{\infty} \left| \vec{F}_n^{(1,2)} \right\rangle Y_{nsub}^{(1,2)} \coth(\gamma_{nsub} h) \left\langle \vec{F}_n^{(1,2)} \right| \tag{5.6}$$

The electric field source $E_1^{(1)}$ is a virtual source defined in the slot domain $D_1^{(1)}$ (scale 1). The name *virtual sources* imply that unlike real sources they deliver no electromagnetic energy and are therefore represented with an arrow across the source. The virtual sources serve to represent two different boundary conditions at a time in one equivalent circuit. For example in this case the field source $E_1^{(1)}$ defined in $D_1^{(1)}$ models dielectric boundary conditions while the dual quantity $J_1^{(1)}$ models the perfect electric boundary conditions of the metallic surface.

It is to be noted here that both quantities $E_1^{(1)}$ and $J_1^{(1)}$ cannot be non-zero at the same time and therefore the energy supplied by the source which is the product of the two quantities **E** and **J** is zero everywhere [35]. $E_1^{(1)}$ serves to represent the tangential electric field in the slot domain on an orthogonal set of entire domain trial functions [63] defined in $D_1^{(1)}$ ($\vec{F}_n^{(1,1)}$) as under.

$$\begin{cases} \vec{E}_1^{(1)} = \sum_{n=1}^{N^{(1,1)}} V_n^{(1,1)} \vec{F}_n^{(1,1)} \\ \vec{J}_1^{(1)} = \vec{0} \end{cases} \quad in\ D_1^{(1)} \tag{5.7}$$

$N^{(1,1)}$ being the number of active modes in $D_1^{(1)}$, The column-vector $V^{(1,1)}$ of dimensions $N^{(1,1)}$ lists the weights of the test functions.

$$V^{(1,1)} = \begin{bmatrix} V_1^{(1,1)} \\ \vdots \\ V_{N^{(1,1)}}^{(1,1)} \end{bmatrix} \tag{5.8}$$

Following matrix equations can be written from the equivalent circuit of Figure 5.5 by using Kirchoff laws.

$$\begin{bmatrix} \mathrm{E}_1^{(2)} \\ \mathrm{J}_1^{(1)} \end{bmatrix} = \begin{bmatrix} 0 & 1 \\ -1 & \hat{Y}_M + \hat{Y}_{sub} \end{bmatrix} \times \begin{bmatrix} \mathrm{J}_1^{(2)} \\ \mathrm{E}_1^{(1)} \end{bmatrix} \tag{5.9}$$

This boundary value problem may be solved by applying the Galerkin method. The above matrix equation can therefore be written in terms of coefficient matrices.

$$\begin{bmatrix} V^{(1,2)} \\ 0 \end{bmatrix} = \begin{bmatrix} 0 & P_1 \\ -P_1^T & P_1^T Y_{sub} P_1 + P_2^T (Y_M + Y_{sub}) P_2 \end{bmatrix} \times \begin{bmatrix} I^{(1,2)} \\ V^{(1,1)} \end{bmatrix} \tag{5.10}$$

T denotes the complex conjugate transpose of a matrix, $[P_1]$ is the projection matrix of dimensions $N^{(1,2)} \times N^{(1,1)}$ of active modes of modal-basis $\vec{\boldsymbol{F}}_{\boldsymbol{n}}^{(1,2)}$on $\vec{\boldsymbol{F}}_{\boldsymbol{n}}^{(1,1)}$.

$$[P_1] = \begin{bmatrix} \langle F_1^{(1,2)}, F_1^{(1,1)} \rangle & \cdots & \langle F_1^{(1,2)}, F_{N^{(1,1)}}^{(1,1)} \rangle \\ \vdots & \ddots & \vdots \\ \langle F_{N^{(1,2)}}^{(1,2)}, F_1^{(1,1)} \rangle & \cdots & \langle F_{N^{(1,2)}}^{(1,2)}, F_{N^{(1,1)}}^{(1,1)} \rangle \end{bmatrix} \tag{5.11}$$

Similarly $[P_2]$ is the projection matrix of dimensions $\left(M^{(1,2)} - N^{(1,2)}\right) \times N^{(1,1)}$ of passive modes of modal-basis $\vec{\boldsymbol{F}}_{\boldsymbol{n}}^{(1,2)}$on $\vec{\boldsymbol{F}}_{\boldsymbol{n}}^{(1,1)}$.

$$[P_2] = \begin{bmatrix} \langle F_{N^{(1,2)}+1}^{(1,2)}, F_1^{(1,1)} \rangle & \cdots & \langle F_{N^{(1,2)}+1}^{(1,2)}, F_{N^{(1,1)}}^{(1,1)} \rangle \\ \vdots & \ddots & \vdots \\ \langle F_{M^{(1,2)}}^{(1,2)}, F_1^{(1,1)} \rangle & \cdots & \langle F_{M^{(1,2)}}^{(1,2)}, F_{N^{(1,1)}}^{(1,1)} \rangle \end{bmatrix} \tag{5.12}$$

$[Y_M]$ is a diagonal matrix of passive modal admittances. Its dimensions are $\left(M^{(1,2)} - N^{(1,2)}\right) \times \left(M^{(1,2)} - N^{(1,2)}\right)$

$$[Y_M] = \begin{bmatrix} Y_{N^{(1,2)}+1}^{(1,2)} & \cdots & 0 \\ \vdots & \ddots & \vdots \\ 0 & \cdots & Y_{M^{(1,2)}}^{(1,2)} \end{bmatrix} \tag{5.13}$$

$[Y_M]$ is a diagonal matrix of dimensions $M^{(1,2)} \times M^{(1,2)}$

$$[Y_{sub}] = \begin{bmatrix} Y_{1sub}^{(1,2)} \coth(\gamma_{1sub} h) & \cdots & 0 \\ \vdots & \ddots & \vdots \\ 0 & \cdots & Y_{M^{(1,2)}sub}^{(1,2)} \coth(\gamma_{Msub} h) \end{bmatrix} \quad (5.14)$$

From equation (**5.10**) surface impedance can be written as

$$[Zs^{(1,2)}] = P_1 \times (P_1^T Y_{sub} P_1 + P_2^T (Y_M + Y_{sub}) P_2)^{-1} \times P_1^T \quad (5.15)$$

with

$$[V^{(1,2)}] = [Zs^{(1,2)}] \times [I^{(1,2)}] \quad (5.16)$$

5.3.3. Scale Changing Network Computation

Equivalent circuit of Figure 5.6 represents the boundary value problem of Figure 5.4 (a). In this case the discontinuity plane represented by the middle branch is modeled with two sources. The current source $j_e^{(2)}$ is the virtual source defined in $D_1^{(2)}$ modeling perfect electric boundary conditions while the electric field source $e^{(2)}$ is the scale-changing source modeling the electromagnetic coupling with the sub-domain as explained in chapter 4.

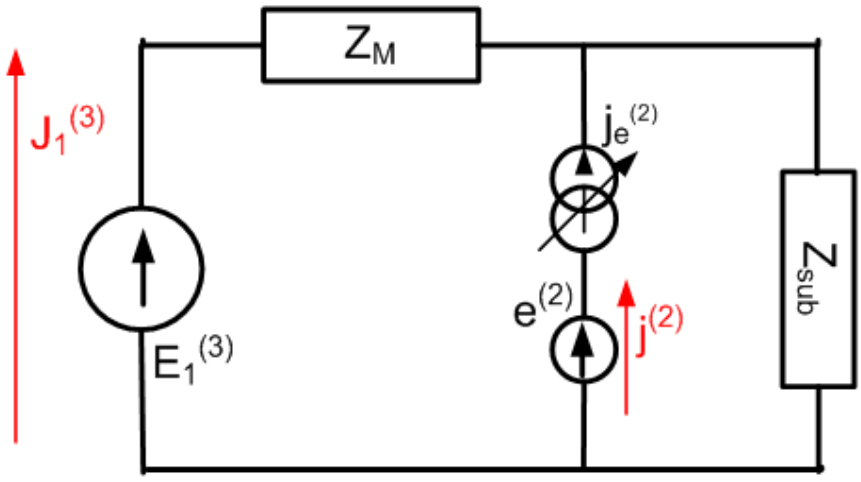

Figure 5.6: Equivalent circuit diagram to compute the scale-changing network multipole of Figure 5.4(a).

Since both sources $j_e^{(2)}$ and $e^{(2)}$ exist in the same domain and at same scale level, hence by assuming that both sources are defined by the same set of orthogonal modes the equivalent circuit can be simplified to that of Figure 5.7 [68].

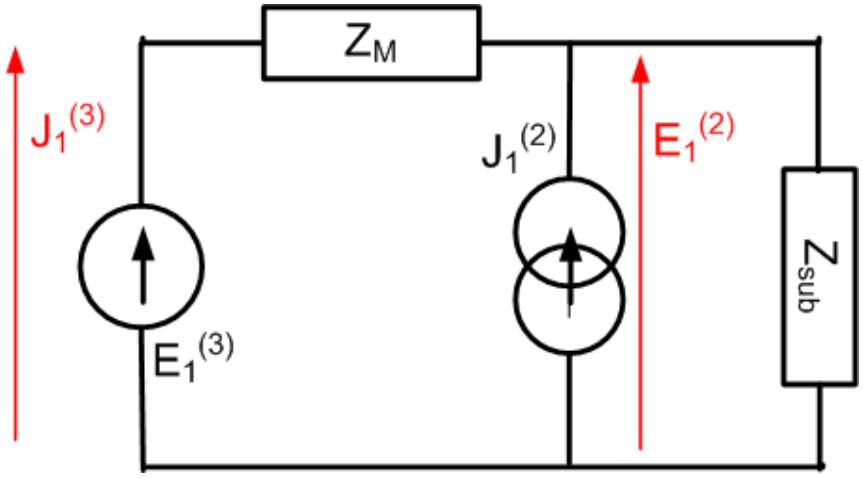

Figure 5.7: Simplified equivalent circuit of Figure 5.6.

$\vec{E}_1^{(3)}$ is the excitation source defined on $N^{(1,3)}$ active modes of the orthogonal modal-basis of $D_1^{(3)}$ ($\vec{F}_n^{(1,3)}$). Floquet modal basis is chosen at this scale to model the periodicity of the infinite array. Floquet modes TE_{00} and TM_{00} are chosen to represent the two plane-wave polarizations. The expressions for the Floquet modal basis can be found in Appendix A.

$$\begin{cases} \vec{E}_1^{(3)} = \sum_{n=1}^{N^{(1,3)}} V_n^{(1,3)} \vec{F}_n^{(1,3)} \\ \vec{J}_1^{(3)} = \sum_{n=1}^{\infty} I_n^{(1,3)} \vec{F}_n^{(1,3)} \end{cases} \tag{5.17}$$

$V^{(1,3)}$ and $I^{(1,3)}$ are the column vectors of dimensions $N^{(1,3)}$,

$$I^{(1,3)} = \begin{bmatrix} I_1^{(1,3)} \\ \vdots \\ I_{N^{(1,3)}}^{(1,3)} \end{bmatrix} \qquad V^{(1,3)} = \begin{bmatrix} V_1^{(1,3)} \\ \vdots \\ V_{N^{(1,3)}}^{(1,3)} \end{bmatrix} \tag{5.18}$$

Operators $\hat{Z}_M$ and $\hat{Z}_{sub}$ are defined as usual

$$\begin{cases} \hat{Z}_M = \sum_{n=N^{(1,3)}+1}^{\infty} \left|\vec{F}_n^{(1,3)}\right\rangle Z_n^{(1,3)} \left\langle\vec{F}_n^{(1,3)}\right| \\ \hat{Z}_{sub} = \sum_{n=1}^{\infty} \left|\vec{F}_n^{(1,3)}\right\rangle Z_{nsub}^{(1,3)} \tanh(\gamma_{nsub} h) \left\langle\vec{F}_n^{(1,3)}\right| \end{cases} \tag{5.19}$$

with modal impedances defined as

$$Z_n^{(i)} = \begin{cases} \frac{j\omega\mu_0}{\gamma_n^{(i)}} & TE\ modes \\ \frac{\gamma_n^{(i)}}{j\omega\varepsilon} & TM\ modes \end{cases} \tag{5.20}$$

Using Kirchoff circuit laws following matrix equation can be written from the equivalent circuit of Figure 5.7.

$$\begin{bmatrix} \mathrm{J}_1^{(3)} \\ \mathrm{E}_1^{(2)} \end{bmatrix} = \begin{bmatrix} \left(\hat{Z}_M + \hat{Z}_{sub}\right)^{-1} & -\hat{Z}_{sub}\left(\hat{Z}_M + \hat{Z}_{sub}\right)^{-1} \\ \hat{Z}_{sub}\left(\hat{Z}_M + \hat{Z}_{sub}\right)^{-1} & \hat{Z}_M\hat{Z}_{sub}\left(\hat{Z}_M + \hat{Z}_{sub}\right)^{-1} \end{bmatrix} \times \begin{bmatrix} \mathrm{E}_1^{(3)} \\ \mathrm{J}_1^{(2)} \end{bmatrix} \tag{5.21}$$

Applying Galerkin method we get:

$$\begin{bmatrix} I^{(1,3)} \\ V^{(1,2)} \end{bmatrix} = \begin{bmatrix} H11 & H12 \\ H21 & H22 \end{bmatrix} \times \begin{bmatrix} V^{(1,3)} \\ I^{(1,2)} \end{bmatrix} \tag{5.22}$$

with projection matrices defined as under:

$[H_{11}]$ is a diagonal matrix of dimensions $N^{(1,3)} \times N^{(1,3)}$

$$[H_{11}] = \begin{bmatrix} \left(Z_{1sub}^{(1,3)} \tanh\left(\gamma_{1sub}h\right)\right)^{-1} & \cdots & 0 \\ \vdots & \ddots & \vdots \\ 0 & \cdots & \left(Z_{N^{(1,3)}sub}^{(1,3)} \tanh\left(\gamma_{N^{(1,3)}sub}h\right)\right)^{-1} \end{bmatrix} \tag{5.23}$$

$[H_{12}]$ is a unitary matrix of dimensions $N^{(1,3)} \times N^{(1,2)}$

$$[H_{12}] = \begin{bmatrix} -1 & \cdots & 0 \\ \vdots & \ddots & \vdots \\ 0 & \cdots & -1 \end{bmatrix} \tag{5.24}$$

with $[H_{21}] = -[H_{12}]^T$ and $[H_{22}] = P_2^T Z P_2$

$[P_2]$ is the projection matrix of dimensions $\left(M^{(1,3)} - N^{(1,3)}\right) \times N^{(1,2)}$ of passive modes of modal-basis $\vec{\boldsymbol{F}}_{\boldsymbol{n}}^{(1,3)}$ on $\vec{\boldsymbol{F}}_{\boldsymbol{n}}^{(1,2)}$.

$$[P_2] = \begin{bmatrix} \langle F^{(1,3)}_{N^{(1,3)}+1}, F^{(1,2)}_1 \rangle & \cdots & \langle F^{(1,3)}_{N^{(1,3)}+1}, F^{(1,2)}_{N^{(1,2)}} \rangle \\ \vdots & \ddots & \vdots \\ \langle F^{(1,3)}_{M^{(1,3)}}, F^{(1,2)}_1 \rangle & \cdots & \langle F^{(1,3)}_{M^{(1,3)}}, F^{(1,2)}_{N^{(1,2)}} \rangle \end{bmatrix} \tag{5.25}$$

and Z is a diagonal matrix of size $\left(M^{(1,3)} - N^{(1,3)}\right) \times \left(M^{(1,3)} - N^{(1,3)}\right)$

$$[Z] = \begin{bmatrix} \frac{Z^{(1,3)}_{N^{(1,3)}+1} Z^{(1,3)}_{N^{(1,3)}sub+1} \tanh\left(\gamma_{N^{(1,3)}sub+1} h\right)}{Z^{(1,3)}_{N^{(1,3)}+1} + Z^{(1,3)}_{N^{(1,3)}sub+1} \tanh\left(\gamma_{N^{(1,3)}sub+1} h\right)} & \cdots & 0 \\ \vdots & \ddots & \vdots \\ 0 & \cdots & \frac{Z^{(1,3)}_{M^{(1,3)}} Z^{(1,3)}_{M^{(1,3)}sub} \tanh\left(\gamma_{M^{(1,3)}sub} h\right)}{Z^{(1,3)}_{M^{(1,3)}} + Z^{(1,3)}_{M^{(1,3)}sub} \tanh\left(\gamma_{M^{(1,3)}sub} h\right)} \end{bmatrix} \tag{5.26}$$

5.3.4. Network Cascade

In this step cascade of both networks of Figure 5.4(a) and (b) is performed to obtain the overall surface impedance $[Z_S]$ of the complete structure as viewed by the excitation modes at the surface of the discontinuity plane (see Figure 3). Consider the final equations of (5.16) and (5.22) as under:

$$\left[V^{(1,2)}\right] = -\left[Zs^{(1,2)}\right] \times \left[I^{(1,2)}\right] \tag{5.27}$$

$$\begin{bmatrix} I^{(1,3)} \\ V^{(1,2)} \end{bmatrix} = \begin{bmatrix} H11 & H12 \\ H21 & H22 \end{bmatrix} \times \begin{bmatrix} V^{(1,3)} \\ I^{(1,2)} \end{bmatrix} \tag{5.28}$$

Note the negative sign in the surface impedance multipole equation (5.27) comes to signify the reversal of the currents in the cascading procedure. From the above two equations (5.27) and (5.28) following equation for the overall multipole can be extracted:

$$\left[I^{(1,3)}\right] = [Ys] \times \left[V^{(1,3)}\right] \tag{5.29}$$

With $[Ys]$ is the overall admittance of the complete phase shifter cell and is given by:

$$[Ys] = [H_{11}] + [H_{12}]\left(\left[Zs^{(1,2)}\right] + [H_{22}]\right)^{-1}[H_{12}]^T \tag{5.30}$$

Scattering parameter matrix is calculated by using

$$[S] = \left(\sqrt{[Z_M]}\right)^{-1}\left([Z_S] - [Z_M]\right) \times \left([Z_S] + [Z_M]\right)^{-1}\sqrt{[Z_M]} \tag{5.31}$$

with $[Z_S] = [Ys]^{-1}$ and $[Z_M]$ is the modal impedance of excitation modes in air.

5.4. Results Discussion

A planar unit-cell reflector depicted in Figure 5.1(b) has been modeled and simulated using the approach outlined in the previous Section. The discontinuity plane of the reflector cell is comprised of slotted patch centered on a grounded dielectric layer. All the dimensions and specifications are indicated in the figure caption. The simulations have been performed for 5 distinct unit-cell geometries obtained by varying metallic patch width (Wp) and slot length (Ls) as given in Table 5.1. Normal plane wave with electric field linearly polarized perpendicular to slot-length is considered as excitation source.

5.4.1. Convergence Study

As described in the previous section, the tangential electromagnetic fields in different regions of the discontinuity plane is defined by the orthogonal set of modes of the domain. Precise description of field quantities would require adequate number of active and passive modes to be considered at each scale-level. Appropriate number of modes may be chosen by a systematic convergence study. This study involves plotting reflection coefficient phase results with respect to the number of modes at each domain to find out the appropriate number for which the results converge.

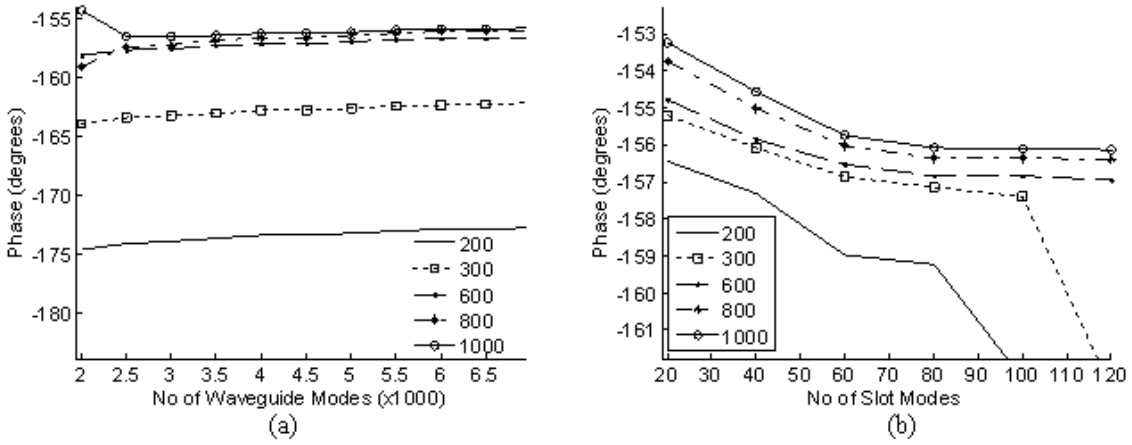

Figure 5.8: Convergence study of the phase of reflection coefficient for configuration 3 (Lp, Ws) => (8, 8), frequency 12.1GHz: (a) Convergence with respect to the number of modes in the periodic waveguide (legend indicates number of patch modes); (b) Convergence with respect to number of modes in the slot (legend indicates number of patch modes).

Convergence study results for the sixth reflector-cell configuration at the centre frequency of 12.1GHz are shown in Figure 5.8. Figure 5.8 (a) shows the convergence of the reflection coefficient phase with respect to the number of active modes $N^{(1,2)}$ in the patch domain $D_1^{(2)}$ and the number of passive modes $M^{(1,3)}$ taken inside the periodic waveguide (discontinuity domain $D_1^{(3)}$. It is apparent that there is no significant variation in phase results for waveguide modes greater than 2500. Similarly around 600 active modes in the patch domain are required for the phase convergence with in 3º margin.

Figure 5.8 (b) plots the convergence curves with respect to patch active modes and the number of active modes $N^{(1,1)}$ taken in the slot domain $D_1^{(1)}$. Here, again the flat part of the curves demonstrates the convergence of reflected phase. It is evident from the curves that convergence is achieved if the number of patch active modes is taken between 600 and 1000 and the number of slot active modes is taken between 80 and 120. However, if the number of slot active modes exceeds a certain limit, matrices become ill-conditioned leading to the loss of convergence as can be seen by the sudden drop in two lower curves. This numerical problem can be attributed to the use of entire domain trial functions and is analogous to the one observed classically in the Mode Matching Technique [69].

For this reflector-cell configuration we have chosen 5000 waveguide modes, 1000 antenna active modes and 120 slot active modes. For these numbers, the convergence achieved is within 1º margin. It should be noted here that the phase convergence is not very

sensitive to number of passive modes in a domain as long as a significant number is taken. 1000 passive modes were taken in the patch domain $M^{(1,2)}$ for the simulation results presented in this section. However a rigorous convergence study is required to determine the number of active modes which characterize the mutual coupling between different scales.

5.4.2. Scattering Parameters Results

The five distinguished unit-cell configurations are simulated using Scale-Changing Technique over the frequency range of 11.7GHz to 12.5GHz using the convergence results at the centre frequency for each configuration. Same structures were simulated using FEM and MoM based commercial software (HFSS *version* 13) under periodic boundary conditions and Floquet port excitation. Figure 9(a) plots the phase curves for the fourth configuration under normal incidence; the maximum difference between SCT and HFSS results is in case of S22 (y-polarization), that is of 4°. Figures 5.9(b) and (c) plot the phase results for all five configurations with respect to different incidence angles at centre frequency (12.1GHz). The angle theta (θ) varies from 0° to 40° while the angle phi (φ) is taken initially equal to 0° for simplicity. Table 5.2 lists the values of the reflected phase obtained by SCT and HFSS simulations for all five configurations under different pairs of wave incidence. Again both results are in good agreement with maximum difference of 3°. The results for cross polarization (S12 and S21) in dBs are shown in Table 5.3. The values of cross polarization under both SCT and HFSS remains below than -40dB, which is an excellent mark regarding design purposes.

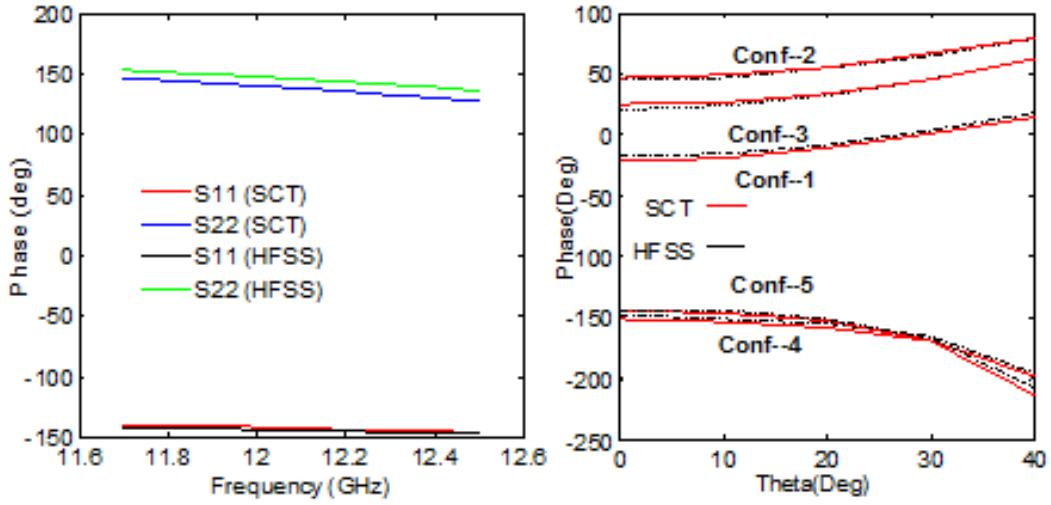

(a) (b)

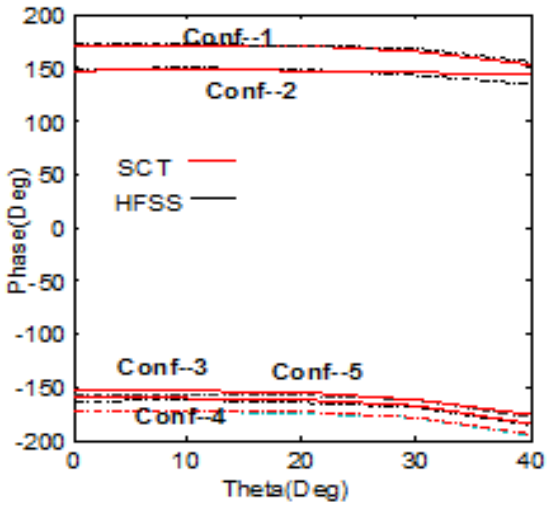

(c)

Figure 5.9: Comparison of the reflected phase obtained by SCT and HFSS (a) over the whole frequency band (11.7-12.5 GHz) under normal incidence, for 4th configuration and both polarizations: S11 (x-Polarization), S22 (y-Polarization); (b) and (c): phase results at center frequency (12.1GHz) for all five configurations under oblique incidence (a) x-Polarization (b) y-Polarization

Table 5.2

Comparison of the reflected phase obtained by SCT and HFSS at middle frequency (12.5 GHz) under different plane wave incidences for all five configurations.

$\theta i, \varphi i$	30,50		70,30		70,0		50,50		30,80	
Technique	SCT	HFSS	SCT	HFSS	SCT	HFSS	SCT	HFSS	SCT	HFSS
Config-1	118.4	121.2	137.5	140.2	88.1	85.5	134.2	137.9	131.2	128.6
Config-2	131.7	131.3	157.2	157.3	78.3	70.4	144.6	145.2	125.3	132.5
Config-3	131.3	130.9	158.4	157.8	102.2	120.3	143.4	144.1	156.8	151.4
Config-4	158.5	161.5	172.3	171.6	142.6	142.1	163.1	163	167.2	163.1
Config-5	-152	-154.1	-172	-170	-155	-157.3	-160	-162	-178	-162

Table 5.3

Comparison of the cross polarization (in decibels) obtained by SCT and HFSS at middle frequency (12.1 GHz) for all five configurations

$\varphi_i=\theta°, \theta_i$	0°		10°		20°		30°		40°	
Technique	***SCT***	***HFSS***	***SCT***	***HFSS***	***SCT***	***HFSS***	***SCT***	***HFSS***	***SCT***	***HFSS***
Config-1	-54.43	-59.89	-63.97	-62.01	-57.95	-58.55	-44.43	-54.31	-54.31	-58.20
Config-2	-60.00	-54.62	-53.09	-54.45	-53.97	-50.44	-42.43	-54.19	-41.19	-49.01
Config-3	-53.97	-49.00	-51.93	-54.45	-48.97	-52.54	-63.09	-65.20	-52.20	-63.55
Config-4	-50.75	-49.97	-55.67	-55.02	-47.95	-53.81	-51.95	-59.76	-59.76	-50.51
Config-5	-57.07	-51.72	-55.67	-59.62	-46.95	-45.53	-52.63	-46.62	-46.62	-65.76

5.4.3. Radiation Pattern Results

To determine the electric field scattered by the surface impedance $[Z_S]$ of the whole structure when illuminated by plane wave, the equivalent surface current density is computed from the resolution of the following matrix equation derived from the Integral Equation Formulation of the boundary value problem by applying SCT:

$$\left[V^{inc}\right] - \left(\left[Z_{space}\right] * \left[I_{eq}\right]\right) = [Z_s] * \left[I_{eq}\right] \tag{5.32}$$

$$\left[I_{eq}\right] = \left(\left[Z_{space}\right] + [Z_s]\right)^{-1}\left[V^{inc}\right] \tag{5.33}$$

$\left[Z_{space}\right]$ is the matrix representation of the free space dyadic Green function, $\left[V^{inc}\right]$ designate the column vectors of entire-domain basis functions components of the incident plane wave and the vector column $\left[I_{eq}\right]$ represents the unknown coefficients of surface current density. Please see chapter 6 for detailed SCT Integral Equation Formulation for EM far-field Scattering.

The far-field radiation patterns at 12.1 GHz frequency are presented in Figure 5.10. Again the results of SCT are in excellent agreement with that of HFSS. The SCT results have been obtained with a significant reduction in terms of computation time and memory resources. The simulation times for this specific periodic reflectarray problem (i.e., unit cell simulation problem) are 93 seconds and 766 seconds for the SCT and HFSS, respectively. The factor of time and memory becomes more critical when simulating finite structures and the SCT is also proving itself a very efficient technique for finite-sized large reflectarray problems, as will be discussed in the following Chapter. Finally, by keeping in view the close agreement between SCT and HFSS, we can conclude that the scale changing technique delivers its advantages without the loss of accuracy in results.

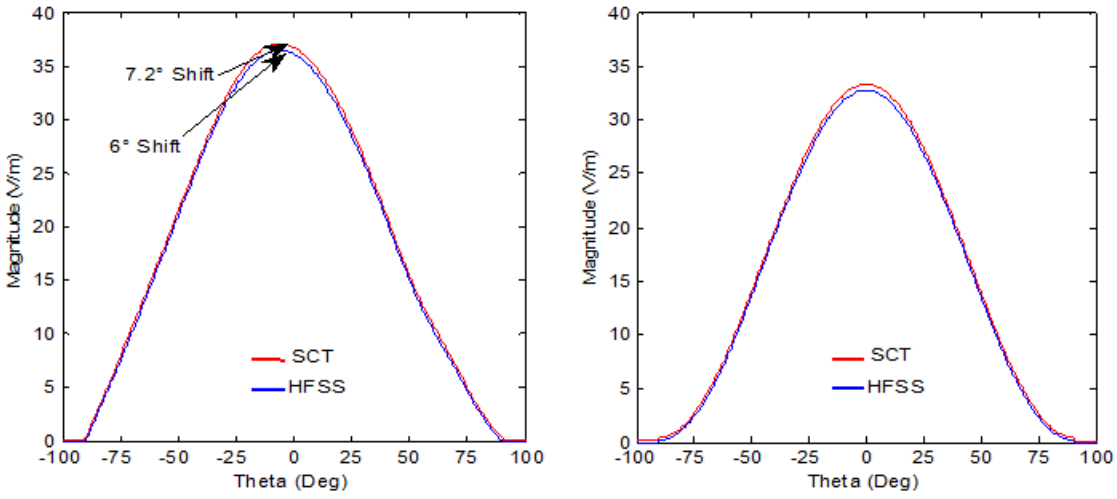

(a) (b)

Figure 5.10: Scattered Electric Field in the far-field zone obtained from the SCT and HFSS under oblique incidence (θ=20°, φ=0°) at 12.1 GHz (a) E-Plane (b) H-Plane

5.5. Conclusions

In this chapter we have presented the underlying theory of the Scale-Changing Technique and explained certain concepts involved in the application of this technique to the planar structures. It has been shown that the Scale-Changing Technique is particularly suited for the applications that require large complex planar geometries with patterns varying over a wide range of scale. The concept of scale-changing network (SCN) to model electromagnetic coupling between adjacent scale-levels is introduced and it has been shown that the computation of these SCNs is mutually independent. This formulation, by its very nature is highly parallelizable, which gives SCT a huge advantage over other techniques that have to be adapted for distributed processing.

In the second half of this chapter the Scale-Changing Technique is applied to the case of a typical reflector unit cell under infinite array conditions. Radiation pattern results and the results for the phase-shift introduced to a linearly polarized plane-wave under both normal and oblique incidence are calculated and compared to another simulation tool. The good agreement between the results demonstrates that SCT is a reliable design and simulation technique.

He who angers you, conquers you.
Elizabeth Kenny

6

Electromagnetic Modeling of Finite-Size Large Microstrip Reflectarrays by Scale Changing Technique

6.1. Introduction

In the previous chapter we have detailed the underlying theory and working of scale-changing technique with the example of a microstrip phase shifter cell under infinite array conditions. In this chapter we will see how this technique can be used to efficiently model large finite-sized reflectarrays of uniform and non-uniform geometry.

First of all we will introduce the concept of bifurcation multipole which is essentially a scale-changing network (SCN) to model the electromagnetic coupling between neighboring unit cells at same scale level in a reflectarray. Mutual coupling between two planar dipoles will be characterized with the help of this scale-changing network and it will be demonstrated that in the case of a planar dipole array the mutual coupling effect is accurately taken into account when modeled using SCT.

Later in the chapter, the concept of this bifurcation scale-changing network is enhanced to incorporate the mutual coupling in 2D microstrip reflectarrays. Large uniform and non-uniform passive planar reflectarray structures are analyzed for plane-wave scattering problem and a good agreement is obtained with the simulation results of conventional simulation tools. Later two types of free-standing planar structures are analyzed using pyramidal horn as an excitation source. Results are presented when the horn is placed at an

offset with an angle of incidence. Also at the end in Section 6.5 the SCT modeling and simulation of a small (containing four phase shifter elements) active reflectarray (electronically tunable with RF-MEMS switches) is presented. The modeling of this small array is presented as an initial step towards large reconfigurable reflectarrays . At the end, the comparison of simulation times between SCT and other full-wave simulation techniques is given.

6.2. Modeling of Inter-Cellular Coupling

6.2.1. Bifurcation Scale-Changing Network

Consider a small array of two unit-cells placed side by side horizontally as shown in Figure 6.1(a). Each of the unit-cells can be characterized independently by its *surface-impedance matrix* defined using an ortho-normal modal-basis of unit-cell's domain. To model the overall behavior of this simple two-cell array, mutual electromagnetic interactions between the cells have to be taken into account. These mutual interactions are characterized by a scale-changing network which when cascaded with the surface impedance matrices of individual unit-cells will give the overall surface impedance or admittance that characterizes this 2-cell array.

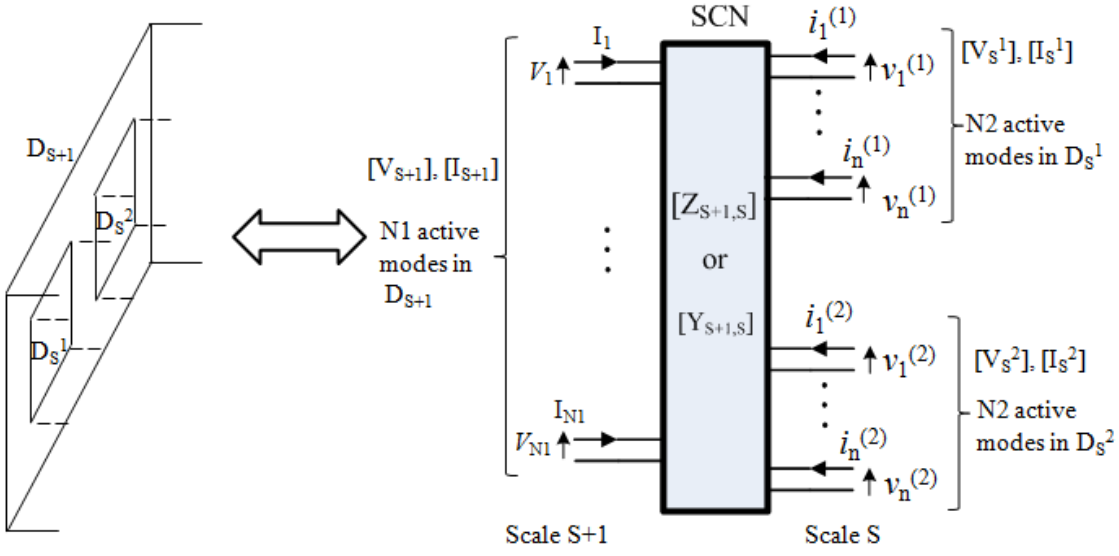

(a) (b)

Figure 6.1: (a) Electromagnetic coupling between two adjacent unit-cell domains D_S^1 and D_S^2 modeled by a bifurcated waveguide. (b) Inter-modal coupling between parent domain D_{S+1} and daughter domains D_S^1 and D_S^2 can be represented by a bifurcation scale-changing network (SCN).

The parent-domain D_{S+1} at scale level S+1 along with the sub-domains D_S^1 and D_S^2 (unit-cell domains) at lower scale level S can be visualized as the openings of a bifurcated waveguide as given in Figure 6.1 (a), the scale-changing network of this bifurcated waveguide (Figure 6.1(b)) is therefore dubbed as the *bifurcation multipole*.

6.2.1.1. Equivalent Electromagnetic Circuit Diagram

Keeping in view the SCT theory of chapter 4, the equivalent circuit to compute the bifurcation scale-changing network between a generic scale S+1 and its subsequent scale S is represented in Figure 6.2. In this equivalent circuit, the electromagnetic sources forming the two branches of the circuit model are the transverse fields in the two sub-domains lying at scale S. The source part of the circuit represents the excitation fields at scale level S+1 [44].

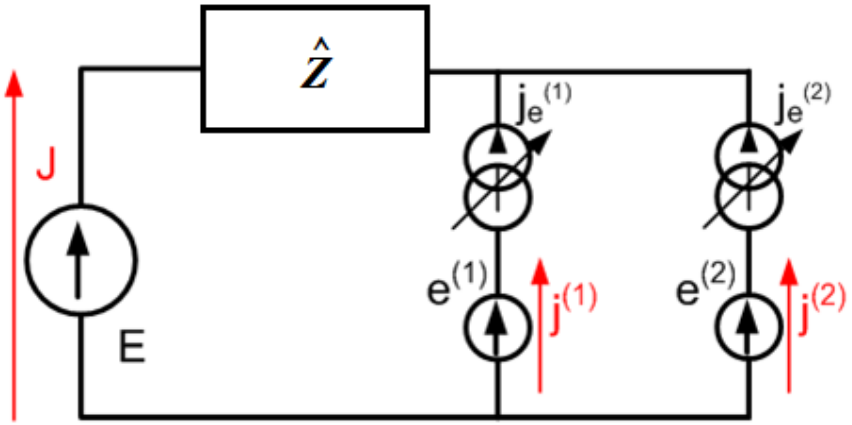

Figure 6.2: Equivalent circuit diagram of a bifurcation scale-changing network. The dual quantities are shown in red.

The current sources $j_e^{(1)}$ and $j_e^{(2)}$ are the virtual-sources defined in the aperture domains D_S^1 and D_S^2 to model the perfect dielectric boundary conditions where the electric field scale-changing sources $e^{(1)}$ and $e^{(2)}$ on the other hand represent the tangential electromagnetic fields in the aperture domains. The tangential electromagnetic field in the parent domain D_{S+1} (at scale S+1) is represented by the source **E**. Virtual sources and the scale-changing sources when defined in the same domain and using the same modal-basis can be modeled by a single equivalent source [68]. This simplification reduces the analytical calculations of the circuit. A simplified version of the equivalent circuit is thus shown in Figure 6.3 with the new equivalent current sources $j^{(1)}$ and $j^{(2)}$.

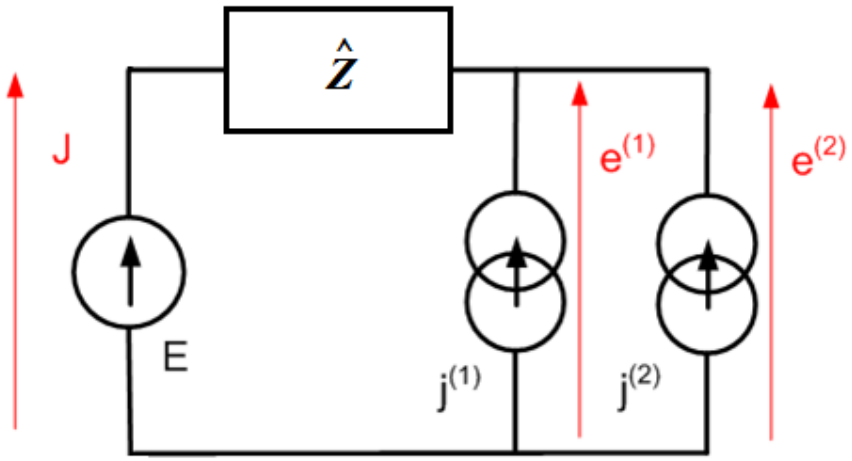

Figure 6.3: Simplified Equivalent circuit. Virtual source and the scale-changing source of each branch (when defined in the same domain and using same orthogonal modal-basis) can be replaced by a single current source.

Assuming N_1 active modes in D_{S+1} and N_2 in each of the daughter domains (D_S^1, D_S^2) we can express the electromagnetic field quantities in terms of mathematical equations written using the equivalent circuit of Figure 6.3.

$$\begin{cases} \vec{E} = \sum_{n=1}^{N1} V_n \vec{F}_n \\ \vec{J} = \sum_{n=1}^{\infty} I_n \vec{F}_n \end{cases} \tag{6.1}$$

$\vec{F}_n$ is the orthogonal modal-basis defined in D_{S+1}.

Similarly,

$$\hat{Z} = \sum_{n=N1+1}^{\infty} |\vec{F}_n\rangle Z_n \langle\vec{F}_n| \tag{6.2}$$

Where Z_n is the equivalent parallel modal impedance in the two half-regions; for example, if we have two different substrates at the two sides of the discontinuity plane, assuming air on one side and a dielectric with relative permittivity ε_r on the other, modal impedance of the n^{th} passive mode Z_n is the parallel equivalent of modal impedances of that mode in each of the dielectric domain and is written as:

$$Z_n = \frac{Z_n^{\varepsilon_0}\, Z_n^{\varepsilon_r}}{Z_n^{\varepsilon_0} + Z_n^{\varepsilon_r}} \tag{6.3}$$

The expressions $[\mathrm{I_{S+1}}]$ and $[\mathrm{V_{S+1}}]$ shown in Figure 6.1 are the column vectors of size N_1 containing the coefficients I_n and V_n of equation 6.1 as follows:

$$[\mathrm{I_{S+1}}] = \begin{bmatrix} \mathrm{I_1} \\ \vdots \\ \mathrm{I_{N1}} \end{bmatrix} \qquad [\mathrm{V_{S+1}}] = \begin{bmatrix} \mathrm{V_1} \\ \vdots \\ \mathrm{V_{N1}} \end{bmatrix} \tag{6.4}$$

Considering the modal-basis $\boldsymbol{f_n^{(1)}}$ and $\boldsymbol{f_n^{(2)}}$ in the two sub-domains D_S^1 and D_S^2, the tangential fields in them can be expressed on their respective modal-basis. For sub-domain D_S^1:

$$\begin{cases} \overrightarrow{\boldsymbol{J^{(1)}}} = \sum_{n=1}^{\infty} i_n^{(1)}\, \overrightarrow{\boldsymbol{f_n^{(1)}}} \\ \overrightarrow{\boldsymbol{e^{(1)}}} = \sum_{n=1}^{\infty} v_n^{(1)}\, \overrightarrow{\boldsymbol{f_n^{(1)}}} \end{cases} \tag{6.5}$$

similarly for sub-domain D_S^2,

$$\begin{cases} \overrightarrow{\boldsymbol{J^{(2)}}} = \sum_{n=1}^{\infty} i_n^{(2)}\, \overrightarrow{\boldsymbol{f_n^{(2)}}} \\ \overrightarrow{\boldsymbol{e^{(2)}}} = \sum_{n=1}^{\infty} v_n^{(2)}\, \overrightarrow{\boldsymbol{f_n^{(2)}}} \end{cases} \tag{6.6}$$

The coefficient vectors $i_n^{(1)}, v_n^{(1)}, i_n^{(2)} and\ v_n^{(2)}$ of equations (6.5) and (6.6) are defined on the active-modes in each sub-domain.

$$\left[I_S^{(k)}\right] = \begin{bmatrix} i_1^{(k)} \\ \vdots \\ i_{N2}^{(k)} \end{bmatrix} \qquad \left[V_S^{(k)}\right] = \begin{bmatrix} v_1^{(k)} \\ \vdots \\ v_{N2}^{(k)} \end{bmatrix} \quad \forall\ k = 1,2 \tag{6.7}$$

6.2.1.2. Matrix Notation

In order to compute the multipole-matrix that characterizes the bifurcation multipole Figure 6.1(b), we need to find a relation between the quantities defined in the parent domain D_{S+1} to that defined in the sub-domains D_S^1 and D_S^2. As these quantities are defined on the active-modes of their respective modal-basis, they form the ports through which tangential fields at one scale can interact with the tangential fields of the other. The relation between the fields at two scales can be written from the equivalent circuit of Figure 6.3 using Kirchoff laws.

$$\begin{bmatrix} J \\ e^{(1)} \\ e^{(2)} \end{bmatrix} = \begin{bmatrix} 0 & -1 & -1 \\ 1 & \hat{Z} & \hat{Z} \\ 1 & \hat{Z} & \hat{Z} \end{bmatrix} \times \begin{bmatrix} E \\ j^{(1)} \\ j^{(2)} \end{bmatrix} \tag{6.8}$$

Solving the matrix equation of equation (6.8) by applying Galerkin method gives the following:

$$\begin{bmatrix} [I_{S+1}] \\ \left[V_S^{(1)}\right] \\ \left[V_S^{(1)}\right] \end{bmatrix} = \begin{bmatrix} 0 & -P_1^{(1)} & -P_1^{(2)} \\ P_1^{(1)*} & P_2^{(1)*} Z P_2^{(1)} & P_2^{(1)*} Z P_2^{(2)} \\ P_1^{(2)*} & P_2^{(2)*} Z P_2^{(1)} & P_2^{(2)*} Z P_2^{(2)} \end{bmatrix} \times \begin{bmatrix} [V_{S+1}] \\ \left[I_S^{(1)}\right] \\ \left[I_S^{(2)}\right] \end{bmatrix} \tag{6.9}$$

Where the symbol $*$ denotes the complex conjugate transpose. If M denotes the multipole-matrix that characterizes the bifurcation-multipole that relates the tangential fields at scale S+1 and S defined on the active modes, then equation (6.9) can be rewritten as under:

$$\begin{bmatrix} [I_{S+1}] \\ \left[V_S^{(1)}\right] \\ \left[V_S^{(2)}\right] \end{bmatrix} = [M] \times \begin{bmatrix} [V_{S+1}] \\ \left[I_S^{(1)}\right] \\ \left[I_S^{(2)}\right] \end{bmatrix} \tag{6.10}$$

The constituent sub-matrices of M are defined here; $\left[P_1^{(k)}\right]$ is the projection matrix of dimensions $N_1 \times N_2$ of active modes of modal-basis $\vec{\boldsymbol{F}}_{\boldsymbol{n}}$ on $\vec{\boldsymbol{f}}_{\boldsymbol{n}}^{(k)}$;

$$\left[P_1^{(k)}\right] = \begin{bmatrix} \langle F_1, f_1^{(k)} \rangle & \cdots & \langle F_1, f_{N2}^{(k)} \rangle \\ \vdots & \ddots & \vdots \\ \langle F_{N1}, f_1^{(k)} \rangle & \cdots & \langle F_{N1}, f_{N2}^{(k)} \rangle \end{bmatrix} \quad \forall\, k = 1,2 \tag{6.11}$$

Similarly $\left[P_2^{(k)}\right]$ is the projection matrix of dimensions $(\mathrm{M} - \mathrm{N1}) \times \mathrm{N2}$ of passive modes of modal-basis $\vec{\boldsymbol{F}}_{\boldsymbol{n}}$ on $\vec{\boldsymbol{f}}_{\boldsymbol{n}}^{(k)}$.

$$\left[P_2^{(k)}\right] = \begin{bmatrix} \langle F_{N1+1}, f_1^{(k)} \rangle & \cdots & \langle F_{N1+1}, f_{N2}^{(k)} \rangle \\ \vdots & \ddots & \vdots \\ \langle F_M, f_1^{(k)} \rangle & \cdots & \langle F_M, f_{N2}^{(k)} \rangle \end{bmatrix} \quad \forall\, k = 1,2 \tag{6.12}$$

The bifurcation multipole defined by the matrix [M] characterizes the electromagnetic coupling between the two consecutive scale-levels and serves as a basic block to model the mutual coupling between the elements of an array structure.

6.2.2. Single Mode Example

To clarify the idea of EM coupling by active modes, let us apply a special case on Figure 6.1, in this case we take only single transverse electromagnetic (TEM) mode used as an active mode in D_{S+1}, D_S^1 and D_S^2 while all the other modes are evanescent (i.e., their cut-off frequency in these three domains is higher than the operating frequency). Additionally consider that the domains D_S^1 and D_S^2 are loaded with metallic strips printed on perfectly magnetic surface, all these domains are bounded by electric (along x-axis) and magnetic (along y-axis) walls as shown in Figure 6.4 (a) and (b).

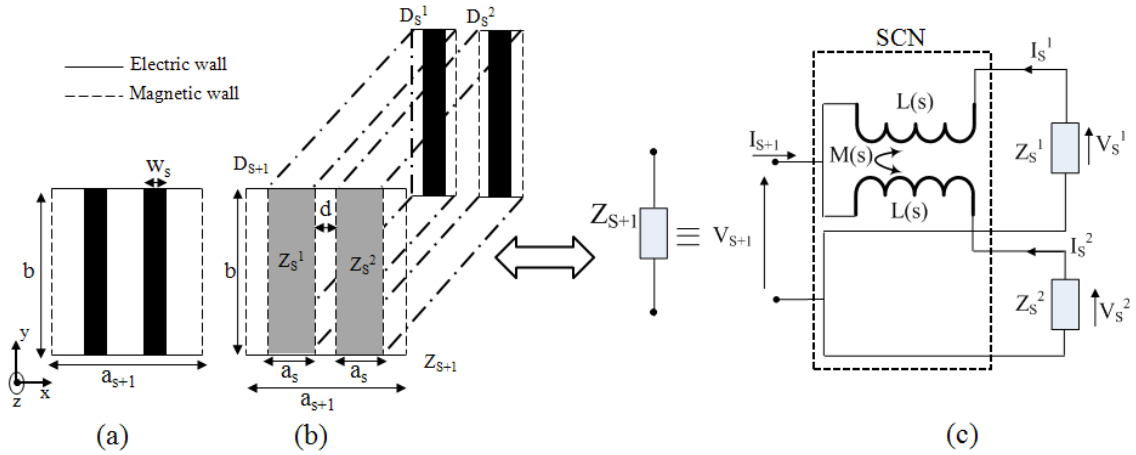

Figure 6.4: (a) a lossless discontinuity plane D_{S+1} (scale-level S+1) containing two metallic strips of width w_S printed on perfectly magnetic surface. (b) Two rectangular sub-domains D_S^1 and D_S^2 (scale-level$S$) of width a_S and height b are defined in the discontinuity plane D_{S+1}. (c) Its equivalent electrical circuit when only TEM mode is used as an active mode in D_{S+1}, D_S^1 and D_S^2 while all the other modes are passive. In this special illustrative case it can be seen that a simple mutual inductance models the EM coupling between the scale-levels S and S+1. The TEM surface impedance $Z_{S+1} = V_{S+1}/I_{S+1}$ in D_{s+1} is then derived from the calculation of the input impedance of the SCN loaded by Z_s^1 and Z_s^2.

The SCN that models the EM coupling between the TEM-modes in D_{S+1}, D_S^1 and D_S^2 is shown in Figure 6.4(c) enclosed by a dashed rectangle. This SCN is characterized by a multipole matrix $M_{s+1,s}$ as defined by the following matrix equation:

$$\begin{bmatrix} I_{S+1} \\ V_S^1 \\ V_S^2 \end{bmatrix} = \left[M_{S+1,S}\right] \begin{bmatrix} V_{S+1} \\ I_S^1 \\ I_S^2 \end{bmatrix} \tag{6.13}$$

Where

$$[M_{s+1,s}] = \begin{bmatrix} 0 & -1 & -1 \\ 1 & jL(s)\omega & jM(s)\omega \\ 1 & jM(s)\omega & jL(s)\omega \end{bmatrix} \tag{6.14}$$

The analytical expressions for the self inductance *L(s)* and mutual inductance *M(s)* are given by:

$$L(s) = 2\mu_0 \frac{b}{a_{s+1}} \sum_{m=1,2,3,\ldots}^{\infty} \frac{I_m^2}{\sqrt{\left(m\frac{\pi}{a_{s+1}}\right)^2 - {k_0}^2}} \tag{6.15}$$

and

$$M(s) = 2\mu_0 \frac{b}{a_{s+1}} \sum_{m=1,2,3,\ldots}^{\infty} \frac{(-1)^m I_m^2}{\sqrt{\left(m\frac{\pi}{a_{s+1}}\right)^2 - {k_0}^2}} \tag{6.16}$$

where

$$I_m = \frac{1}{a_s} \int_{-a_s+(a_{s+1}-d)/2}^{(a_{s+1}-d)/2} cos\left(m\frac{\pi}{a_{s+1}}x\right)\, dx = \frac{sin[m\pi(a_{s+1}-d)/2a_{s+1}] - sin\{m\pi[-a_s+(a_{s+1}-d)/2a_{s+1}]\}}{m\pi\frac{a_s}{a_{s+1}}} \tag{6.17}$$

The TEM surface impedances $\mathrm{Z_S^1} = -\mathrm{V_S^1}/\mathrm{I_S^1}$ and $\mathrm{Z_S^2} = -\mathrm{V_S^2}/\mathrm{I_S^2} (= \mathrm{Z_S^1}$ in this example) model the metallic strips in the sub-domains D_S^1 and D_S^2 respectively. The resulting TEM surface impedance $Z_{S+1} = V_{S+1}/I_{S+1}$ in D_{s+1} is then derived from the calculation of the input impedance of the SCN loaded by Z_S^1 and Z_S^2. The analytical expressions of Z_{S+1}, Z_S^1 and Z_S^2 are given by [70]:

$$Z_S = j\omega L_S \qquad \text{with} \qquad L_S = 2\mu_0 \frac{b}{a_s} \sum_{m=1,2,3,\ldots}^{\infty} \frac{1}{\sqrt{\left(2m\frac{\pi}{a_s}\right)^2 - {k_0}^2}} \left[\frac{sin\left(m\pi\frac{w_s}{a_s}\right)}{m\pi\frac{w_s}{a_s}}\right]^2 \tag{6.18}$$

Finally the surface impedance Z_{S+1} in D_{s+1} is then derived from the calculation of the input impedance of the SCN loaded by Z_s^1 and Z_s^2 $(= Z_s^1 = Z_s)$ as follows:

$$Z_{S+1} = j\omega L_{S+1} \qquad \text{with} \qquad L_{S+1} = \frac{1}{2}[L_S + L(S) + M(S)] \tag{6.19}$$

In this illustrative example, the electromagnetic coupling between D_S^1 and D_S^2 is clearly modeled by the mutual inductance *M(s)*. In practice, a single active mode per scale-level is not sufficient for obtaining accurate results and describing precisely the EM coupling between the scales rather, as previously mentioned, the number of active modes at each scale level is derived from the numerical convergence analysis of the solution. However this illustrative example allows providing a comprehensive model representing the EM coupling by a simple mutual inductance *M(S)* between two adjacent (successive) scale-levels *S* and S+1.

6.2.3. Full Wave Analysis for Coupling Validation

6.2.3.1. Coupling Analysis between two Dipoles

Now to validate that the bifurcation multipole described in last Section accurately models the mutual coupling between the elements of the array, full wave simulation results are presented here. Two thin metallic strips of half-wavelength (12 mm) dimensions separated by a distance d as shown in Figure 6.5 are simulated as a simple array of two unit-cells. Given a plane wave with normal incidence, an isolated half-wave dipole scatters uniformly around its axis.

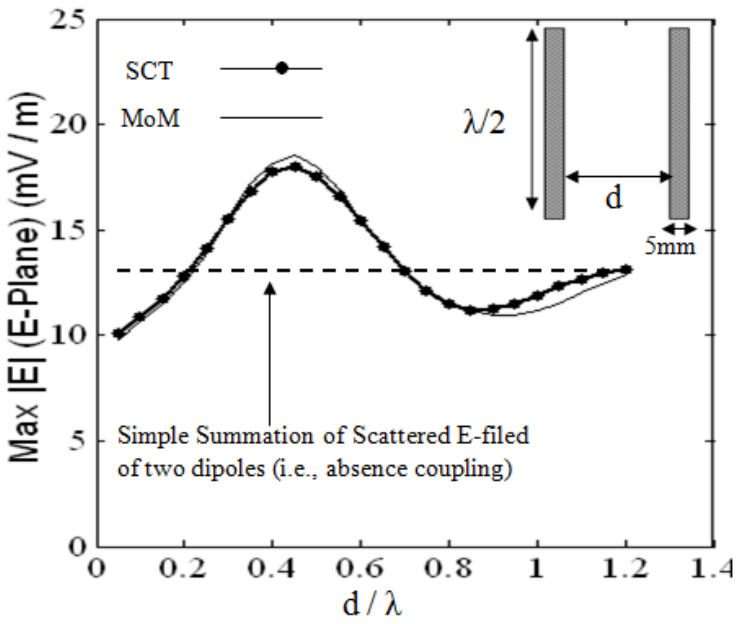

Figure 6.5: Characterization of mutual coupling for two dipole strips at 12.5GHz: E-plane backscattered electric field in the normal direction by two coupled half-wave printed dipoles with respect to the normalized separation between the dipoles when illuminating by a normally incident plane wave (polarized along the dipoles axis) at 12.5GHz.

In the absence of mutual coupling, the resulting re-radiated E-field in the normal direction is a simple summation of the individual fields radiated by each dipole as given by superposition principle. This value is indicated by the straight dotted line on the plot of Figure 6.5. However, due to the presence of mutual coupling between the two dipoles which may generate a constructive or destructive interference effect, the actual backscattered field in the normal direction depends on the distance d between the two dipoles. A single scale-changing network grouping the elements in one dimension is required to characterize the mutual coupling between the two strips.

The strips were simulated multiple times by varying the distance between them. The maximum radiated E-field values are plotted against the distance d normalized to the free-space wavelength λ. The results of the simulations performed by a conventional simulation tool HFSS (Ansoft high frequency structure simulator based on FEM and MoM) are also given for validation purposes. It is found that the results obtained by two techniques agree closely which validates the point that SCT accurately characterizes the effects of mutual coupling between the elements of an array. Here in this case, at lower level 25 active modes

are taken for each subdomain while at the top level 40 active modes and 2000 passive modes have been taken for ensuring the convergence of the numerical solution.

6.2.3.2. Coupling Analysis for a 4×4 Dipole-array.

For modeling the mutual coupling effect in case of a small two-dimensional array, a small 4×4 array of dipole strips has been simulated under normal plane-wave incidence. The dipole elements are separated horizontally by a distance of half wavelength. In this case the scale-changing network groups elements in two dimensions, i.e., mutual coupling between four elements is considered in the computation of a single scale-changing network. To account properly for all mutual EM coupling effects, a convergence study has to be done to ensure that enough active modes are considered in the calculation of scale-changing networks.

The inter-cell interactions are not well defined by too few modes while too many can produce ill-conditioned matrices and other numerical errors. The plots of the radiation patterns in H-plane and E-plane of the array are represented in Figure 6.6(a) and (b) respectively, for the normal plane-wave incidence with the incident E-field polarized along the axis of the dipole strips. The radiation pattern of the array in the absence of mutual coupling as computed using the radiation pattern of a single element and the array factor of the 4×4-dipole array is also traced on the same plot for showing that mutual coupling occurs in the considered planar array. The same array was simulated by HFSS for comparison purposes. Here in this case, at the top level, 300 active modes and 3000 passive modes have been used.

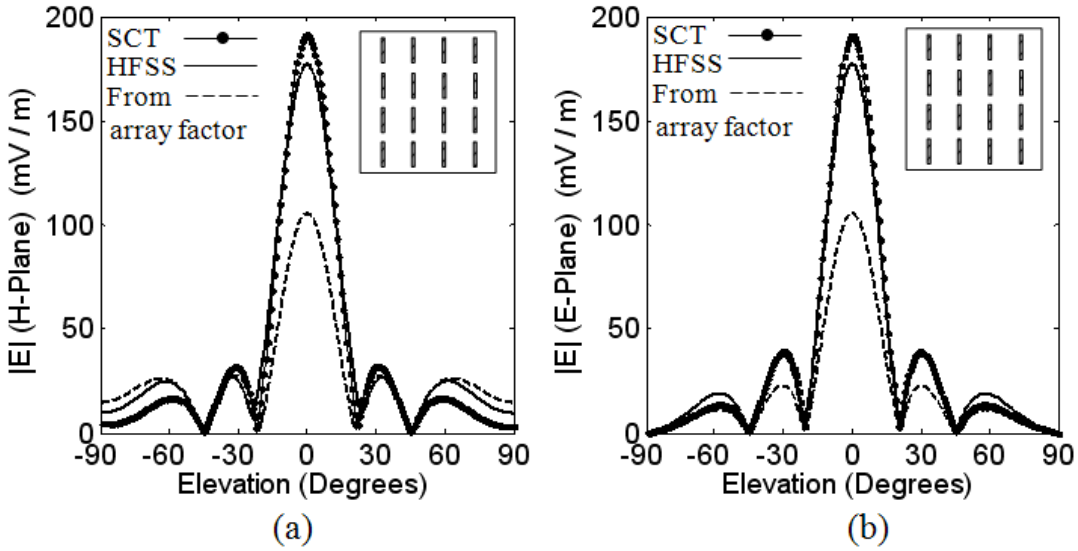

Figure 6.6: Far-field radiation pattern of a simple 4×4 dipole array in(a) H-plane and (b) E-plane when illuminating by a normally incident plane wave (polarized along the dipoles axis) at 12.5GHz.

6.3. Modeling of large and more Complex Microstrip Reflectarrays

Once it has been shown in previous Sections that SCT successfully characterizes mutual EM coupling between the elements of a small and simple finite array of dipoles, the next logical step is to apply the concept for the case of larger arrays and with relatively complex geometries that are traditionally used in modern reflectarray applications. In this Section, we will first present the theory behind the scattering problem and then the radiation pattern results for three types of reflectarrays are presented.

6.3.1. SCT Formulation of Electromagnetic Scattering Problem

This section presents the theory of electromagnetic scattering from the planar reflectarray shown in Figure 6.7 (a). Let say it consists of $N\times N$ unit cells composed of metallic patterns printed on a grounded dielectric surface of thickness h and relative permittivity ε_r. Suppose that in the discontinuity plane D many scale levels (with respect to small and large dimensions) separate the largest pattern to the smallest one. The discontinuity plane D is illuminated by a plane wave $\vec{E}_{inc}$ with an arbitrary angle of incidence (θ, φ) on one side,

while on the other side a finite-sized grounded dielectric surface is placed. The time-harmonic regime is assumed for all fields.

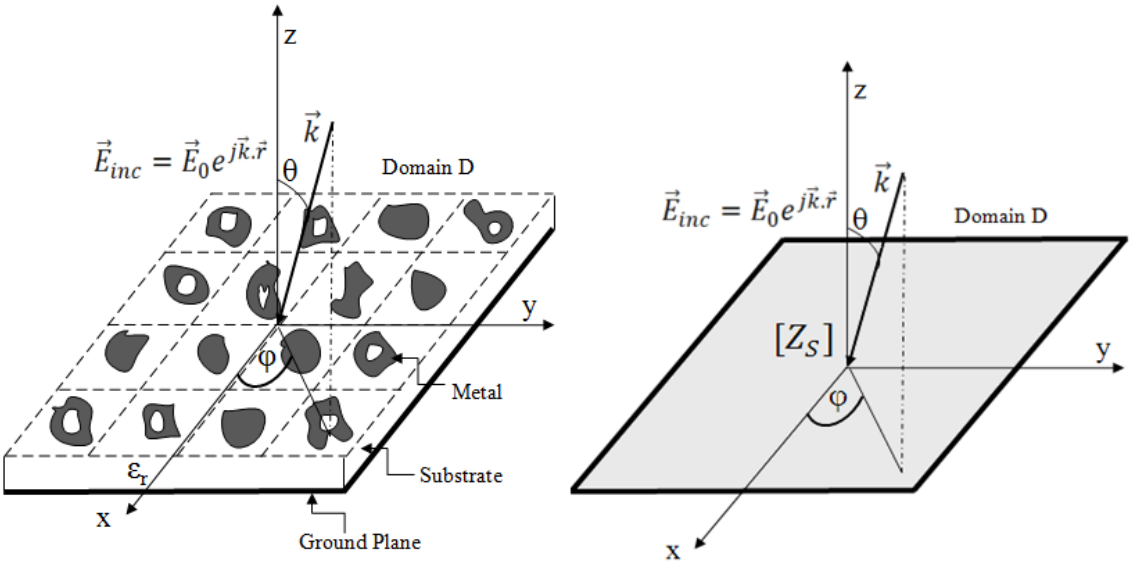

(a) (b)

Figure 6.7: (a) An $N \times N$ microstrip reflectarray of arbitrary cells under arbitrary plane wave incidence. (b) The surface impedance matrix $[\boldsymbol{Z_S}]$ modeling the domain $\boldsymbol{D}$, this matrix is derived from the cascade of scale changing networks as shown in Figure 6.9.

6.3.1.1. Derivation of the current density on the reflectarray domain D

The integral equation formulation of the boundary value problem on the metal domain $\boldsymbol{D_{metal}}$ (metallic parts on the Domain D) can be written as [33]:

$$\vec{E}_{exc}(r) + \vec{E}_{scat}(r) = \vec{E}_{tot}(r) = 0 \quad for \quad r \in D_{metal} \tag{6.20}$$

Where $\vec{E}_{exc} = \vec{E}_{inc}(1 + \Gamma)$, $\vec{E}_{inc}(r)$ and $\vec{E}_{scat}(r)$ denote the incident and scattered fields respectively and Γ is the reflected coefficient computed by the SCT when the domain is replaced by a perfect electric conductor. The total tangential field is zero as dictated by the perfect electric boundary conditions at the metal surface D_{metal}. The scattered field from a planar surface can be written in terms of unknown surface current density $\vec{J}$ on the metal domain D_{metal} of the planar scatterer and free space dyadic Green function $\bar{\bar{G}}(r, r')$:

$$\vec{E}_{scat}(r) = \int_{D_{metal}} \bar{\bar{G}}(r,r')\vec{J}(r')dr' \tag{6.21}$$

In Scale Changing Technique, the current density $\vec{J}$ defined on the metal domain D_{metal} is replaced by an equivalent current density $\vec{J}_{eq}$ defined on the entire discontinuity plane D incorporating D_{metal}. This domain D is characterized by surface impedance matrix $[Z_s]$ **(**the calculation details of $[Z_s]$ is given in the following section) which allows formulating the new boundary conditions of the problem such as:

$$\bar{\bar{G}}\,\vec{J}_{eq} - \vec{E}_{exc}(r) = \vec{E}_{tot} = -[Z_s]\,\vec{J}_{eq} \tag{6.22}$$

Where $\vec{E}_{tot}$ is the vector of total tangential field (superposition of scattered and incident field). The unknown surface current density J_{eq} is given by:

$$\vec{J}_{eq} = \sum_{i=1}^{N_D \times N_D} \vec{I}_{eq\_i}\vec{g}_i \tag{6.23}$$

where $\vec{g}_i$ is the ith entire domain trial function, here these functions are the active modes in domain D and N_D represents the number of active modes deduced from comprehensive numerical convergence study of the EM scattering problem. In practice, same entire-domain orthogonal basis functions are also used for representing the equivalent surface impedance matrix $[Z_s]$ that models the reflectarray. By applying Galerkin method equation (6.23) can be written as:

$$[Z_{space}][I_{eq}] - [V_{exc}] = [V_{tot}] = -[Z_s][I_{eq}] \tag{6.24}$$

Where $[Z_{space}]$ is the matrix representation of the free-space dyadic Green function and $[I_{eq}]$ denotes the vector matrix containing the unknown expansion coefficients of the surface current density in domain D. Following the formulation of [33] the vector $[V_{exc}]$ is given by:

$$[V_{exc}] = \{[1] + [\Gamma]\}[V_{inc}] \tag{6.25}$$

Where $[V_{inc}]$ contains known expansion coefficients of the incident electric field $\vec{E}_{inc}$ on the active modes in D, the matrix '[1]' is the unit matrix with dimension $N_D \times N_D$ and $[\Gamma]$ denotes the reflection matrix representation in the set of active modes when the domain *D* is replaced by a perfect electric conductor (the calculation details of $[V_{exc}]$, $[Z_{space}]$ and $[\Gamma]$ is given in the following sections). To determine the electric field scattered by the reflectarray when illuminating by a plane wave, the unknown components $[I_{eq}]$ of the equivalent surface current density in the domain *D* needs to be calculated. These components may be computed from equations (6.25) and (6.26) as follows:

$$[I_{eq}] = \{[Z_{space}] + [Z_s]\}^{-1}\{[1] + [\Gamma]\}[V_{inc}] \tag{6.26}$$

From the computation of $[I_{eq}]$, the total electric field $[V_{tot}] = -[Z_s][I_{eq}]$ is then derived. Finally, the scattered electric relevant to the far field distribution is only $[V_{scat}]$ and is given by the following equation:

$$[V_{scat}] = [V_{tot}] - [V_{inc}] \quad or \quad \vec{E}_{scat} = \vec{E}_{tot} - \vec{E}_{exc} \tag{6.27}$$

The process of computing the values of V_{inc}, Z_s and Z_{space} in equation (6.26) is detailed below.

6.3.1.2. Calculation of $[V_{inc}]$

The vector $[V_{inc}]$ contains the expansion coefficients of the incident electric-field in the set of N_D active modes $(\vec{F}_m)_{m=1,2,\ldots,N_D}$ in the domain D of the array. The mth coefficient $[V_{inc}]_m$ is computed as follows:

$$[V_{inc}]_m = \langle F_m, E_{inc} \rangle = \iint_D \vec{F}_m^*(x,y).\vec{E}_{inc}(x,y)dxdy \tag{6.28}$$

where $\vec{E}_{inc}(x,y)$ is the tangential component of the incident field on the planar domain D. In the case of plane-wave incidence it can be written as:

$$\vec{E}_{inc}(x,y) = \left[E_{0x}\vec{x} + E_{0y}\vec{y}\right] e^{-j(k_0\, sin\theta cos\varphi\, x + k_0\, sin\theta sin\varphi\, y)} \tag{6.29}$$

with θ and φ the angles of incidence (see Figure 6.7).

Instead of plane wave excitation for antenna sources such as feed horn, $\vec{E}_{inc}$ is also the tangential component of the radiated electric-field incident on the planar surface D and can be calculated from the radiation pattern characteristics and the position of the source with respect to the reflectarray. This process is outlined in Appendix B for a case of pyramidal horn. In addition $\vec{E}_{inc}$ can be found numerically by simulating the source antenna with any 3D EM simulation tool (e.g. GRASP) and using the tangential component of the field projected on the reflectarray-plane in equation to find V_{inc}. Alternatively the projection of antenna measurement data expressed on spherical modes can be used in place of $\vec{E}_{inc}$.

6.3.1.3. Calculation of $\left[Z_{space}\right]$

The matrix $\left[Z_{space}\right]$ in equation (6.26) is represented as the set of N_D active modes $\left(\vec{F}_m\right)_{m=1,2,\ldots,N_D}$ in the domain D of the array. The element $\left[Z_{space}\right]_{mn}$ $\forall$ $m,n = 1,2,\ldots,N_D$ is given as follows.

$$\left[Z_{space}\right]_{mn} =$$

$$\iint_{-\infty}^{+\infty} \vec{F}_m^*(x,y) \cdot \frac{j}{\omega\varepsilon_0} \begin{bmatrix} k_0^2 + \frac{\partial^2}{\partial x^2} & \frac{\partial^2}{\partial x \partial y} \\ \frac{\partial^2}{\partial y \partial x} & k_0^2 + \frac{\partial^2}{\partial y^2} \end{bmatrix} \bar{\bar{G}}(x,y\,;x',y') \cdot \vec{F}_n(x',y') dx dy$$

(6.30)

where $\bar{\bar{G}}(x,y';x,y')$ is the dyadic Green function in the spatial domain and the convolution product in the integrand is given by.

$$\bar{\bar{G}}(x,y\,;x',y') \cdot \vec{F}_n(x',y') = \iint_{-\infty}^{+\infty} \frac{e^{-jk\left[(x-x')^2+(y-y')^2\right]^{1/2}}}{4\pi\left[(x-x')^2+(y-y')^2\right]^{1/2}}\, \vec{F}_n(x',y') dx' dy' \tag{6.31}$$

In the spectral domain the equation (6.30) reduces to the following expression:

$$[\mathrm{Z_{space}}]_{mn} = \frac{1}{4\pi^2}\iint_{-\infty}^{+\infty} \vec{\tilde{F}}_m^*(k_x,k_y).\ \frac{1}{j\omega\varepsilon_0}\begin{bmatrix} k_x^2-k_0^2 & k_xk_y \\ k_yk_x & k_y^2-k_0^2 \end{bmatrix} \bar{\bar{\tilde{G}}}\,(k_x,k_y)\vec{\tilde{F}}_n^*(k_x,k_y)dk_xdk_y \quad (6.32)$$

where $\vec{\tilde{F}}_n^*(k_x,k_y)$ denotes the Fourier transform of $\vec{F}_n(x',y')$ and $\bar{\bar{\tilde{G}}}\,(k_x,k_y)$ is given by:

$$\bar{\bar{\tilde{G}}}\,(k_x,k_y) = \begin{cases} \dfrac{-j}{\sqrt{k_0^2-k_x^2-k_y^2}} & if\ k_0^2 > k_x^2 + k_y^2 \\ \dfrac{1}{\sqrt{k_x^2+k_y^2-k_0^2}} & if\ k_0^2 < k_x^2 + k_y^2 \end{cases} \quad (6.33)$$

By using spectral domain the computation of $[Z_{space}]$ has been reduced to the computation of a single double integral in the spectral domain. Moreover since the test functions $\vec{F}(x',y')$ are defined in the rectangular domain their Fourier transform can be calculated analytically.

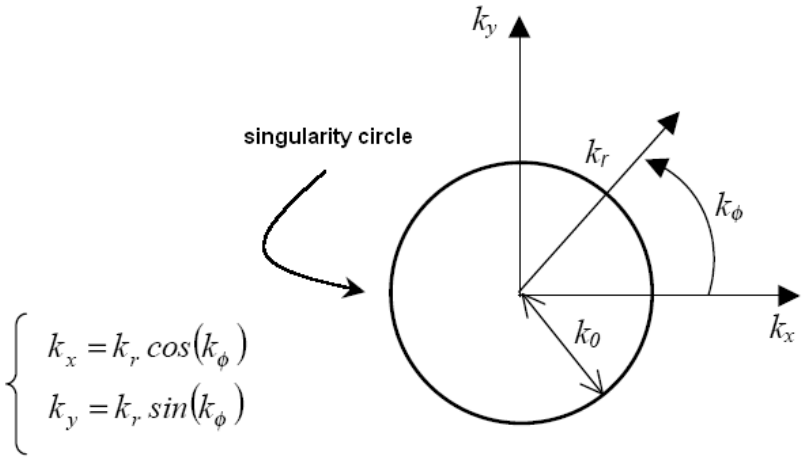

Figure 6.8: Wave-vector transformation from Cartesian to polar co-ordinates.

In the computation of the integral of equation (6.32) a singularity appears at $k_x^2 + k_y^2 = k_0^2$. While the continuous integral is computed numerically as a discrete sum, the discontinuity can easily be avoided. Using polar co-ordinates k_φ and k_r, singular values of k_x and k_y translates into a circle of $k_r = k_0$ as shown in the Figure 6.8. The numerical computation of the integral in equation 6.32 is performed in polar coordinates avoiding the singularity circle [44].

6.3.1.4. Calculation of $[\Gamma]$

In equation (6.25) the matrix [Γ] denotes the reflection matrix representation in the set of N_D active modes in *D* of the array when *D* is replaced by a perfect electric conductor. In this case the current density $[I_{eq}^{cc}]$ on *D* is given by $[I_{eq}^{cc}] = \left[Z_{space}\right]^{-1}[V_{inc}]$. Consequently [Γ] is such that $[E_r] = [\Gamma\,][E_{inc}]$ where $[E_r]=\left[Z_{space}\right][I_{eq}^{cc}]$. Finally $[V_{exc}]$ is derived from equation (6.25).

6.3.2. Derivation of the Surface Impedance Matrix $[Z_s]$

Here we will explain the SCT process to model the reflectarray of Figure 6.7(a) represented by domain D by its equivalent surface impedance $[Z_s]$ or admittance $[Y_s]$ as depicted in Figure 6.7(b). In a complex discontinuity surface the metallic patterns can be viewed as a set of several domains and embedded sub-domains. In order to demonstrate the partitioning process of the discontinuity plane in case of relatively large reflectarrays, consider the array of Figure 6.7(a) with individual cells of arbitrary geometry arranged on a uniform rectangular lattice.

As explained in the previous chapters, the starting point of the SCT approach consists of the coarse partitioning of the complex discontinuity plane into planar sub-domains of comparable sizes and arbitrary shapes; in each sub-domain a second partitioning is performed by introducing smaller sub-domains; again, in each sub-domain introduced at the previous step a third partitioning is performed by introducing smaller sub-domains; and so on. Such hierarchical domain-decomposition allows focusing rapidly on increasing fine details in the discontinuity plane. It is stopped when the finest dimension –the smallest scale– is reached. To each sub-domain, a scale-level is associated. The largest domain corresponds conventionally to the scale level $S = S_{max}$ while; the scale level $S = 1$ corresponds to the smallest domains.

For the sake of clarity, consider that the reflectarray of Figure 6.7(a) consists of 64 arbitrary unit cells (N=8). As shown in Figure 6.9, at scale level *S*, the plane of the array is partitioned into squared sub-domains $D_S^{i,j}$ of comparable sizes, where *i, j* denote the position indices of cell in the array. All the individual cells lie on the scale-level 1; at this scale, surface impedance $[Z_S]$ or admittance $[Y_S]$ matrix of each unit-cell is calculated individually.

Individual cells (or equivalently we can call them individual impedances or admittances) are then grouped into 4-cell blocks taking into account the mutual electromagnetic (EM)

coupling between the elements comprising the block. These 4-cell blocks make up the scale-level S=2.

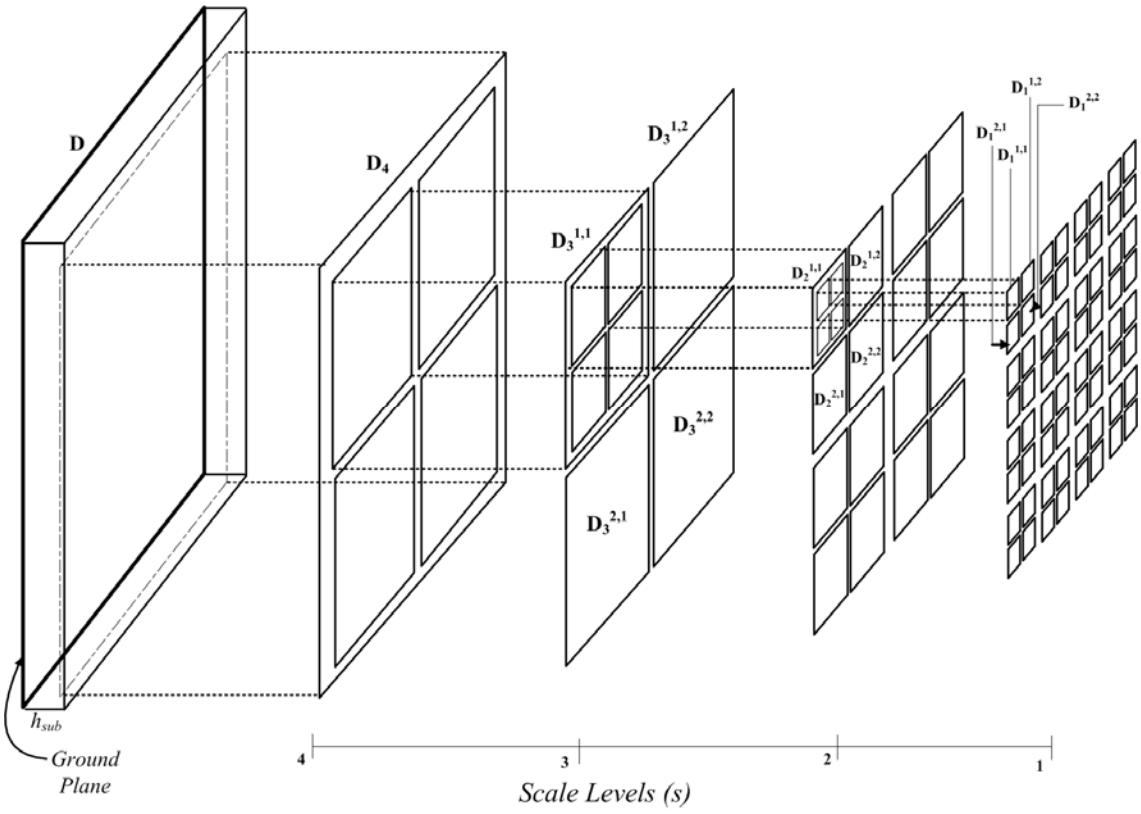

Figure 6.9: Partitioning of 64-cell array (8×8); such hierarchical domain-decomposition allows defining the constitutive scale-levels and focusing rapidly on increasing fine details in the array.

This process of grouping the block elements of the lower scale continues until the mutual EM coupling of the entire array has been modeled by reaching the highest scale level. The individual unit-cell at scale level S=1 representing by the sub-domain $D_1^{i,j}$ can be decomposed further into constitutive scale levels depending on the number of metallic patterns and fine details present in it. For illustration purpose, if we consider that the unit cell consists of a patch loaded with a slot then it can be decomposed into two or three scales as sketched in Figure 5.2 (Chapter 5). It should be noted that the effect of dielectric and ground plane is taken into account at each scale level.

This process of partitioning the array plane is applicable for the array of any size. Generally, in case of cells arranged on rectangular lattice, an array containing N number of cells can be partitioned in $log_2 N$ scale-levels. For other cell-arrangements the partitioning

technique is still valid, only the sub-domains may not be regular-shaped which would affect the choice of modal basis for the analysis of these domains.

By the partitioning process, the overall EM problem is divided into many sub-problems. To solve each problem separately, artificial boundary conditions are imposed at the contour of each sub-domain. These boundary conditions are applied only at the contours and are chosen such that they do not greatly perturb the electromagnetic fields in the domains. In each domain the tangential EM-fields are expanded on orthogonal modal-basis. Physical nature of the problem can be considered in the choice of boundary conditions. Or alternatively several boundary conditions can be tried and the one with the best convergence results are chosen. However, we have observed in practice that the choice between magnetic and electric boundary conditions at the contour of each sub-domain does not seem to be very critical for reaching the numerical convergence of the solutions.

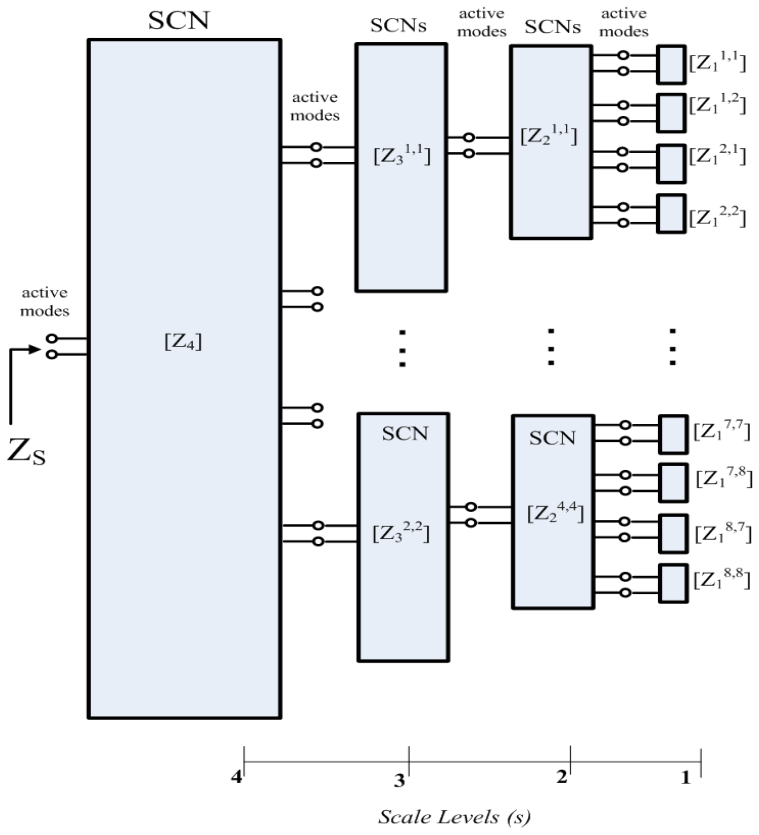

Figure 6.10: Computation of the surface impedance matrix of the reflectarray of Figure 6.9 obtained by the cascade of the scale changing networks derived at lower scale levels.

The last step in Scale Changing Technique is the cascading of all the scale changing networks to reach the global surface impedance or admittance of the whole reflectarray. The computation of all scale-changing networks is mutually independent therefore each multipole (SCN) can be computed separately on different machines and it is only the final step at which the resulting matrices are cascaded to obtain the global simulation of the entire structure. This cascading consequently, models the interactions among the multiple scales of a complex discontinuity plane where each network models the electromagnetic coupling between two adjacent (successive) scale levels S and S+1.

Now, referring to the partition process shown in Figure 6.10 of multiscale reflectarray of size 8×8, the equivalent surface impedance matrix of this reflectarray can be achieved by cascading all the scale changing networks derived at individual scale levels from S=1 to S=4 as shown in Figure 6.10. The term $Z_S^{i,j}$ (where S denotes the respective scale level of each sub-domain, i and j are position indices of the sub-domains inside the 8×8 rectangular reflectarray) represents the surface impedances of respective domains and sub-domains at their respective scale levels. The global surface impedance matrix $[Z_S]$ at the largest scale S=4 represents the equivalent multi-modal surface impedance of the whole reflectarray. Its dimension is the number of active modes required at largest scale S=4 for reaching the convergence of the numerical solution.

6.4. Numerical Results and Discussion

In this section the radiation pattern results for three types of reflectarrays are presented.

6.4.1. Microstrip Reflectarrays with Identical Unit Cells

Here, two types of uniform reflectarrays consisting of 256 and 64 identical elements arranged in 16×16 and 8×8 rectangular grids are considered. The geometries of the reflectarrays with all details of the unit cell are shown in Figure 6.11 (a)-(c). Each unit cell of 256-cell array consists of a simple metallic patch while in case of 64-cell array each cell contains a metallic patch loaded with a slot.

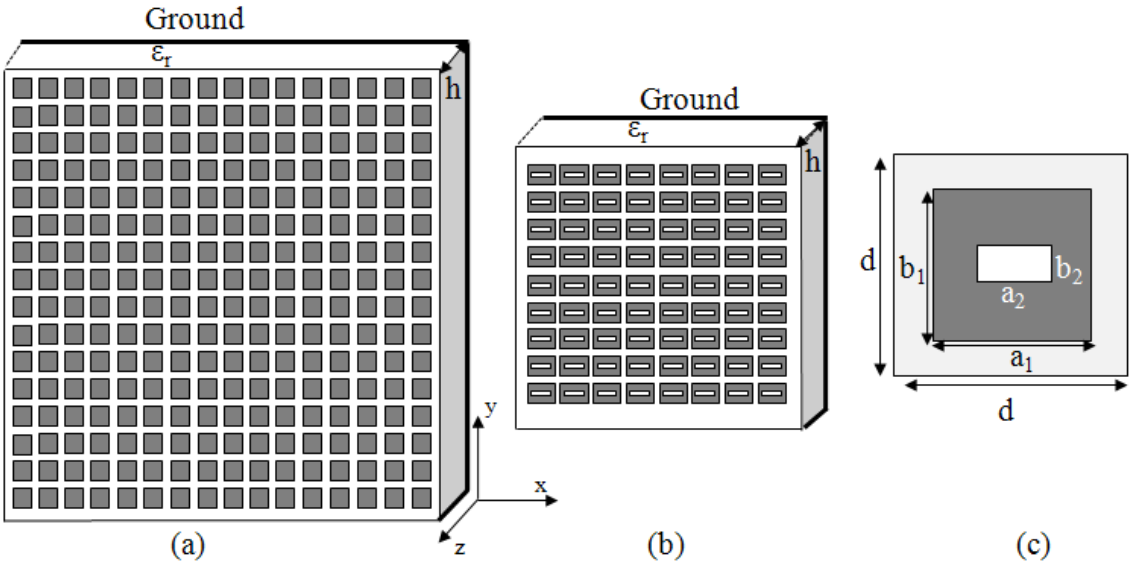

Figure 6.11: (a) A 256-cell (16 ×16) reflectarray geometry, unit cell and patch dimensions are the same as given in (c). (b) A 64-cell (8×8) reflectarray geometry with h=3.175mm, $\boldsymbol{\varepsilon_r}$=2.17. (c) An enlarged unit cell with d=16.8mm, a_1=13.5mm, b_1=13mm, a_2=9mm and b_2=6mm.

With an array of 256-cells, we need to compute eight scale-changing networks while in case of 64-cell array, 4 scale-changing networks are required. Also convergence study has to be done to find out a suitable number of coupling modes at each scale level, these steps have already been explained in detail in the light of scale changing technique. The radiation pattern results of the scattered E-field in E-plane and H-plane for normal incidence in case of 256-cell array are given in Figure 6.12.

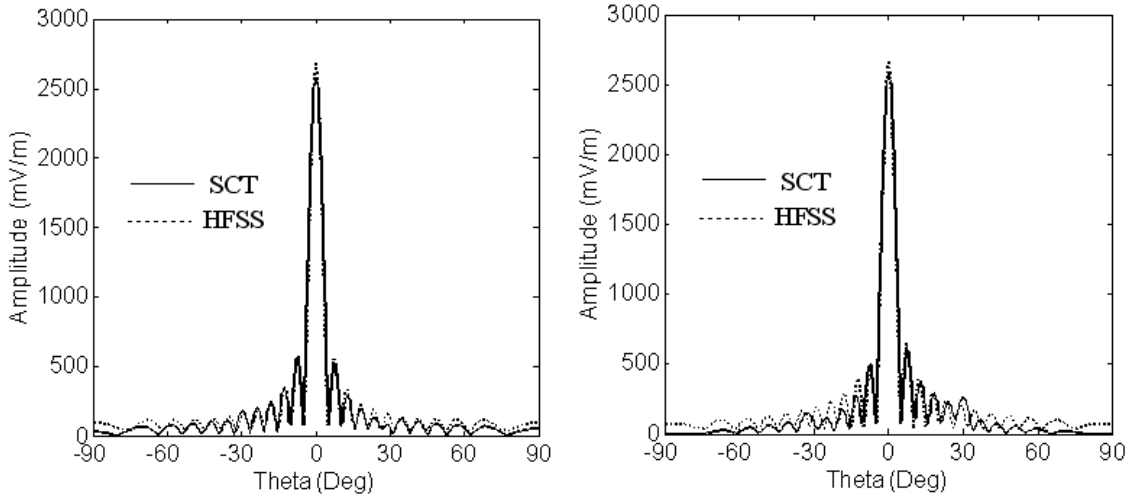

Figure 6.12: (a) E- plane and (b) H-plane radiation patterns of a 16×16 uniform patch-slot reflectarray (see caption of Figure 6.10(c) for the dimensions of the structure)

For the 64-cell array, both normal and oblique plane wave incidences are considered with the E-field polarized in the vertical direction. For this case, the radiation pattern results of the scattered E-field in E-plane and H-plane for normal and oblique (θ=10°) incidence cases are given in Figure 6.13. An excellent agreement is observed between the results obtained from scale changing technique and HFSS.

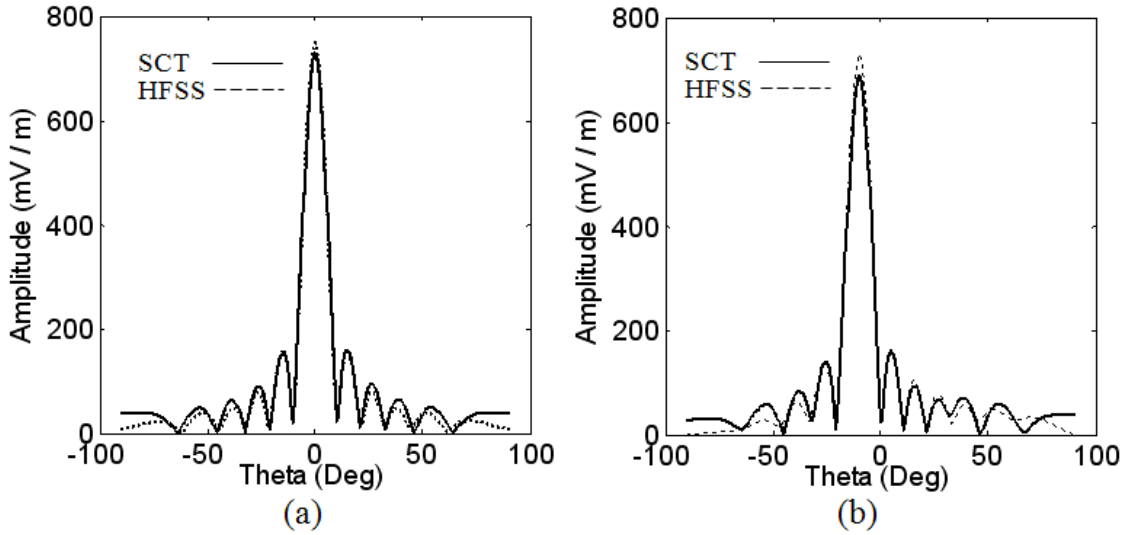

Figure 6.13: (a) E- plane radiation patterns of a 8×8 uniform reflectarray of identical patches under normal plane wave incidence, both patterns are symmetrical (b) H-plane pattern of the same reflectarray under oblique incidence (θ=10°), E-plane pattern is similar as shown in (a).

6.4.2. Microstrip Reflectarray with Non-identical Unit Cells (Steer Beam Case)

As a third case a non-uniform reflectarray of 64 elements shown in Figure 6.14 is analyzed. The array is constructed by varying cell-geometries along horizontal axis whereas the array is kept symmetric along vertical axis. This means that a maximum energy shift is expected in H-plane (i.e., non-uniform pattern) when the incident field is polarized in the vertical direction. The field magnitude in the E-plane will be negligible.

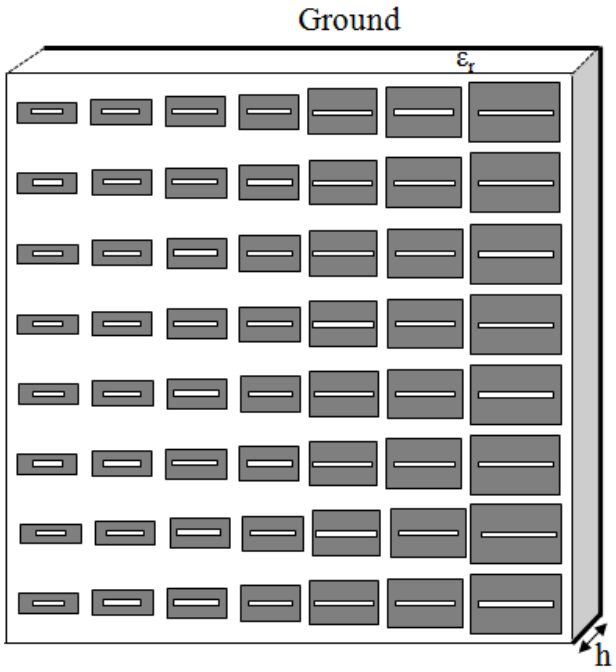

Figure 6.14: Geometry of non-uniform reflectarray, patch width (b_1) and slot length (a_2) are different for each array element as given in Table 6.1.

The variations in the dimensions of the patch and slot introduce a non-uniform mutual coupling between the array elements. The individual unit-cell of the array is the same as shown in Figure 11(c) except with different values of a_2 and b_1 for each unit cell along x-axis. These eight different configurations of unit cells are given Table I.

Table 6.1

Different *8* Unit Cell Configurations

Configuration	1	2	3	4	5	6	7	8
b_1 (mm)	6	6	6	6	8	10	12	13
a_2 (mm)	5.52	7.2	8.12	9.42	11.08	11.54	11.18	12.32

This reflectarray is designed to steer the beam with maximum energy in θ=10° direction. The array geometry is assumed under normal plane-wave excitation with the E-field polarized in the vertical direction. The radiation pattern results of the scattered E-field in H-plane are given in Figure 6.15. The magnitude of the E-plane pattern is quite negligible and

hence not shown here. Again in this case, the radiation pattern results obtained by the scale changing technique fully agrees with the results obtained by a simulation tool based on FEM and MoM.

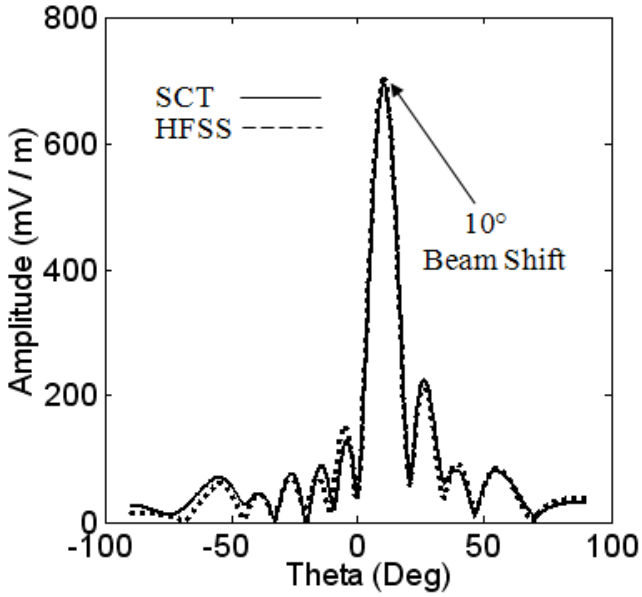

Figure 6.15: H-plane radiation pattern of an 8×8 non-uniform array containing non-identical metallic patches and slots

6.4.3. Scattering Results under Feed Horn Excitation

In the above sub-section both uniform and non-uniform planar structures were simulated under plane-wave incidence. The plane-wave excitation condition is valid for the applications where the planar structure is used at a far receiving end or when the excitation source is placed very far from the surface of the array. In most practical applications an antenna illumination source is placed in close proximity to the planar array therefore it needs to be simulated along with the planar structure.

As SCT is a 2.5D simulation technique it cannot be directly applied to simulate 3D antenna sources. To incorporate the source in the simulations, SCT can be used in hybrid with other 3D modeling tools. For example, a source antenna can be modeled using tools like GRASP, FEKO or HFSS and the projection of the radiation fields in the array domain can be used in SCT as an excitation source. Alternatively, some antennas can be modeled analytically e.g. analytical modeling of a pyramidal horn is detailed in Appendix B.

6.4.3.1. Radiation Characteristics of Pyramidal Horn

The scattering behavior of a pyramidal horn antenna shown in Figure 6.16 has been modeled analytically by the scattering behavior of a radiating aperture mounted on an infinite ground plane. Taking aperture dimensions equal to that of horn's aperture and a similar aperture field distribution, the far-field radiation patterns of the aperture can approximate the horn's radiation pattern over certain range of the elevation angle in the main-beam direction. The details of the analytical modeling of pyramidal horn antenna is given in Appendix B.

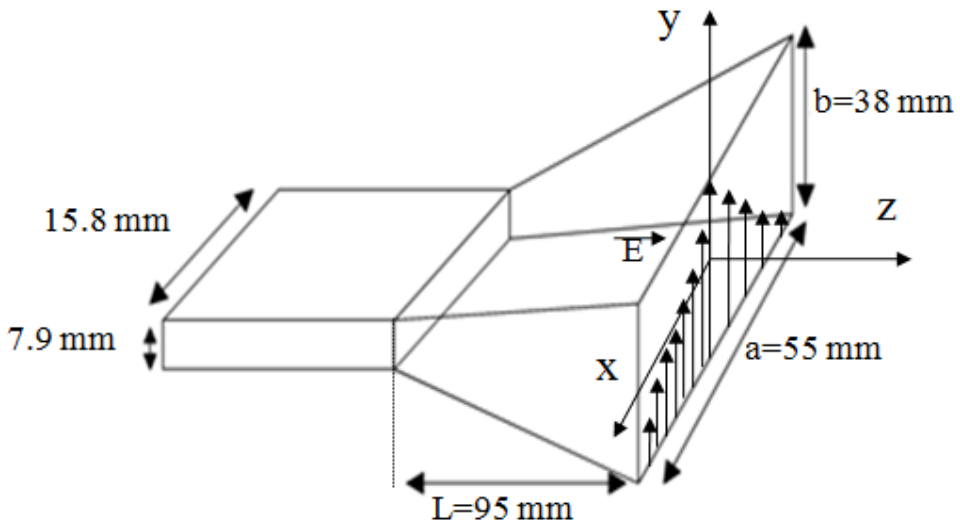

Figure 6.16: Dimension of the pyramidal horn along with its aperture field distribution (TE_{10} mode)

Within the simulation frequency band (10-12.5 GHz), the feed waveguide has only TE_{10} as propagation mode. Therefore the field distribution at the aperture of the horn can be approximated by TE_{10} mode distribution. Analytical expressions of electric fields radiated from an aperture mounted on an infinite ground plane with TE_{10}-mode distribution can easily be found in the literature [57]. The far-field radiation patterns from the aperture have been compared to that of the pyramidal horn radiation patterns in Figure 6.17 to confirm the validity of the approximation.

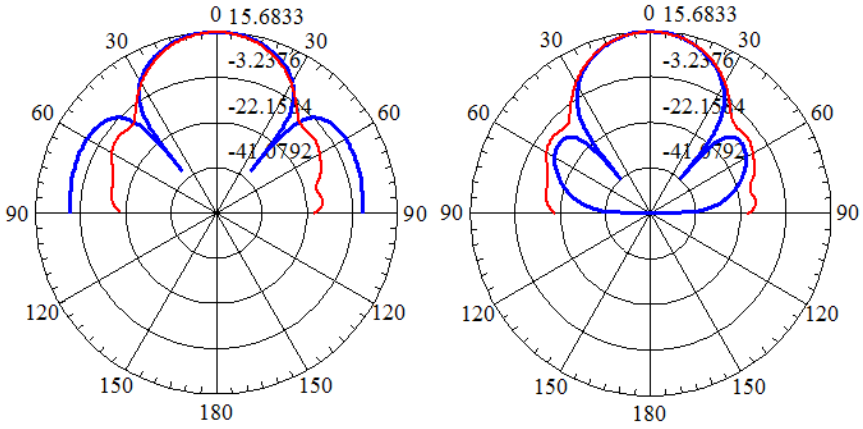

(a) (b)

Figure 6.17: Directivity pattern of the pyramidal horn (blue) compared to that of aperture antenna (red) at 12.5 GHz (a) E-plane (b) H-plane

It is clear from both H-plane and E-plane radiation pattern results that for the elevation angles between -30º and 30º, the two results overlap precisely. Therefore as long as the planar array is placed within this source elevation range, the behavior of the horn can be modeled accurately by a radiating aperture of comparable dimensions. This approximation holds only if the source horn is placed at a distance greater than $2D^2/\lambda$ (where D is the largest horn dimension) which may not always be the case in practical applications. Nonetheless, this approach is presented here as an example to demonstrate how the excitation sources can be incorporated with SCT simulations.

6.4.3.2. Radiation Pattern Results

For practical applications the source antenna is not usually placed directly at the top of centre of the planar structure to avoid the masking effect of the source on the backscattered field. Conventionally it is placed at an offset with respect to the center of the planar structure with a certain angle of inclination to center the main lobe of the antenna in the middle of the array (see Figure 6.18).

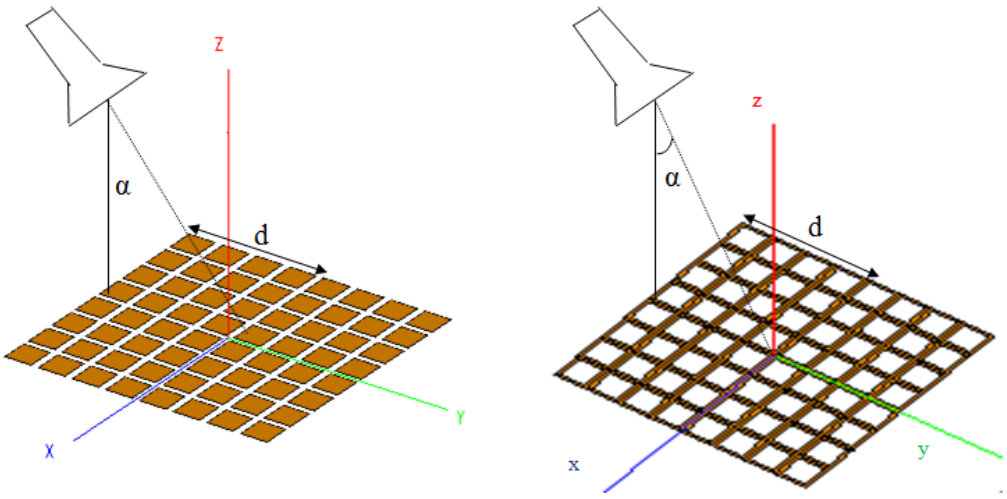

Figure 6.18: Basic configuration of free-standing planar structures with feed horn (a) metallic patch structure: patch dims 13.5x13, unit-cell dims 16.8x16.8 (b) metal grid structure: aperture dims 13.5 x 13, unit- cell dims 16.8 x 16.8 (all dimensions are in mm).

The two planar structures consisting of microstrip patches and of grid with size 134.4mm × 134.4mm are shown in Figure 6.18 respectively. They are simulated by Scale Changing Technique and MoM based technique (FEKO) at 12.5GHz and 10GHz respectively. FEKO was chosen due to its surface meshing capability contrary to HFSS which performs meshing in the whole volume and therefore cannot be used with the memory resources available on a common PC. The feed horn is placed at 660mm with offset distance 'd' equal to 134.4 mm from the centre of the structures. The inclination angle 'α' is taken equal to 7° to centre the main beam of the feed horn on the planar structures. The simulated radiation pattern results for both types of the structures are shown in Figure 6.19 and Figure 6.20 respectively.

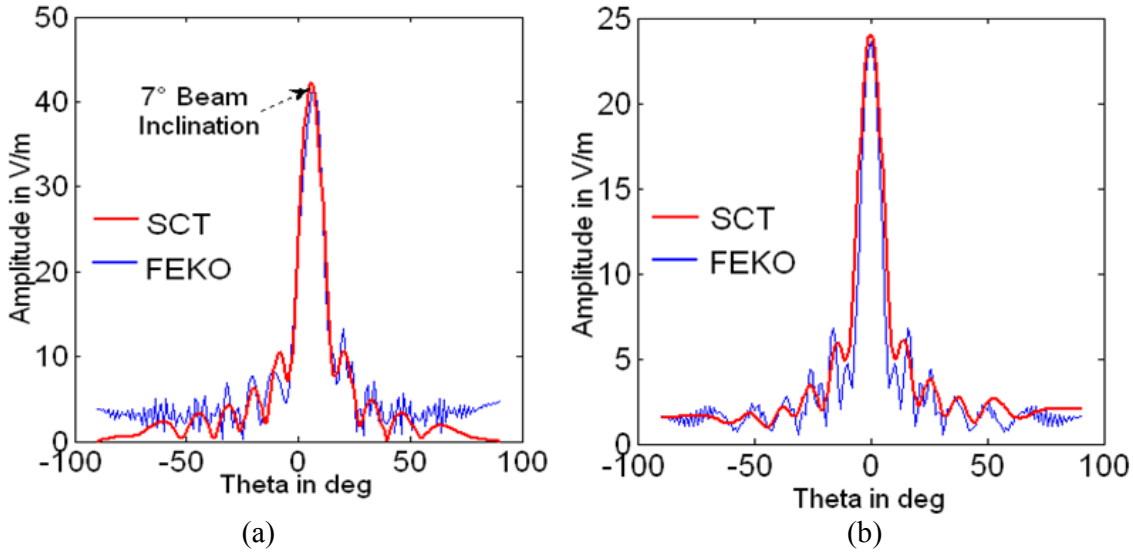

Figure 6.19: Radiation pattern diagrams for an 8x8 uniform metallic patch structure at 12.5GHz (a) E-Plane pattern (b) H-Plane pattern

Since an inclination of 7° is given to the feed horn to orient its main beam to the plane of the structures, this effect is observed by 7º displacement of main backscattered lobe in the E-plane. In the H-plane the pattern is symmetric around 0º as expected.

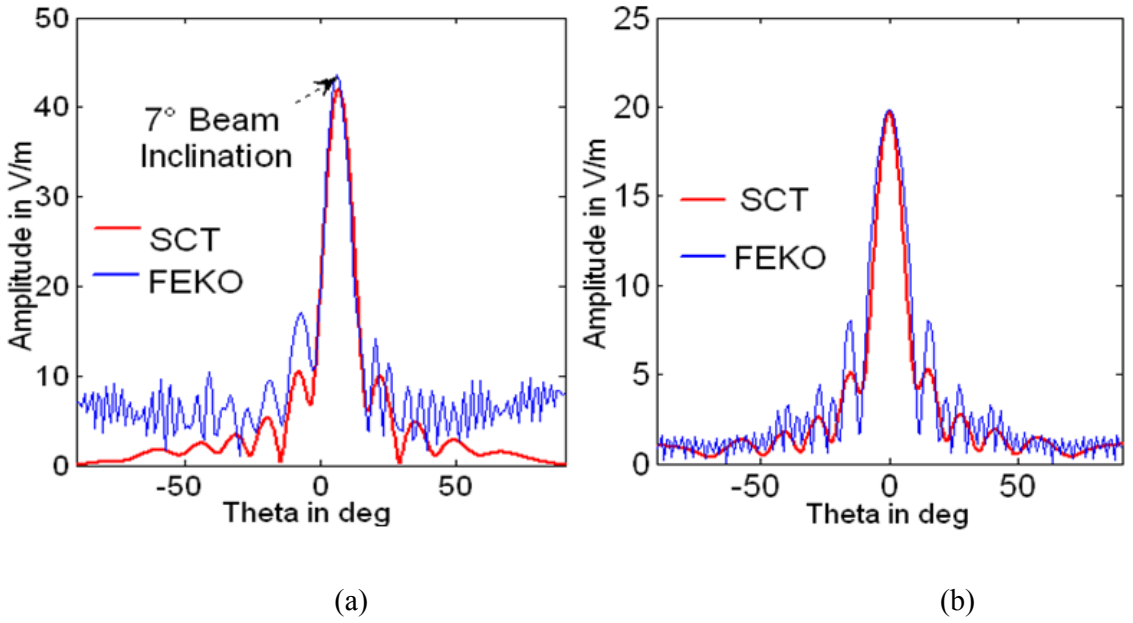

Figure 6.20: Radiation pattern diagrams for an 8x8 uniform metallic grid structure at 10GHz (a) E-Plane pattern (b) H-Plane pattern

The non-normalized comparison shows good agreement in the magnitude as well as main-lobe position of the reflected field components. For all FEKO results, rapid jittery variations

may be due to the convergence errors as the meshing step is not fine enough. For all FEKO results presented here, λ/10 is taken as mesh-step. A smaller step cannot be used due to the limitations of memory resources. Nevertheless the FEKO results validate the general form and amplitude of the SCT scattered field patterns.

6.5. Comparative Study of Execution Times

The execution times for SCT simulations depend on a number of factors. The scattering patterns are calculated from the equivalent surface current defined by the equation (6.26). The solution of the fore-mentioned equation requires the computation of three matrices i.e., $[Z_{space}]$ (the matrix representation of the free-space dyadic Green function), $[V_{inc}]$ (the vector containing the known expansion coefficients of the incident electric-field) and $[Z_s]$ (surface impedance matrix modeling the whole reflectarray structure). All these matrix representations are given in the set of active modes in the domain *D* of the array. The computation of both $[Z_{space}]$ and $[V_{inc}]$ does not involve the application of SCT and they are not required to be recomputed if any change is made to an individual cell-geometry at lower scales (their re-computation is required only if the number N_D of active modes at the top-scale is modified for analyzing the numerical convergence of the solution). Therefore in parametric studies and optimization loops, the computation time of $[Z_s]$ is the most important.

The computation of $[Z_s]$ depends on the size of the array as well as the unit-cell geometries. Size of the array will determine the number of scale-changing networks to be computed where as the unit-cell geometry will principally determine the number of active and passive modes required to compute the surface-impedance matrices. Also if two or more cells have the same geometry, the surface impedance matrix for each of them needs to be calculated only once.

Table 6.2

Computation time for 8×8 uniform patch slot array

CPU Time (sec)

	SCT	HFSS
Complete reflectarray	55.23	829.43
Zs of unit-cell	13.19	
SCN (120 active 4000 passive) (1 SCN + 4 case)	14.2	
SCN (200 active 4000 passive) (1 SCN + 2 case)	11.9	
SCN (300 active 4000 passive) (1 SCN + 1 case)	8.3	

In the case of a 64-elements (8×8) uniform patch-slot array, only one surface-impedance matrix needs to be computed along with three scale-changing networks to compute the multimodal surface impedance for the entire array. The whole process takes around 55 seconds with a 3.2 GHz Intel ×86 family processor with 2GB RAM (see Table 6.2**)**. At scale-level S=1, single-unit cell requires 8 seconds to compute; at scale S=2 one scale-changing network along with a single cascade (scale-changing network with 4 surface impedance matrices) requires 11.9 seconds and so on. For a uniform array case, at each scale-level only a single scale-changing network and a single cascade computation need to be performed.

Table 6.3

Computation time for 8×8 non-uniform patch slot array

CPU Time (sec)

	SCT	HFSS
Complete reflectarray	192.5	1340.03
Zs of unit-cell (8 Configs)	144.2	
SCN (100 active 4000 passive) (1 SCN + 4 case)	21.6	
SCN (200 active 4000 passive) (1 SCN + 2 case)	15.45	
SCN (300 active 4000 passive) (1 SCN + 1 case)	9.1	

The execution times in the case of an 8×8 non-uniform patch-slot array with 8 different unit-cell configurations are given in Table 6.3. In this case at the scale-level S=1, eight surface impedance matrices have to be computed, each corresponding to one geometric configuration. At scale-level S=2, one scale-changing network has to be computed but 4 cascades need to be performed. The process continues likewise at higher scales. It is clear from these results that SCT make use of redundant nature of the geometry to efficiently characterize the whole structure. It can be deduced from the results of Table 6.3, that in the case of an array where all unit-cells differ from one another, the CPU time required to compute $[Z_s]$ of the complete array would be around 1130 seconds. Figure 6.21 plots the simulation time against the array-size in case of two simulation techniques. If the array-size is represented in the number of unit-cells *N* then for each iteration *n* the size of the array is given as $N=2^n$. In other words, for each size-iteration the unit-cells in the array double from the previous value.

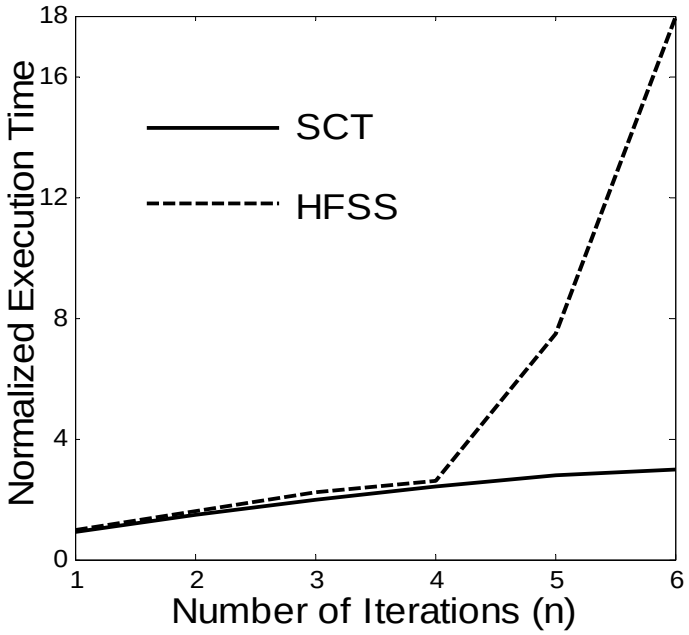

Figure 6.21: Evolution of the normalized computation time with respect to bifurcation iterations used. For an iteration *n* the array consists of 2^n cells.

In the Figure 6.21 , for each technique the execution time results are normalized with respect to the time required to simulate an array of two unit-cells (n=1). In case of SCT, the execution time for simulating uniform reflectarray increases linearly with increase in the number of iterations (i.e., $n = ln(N)/ln(2)$). However this is not the case for HFSS and

other techniques that uses linear mesh-refinement procedure. The behavior is similar to that observed in the metallic strip array case as expected. The linear behavior of SCT comes from the fact that for all similar unit-cells only one scale-changing network needs to be calculated to represent all of them. This allows faster and better convergence for SCT results as compared to Finite Element Method using spatial meshing. In case of non-uniform arrays the linear behavior can be achieved by executing individual scale-changing networks in parallel on multiple processors. It should be noted that the same reflectarrays have also been simulated with CST (using both frequency and time domain solvers) [71], FEKO (using MLFMM) [72] and IE3D [73], but all of these simulation tools approximately share the same requirements regarding execution times and memory resources and the SCT proved to be much more efficient than all of these techniques.

6.6. Microstrip Reflectarray Electronically Tunable with RF-MEMS Switches (Reconfigurable Case)

In this Section a brief description of SCT modeling for a small 1D reconfigurable reflectarray electronically tunable with RF-MEMS switches is presented. The detailed introduction and benefits of RF MEMS-based reflectarray has already been given in chapter 1.

6.6.1. Application of Electrical Circuit Model to find out appropriate Cell Configurations

The design and optimization of the MEMS-controlled phase shifters for such active reflectarray antennas has also been presented in detail in chapters 2 and 3 respectively. This small active reflectarray is basically an intermediate step towards the simulation by SCT of

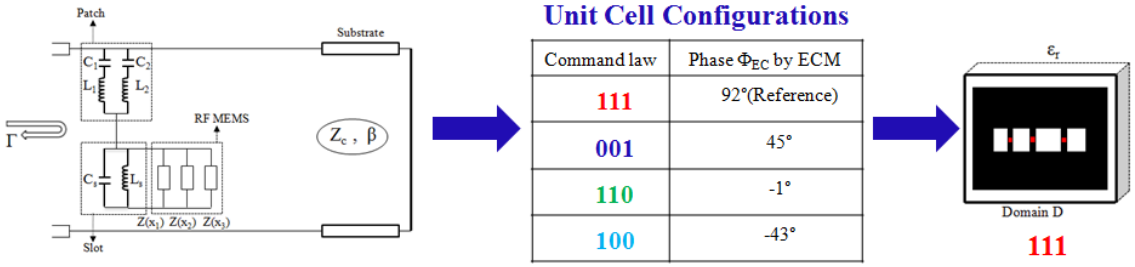

Figure 6.22: Application of the circuit model to find out individual phase shifter configurations for a reconfigurable reflectarray containing RF-MEMS switches.

large 2D reflectarrays containing RF-MEMS as tunable electronic devices. As shown in Figure 6.22, the electrical circuit model is applied to find out such phase shifter configurations that give us the desired progressive phase shift in the radiated beam. For this purpose, by using the equivalent circuit model and applying the design equation (6.33), we determined four different phase shifter configurations that collectively provide 10^{o} beam shift in the horizontal direction (as only β_x is taken) i.e., left and in the right by varying the states of the RF-MEMS switches.

$$\beta_x = -k_0 d \sin\theta\,,\ taking\ \theta = \pm 10°, \beta_x = \mp 43.72° \tag{6.34}$$

This four cell reconfigurable reflectarray containing four phase shifter cells controlled by RF-MEMS switches designed by equivalent circuit model is shown in Figure 6.23.

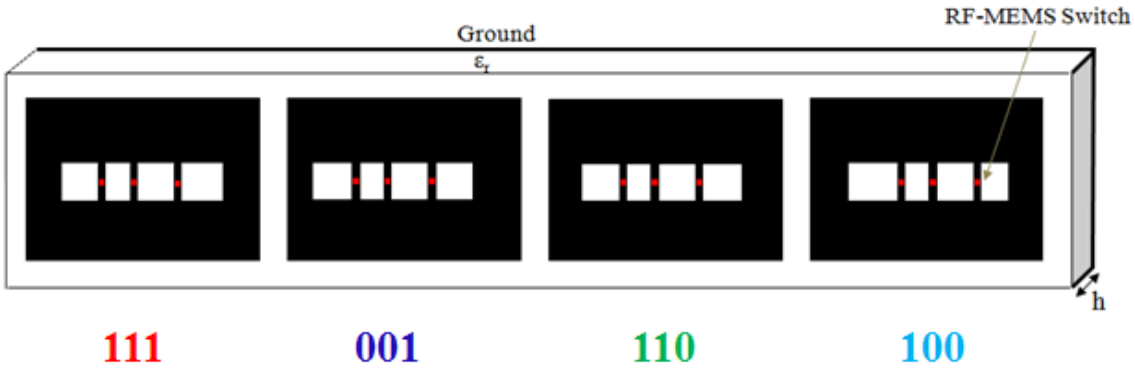

Figure 6.23: A 4-cell (4x1) reconfigurable reflectarray, all the dimensions are the same as given in Figure 1 of Chapter 2.

6.6.1. SCT Modeling of Reconfigurable Reflectarray

Each RF-MEMS switch is modeled by its surface impedance and then this surface impedance is used in the SCT modeling of the whole phase shifter cell. The following Figures 6.24 and 6.25 present the SCT partitioning process of the active phase shifter cell controlled by three MEMS switches and the respective Scale Changing Network diagram respectively.

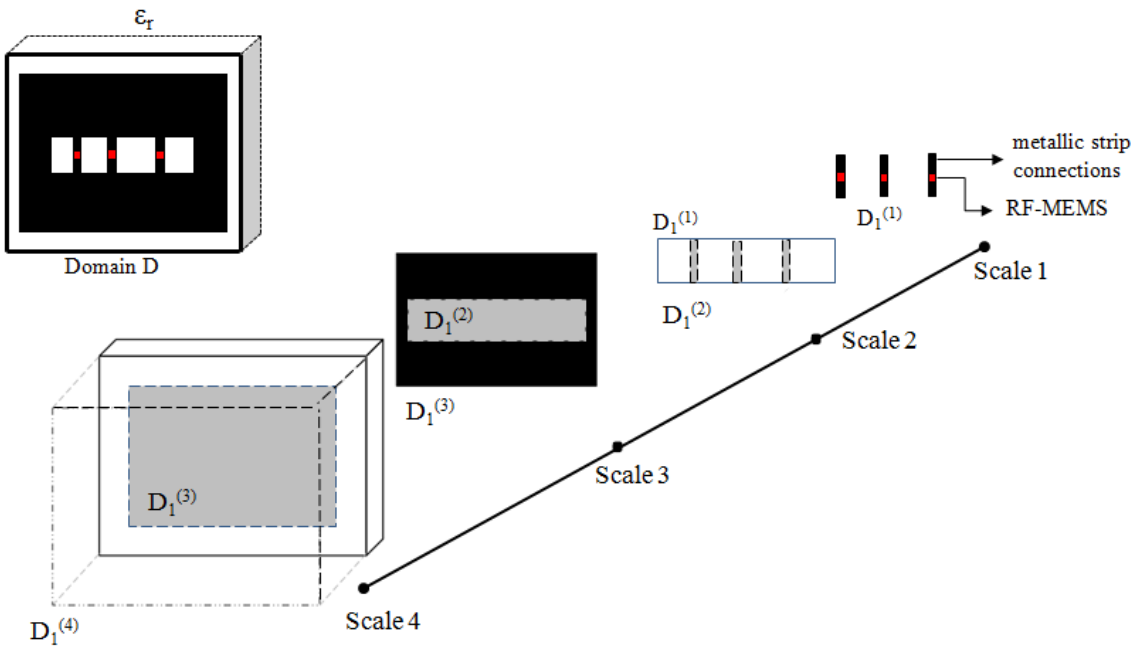

Figure 6.24: Partitioning of the discontinuity plane D of the active phase shifter cell in its constituent domains and sub-domains in four scales, white portions represent dielectric, black represents metal, grey parts represent un-partitioned sub-domains and red represents the RF- MEMS switch.

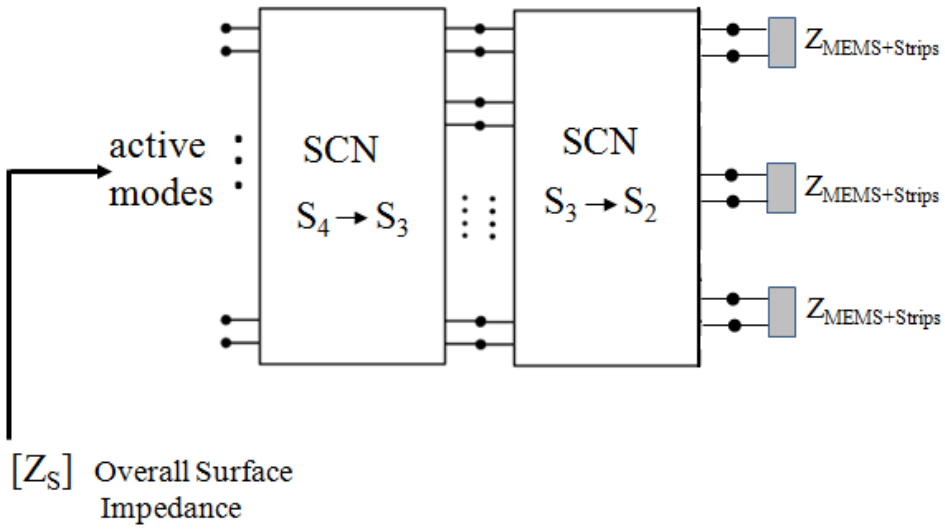

Figure 6.25: Global simulation of the planar reflector involves the cascade of the scale-changing networks and the surface impedances of RF-MEMS switches.

6.6.2. Radiation Pattern Results

The active array shown in Figure 6.22 is simulated by the SCT and HFSS. First, the configuration (i.e., the ON/OFF states) of the RF-MEMS for all four phase shifter cells are kept identical, here, the pattern of the states of MEMS switches for all four unit cells is as

follows: [001, 001, 001, 001] where 1 and 0 represent the ON and OFF states of the switches respectively. By keeping the configuration same for all four phase shifter, the symmetrical radiation patterns has been obtained in E and H planes as shown in Figure 6.25.

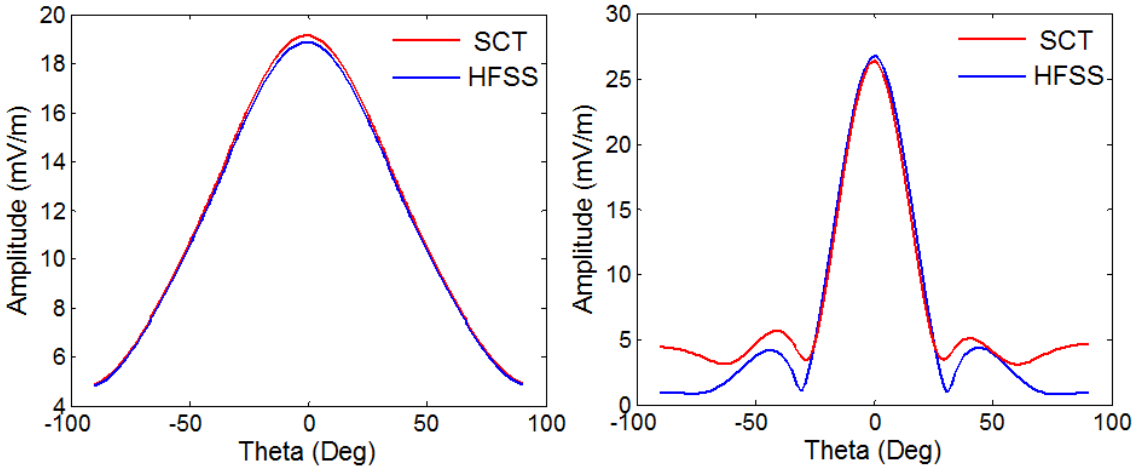

(a) (b)

Figure 6.25: Radiation patterns of 4-cell reconfigurable reflectarray of Figure 6.23 keeping the electronic configuration (i.e., the switching states ON/OFF) for the twelve RF-MEMS switches of four phase shifter cells identical and hence obtaining both E and H plane patterns symmetrical (a) E-plane pattern (b) H-plane pattern

Second, the configuration of the RF-MEMS of each phase shifter cell is made different from each other to obtain a desired beam shift in a specific direction. Here in this case, the RF-MEMS states of each cell are selected such that they provide 10° beam shift in right and 10° beam shift in left as shown in Figure 6.26. The configuration pattern of the RF-MEMS states for each beam steering case is given in the caption of the Figure 6.26.

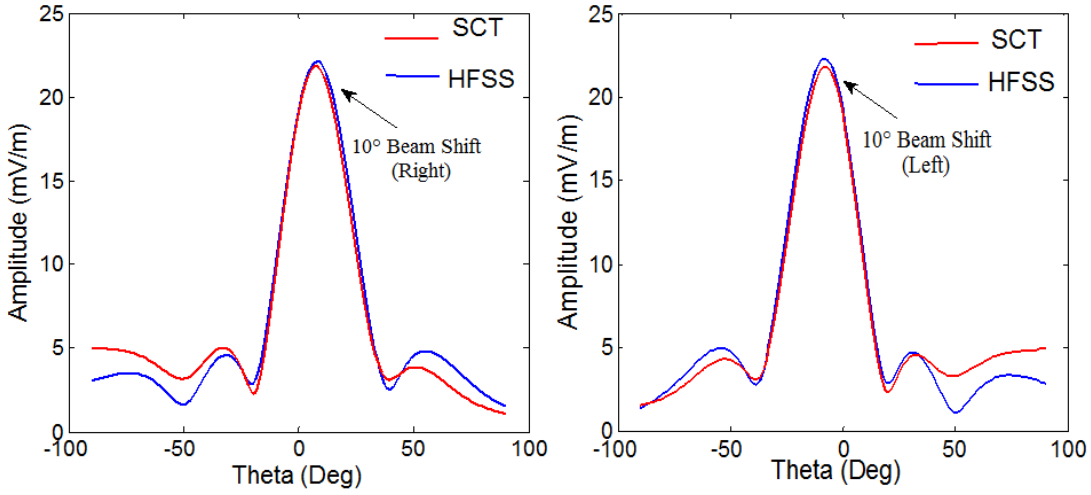

(a) (b)

Figure 6.26: Un-normalized radiation patterns of 4-cell reconfigurable reflectarray of Figure 6.23, the electronic configuration (i.e., the switching states ON/OFF) for the twelve RF-MEMS switches of four phase shifter cells are non-identical and hence obtaining H plane patterns asymmetrical (a) H-plane pattern with electronic configuration of the four elements as [111 001 110 100] (b) H-plane pattern with electronic configuration as [100 110 001 111].

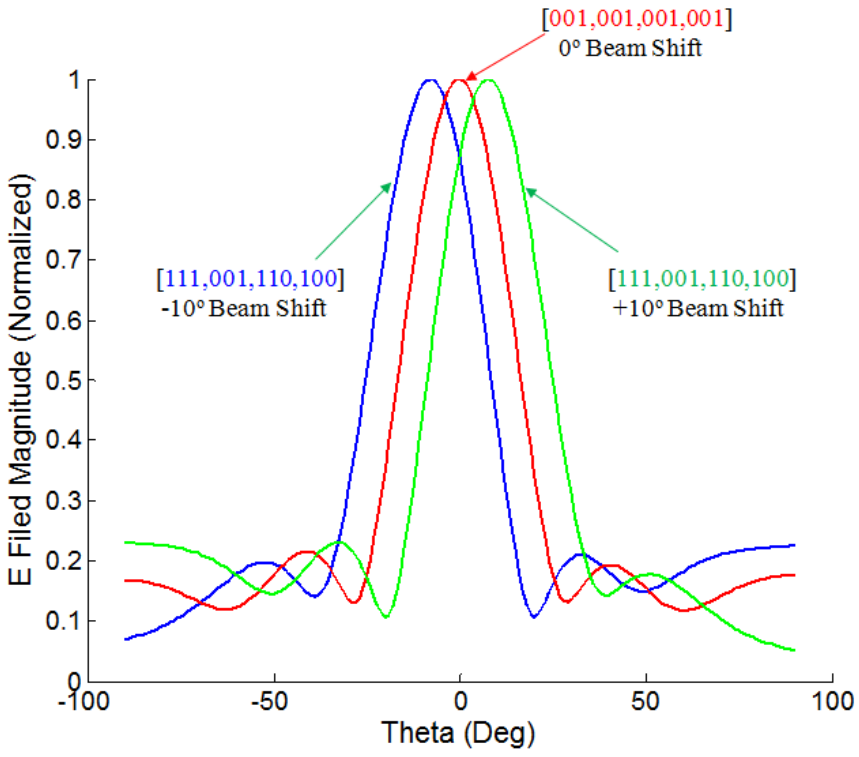

Figure 6.27: Normalized SCT results of 4-cell reconfigurable reflectarray of Figure 6.23, the electronic configurations (i.e., the switching states (ON/OFF) for all the three types are shown in the Figure.

Figure 6.27 puts the SCT results together for the above three cases to make it prominent that how reconfigurability works. The array geometry remains same and we are achieving the dynamic phase control by only varying the ON/OFF states of the RF-MEMS switches. The main center beam is achieved by maintaining the identical ON/OFF state pattern for all the four phase shifter elements, while to steer the beam in the desired direction (here +10° and -10°), the ON/OFF states must be designed accordingly as shown in Figure 6.27.

6.7. Conclusions

In this chapter the scale changing technique (SCT) has been successfully applied to characterize several planar structures. In the first part of the chapter, the concept of a scale-changing network to model the mutual coupling between array elements was introduced. It has been shown that SCT can effectively be used to characterize the mutual coupling in the planar reflectarrays. This was demonstrated both in the case of mutual coupling between two half-wave dipole elements as well as between the elements in a planar dipole array.

Later in this chapter, the SCT has been applied to the problem of electromagnetic scattering from two dimensional uniform and non-uniform reflectarray structures. The scattered field patterns are calculated under plane-wave and horn-antenna excitation. These results are compared to the simulation results from other 3D full-wave analysis tools. Next, the comparison between the execution times to compute the surface impedances in the case of both uniform and non-uniform arrays are given. It has been shown that SCT effectively reuses the redundancy in a design. Moreover, the highly parallelizable execution capability of scale-changing network makes SCT a promising tool to design, analyze and optimize large complex planar structures, which is not usually convenient to do with the existing techniques. At the end, a small case of an active reflectarray is discussed. The modeling of large 2D active reflectarray tunable by RF-MEMS switches is underway.

The greatest discovery of all time is that a person can change his future by merely changing his attitude.
Oprah Winfrey

7

Conclusions and Perspectives

The aim of this chapter is to sum up all the work presented in this thesis, and then obtain a constructive conclusion that would help in the future development based on this research work.

The primary motive of this thesis was to develop a methodology through which the electromagnetic (EM) scattering analysis of the modern complex multi-scale antenna structures could be carried out more efficiently in terms of computational resources. To achieve this objective, a new modeling technique called Scale-Changing Technique (SCT) has been implemented and applied for EM modeling of the large finite-sized microstrip reflectarrays. Although, this technique is itself very fast in terms of execution times and memory resources, however to accelerate the design, analysis and optimization process of the reflectarrays, an equivalent circuit model of passive and active phase shifter elements has also been introduced. This equivalent circuit model is quite helpful for rapid designing of reflectarray phase shifter cells containing patches, slots and RF-MEMS switches.

After a careful study and systematic evaluation of different reflectarray element designs, it had been decided that the element – patch loaded with slot is best suited keeping in mind the future RF-MEMS implementation. In chapters 2 and 3 the extraction and working of the equivalent circuit models for a passive reflectarray phase shifter cells (a cell loaded with microstrip patch and slot) and active reflectarray phase shifter cells (a cell loaded with

microstrip patch, slot and RF-MEMS) have been fully explained. These equivalent circuits are then used for the rapid design and optimization of the individual unit cells of the passive and reconfigurable reflectarrays. These equivalent circuits present a very fast method to find a more power efficient design of MEMS-controlled phase shifter cells having 360° phase range. This circuit model takes three parameters as design inputs i.e., the number, the ON/OFF state and the locations of the MEMS switches within the slot. Depending on these three parameters, it helps to search out such unit cell configurations that provide 360° phase range with linear distribution of the selected phases over this range. Very good agreement in comparison with contemporary computational electromagnetics (CEM) softwares has been obtained. Moreover, this equivalent electrical circuit provides a better understanding of how a particular phase shifter cell operates and it potentially allows fast synthesis of reflectarray cells by optimization of circuit parameters to achieve the desired frequency response and angular behavior.

In the Section II of the thesis, the SCT technique based on interconnecting Scale-Changing Networks has been applied for the electromagnetic modeling of planar reflectarray structures. The problem of electromagnetic scattering from these arrays was addressed and it has been shown that the Scale-Changing Technique can effectively be used to calculate the field scattering patterns and surface currents. In the course of this thesis SCT has been applied to the scattering problem of several planar reflectarrays and it has been demonstrated that the technique effectively models the mutual interactions between the array elements.

The unique formulation of the Scale-Changing Technique avoids the direct computation of structures with high aspect ratios. Thanks to hierarchical domain-decomposition provided by the partitioning process, the complex geometries are broken down into finite number of simpler geometries at distinct scale-levels. Moreover, the scale-changing networks which relate the electromagnetic fields at adjacent scales are computed separately, therefore providing an inherent parallelization capability. Typically, if N orders of magnitude separate the largest to the smallest dimensions in the structure, the Scale-Changing Technique requires the computation of N Scale-Changing Networks, while tremendous execution time and memory resources are required by other numerical techniques for handling the corresponding aspect ratio of 10^N.

The SCT is a generic approach and can be advantageously applied to the modeling of microwave and millimeter wave circuits with high aspect ratios, MEMS-controlled coupled

microstrip reflectarrays and multiscale pre-fractal structures. The modular nature of the technique can be exploited by distributed processing algorithms (Grid Computing Methods) to reduce the simulation time many fold. Similarly the convergence study (finding the appropriate number of active and passive modes at each domain) can be parallelized by running convergence passes as separate processes. It has been demonstrated that for certain planar structures the simulation times can be reduced by 90% by implementing both of above stated approaches [74].

Domain decomposition not only allows the rapid processing of the overall simulation, it also helps solving the memory problems for simulating large structures. As the complex problem is now partitioned into much smaller problems, the new equations are made up of fewer unknowns and thus can be represented by smaller matrices requiring much less memory resources. In addition this gradual change of dimensions from one scale-level to the next helps to avoid the numerical conditioning errors linked to critical aspect ratios in a structure.

In design and optimization processes small modifications in the structure geometry is often required. For example, if modifications in the structure geometry occur at a given scale S, only the SCNs between scale S and S-1 and between S and S+1 need to be recalculated. This gives SCT a huge advantage on classical meshing based techniques which require the recalculation of the overall structure. This built-in modularity makes the scale-changing technique a very powerful optimization and parameterization tool.

Although as a stand-alone method, SCT is applicable only to 2D or 2.5D planar structures, but it can be used in hybrid with other classical methods for 3D applications. The idea is to use the SCT for the planar sub-domains and one of the classical methods e.g. FDTD, FEM or TLM for the volume sub-domains. The interlinking between the methods can be performed using integral equation (IE) formulation by relating tangential electromagnetic fields at the exterior surfaces of the volume sub-domains to the active modes of the planar sub-domains.

Apart from all the positive features SCT has its own limitations. First of all, there is no simple and automatic convergence criterion for determining the number of coupling (active) modes in the sub-domains. For the moment the appropriate number of active modes has to be manually determined from the convergence curves. Moreover in certain cases the matrix ill-

conditioning problems may lead to numerical convergence issues requiring additional processing e.g. iterative solver methods to resolve them.

Presently, planar structures comprised of simple canonical domains have been treated only. The rectangular domains and sub-domains allow the field description in terms of purely analytical entire-domain trail functions and therefore save the complex numerical treatment necessary in the case of non-analytical trial functions required to describe the electromagnetic field in non-canonical shaped domains.

Another limitation concerns the introduction of artificial boundary conditions at the boundaries of domains formed by the partitioning process. Normally these boundary conditions are selected taking into account physical nature of the problem that is the behavior of electromagnetic fields in their vicinity. But even a different set of boundary conditions does not seem to affect the accuracy of the solution significantly, only in this case the solution would need a larger number of modes to converge.

Concerning the perspectives of this research work, it will be highly interesting to design a real-life planar array application e.g. a Cassegrain FSS or a reflectarray using Scale-Changing Technique and a possible optimization using Grid-computing. The experimental validation of such a case would help to demonstrate the potential of the SCT in the design and analysis of real-life applications. Also the application of the SCT to the electromagnetic modeling of reconfigurable reflectarrays composed of coupled MEMS-controlled planar phase shifters under both plane wave and feed horn excitation is a task of future work.

Don't handicap your children by making their lives easy.
Robert A. Heinlein

Appendices

Success is never final. Failure is never fatal. It's courage that counts.
John Wooden

APPENDIX A

DEFINITIONS OF ORTHOGNAL MODAL-BASIS

A.1. INTRODUCTION

This annex gives the expressions of the orthogonal modal-basis for the various kinds of boundary conditions described in chapter 4 of this thesis. Assuming a rectangular domain of dimensions A (along x-axis) and B (along y-axis) with the lower left corner placed at the origin as shown in Figure A.1

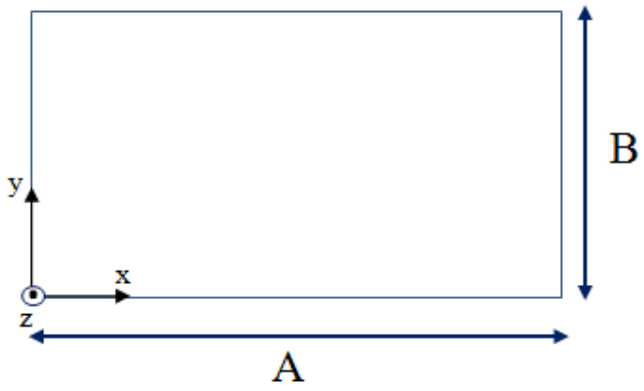

Figure A.1: A rectangular domain based at origin.

If this rectangular domain is bounded by any of the following boundary conditions, the transverse electromagnetic field in the domain can be expressed on the orthogonal modes as under.

A.2. ELECTRIC BOUNDARY CONDITIONS

The rectangular domain is bounded by perfect electric boundary conditions on all sides.

$$\vec{f}^{\alpha}(x,y) = \begin{cases} M^{\alpha}\, cos\left(\frac{m\pi}{A}x\right) sin\left(\frac{n\pi}{B}y\right)\vec{x} \\ N^{\alpha}\, sin\left(\frac{m\pi}{A}x\right) cos\left(\frac{n\pi}{B}y\right)\vec{y} \end{cases}$$

$$where\ \ \alpha = TE, TM\ \ A\ and\ B\ are\ the\ dimensions\ of\ the\ array$$

$$M^{\alpha} = \begin{Bmatrix} -\frac{n}{B}\frac{\sqrt{2T}}{\sqrt{m^2\left(\frac{B}{A}\right)+n^2\left(\frac{A}{B}\right)}} & (TE) \\ \frac{m}{A}\frac{\sqrt{2T}}{\sqrt{m^2\left(\frac{B}{A}\right)+n^2\left(\frac{A}{B}\right)}} & (TM) \end{Bmatrix} \quad N^{\alpha} = \begin{Bmatrix} \frac{m}{A}\frac{\sqrt{2T}}{\sqrt{m^2\left(\frac{B}{A}\right)+n^2\left(\frac{A}{B}\right)}} & (TE) \\ \frac{n}{B}\frac{\sqrt{2T}}{\sqrt{m^2\left(\frac{B}{A}\right)+n^2\left(\frac{A}{B}\right)}} & (TM) \end{Bmatrix}$$

$$where \begin{cases} T = 1 & m \; or \; n = 0 \\ T = 2 & otherwise \end{cases}$$

A.3. MAGNETIC BOUNDARY CONDITIONS

The rectangular domain is bounded by perfect magnetic boundary conditions on all sides.

$$\vec{f}^{\alpha}(x,y) = \begin{cases} M^{\alpha} \, sin\left(\frac{m\pi}{A}x\right) cos\left(\frac{n\pi}{B}y\right)\vec{x} \\ N^{\alpha} \, cos\left(\frac{m\pi}{A}x\right) sin\left(\frac{n\pi}{B}y\right)\vec{y} \end{cases}$$

$$where \;\; \alpha = TE, TM \;\; A \; and \; B \; are \; the \; dimensions \; of \; the \; array$$

$$M^{\alpha} = \begin{Bmatrix} -\frac{n}{B}\frac{\sqrt{2T}}{\sqrt{m^2\left(\frac{B}{A}\right)+n^2\left(\frac{A}{B}\right)}} & (TE) \\ \frac{m}{A}\frac{\sqrt{2T}}{\sqrt{m^2\left(\frac{B}{A}\right)+n^2\left(\frac{A}{B}\right)}} & (TM) \end{Bmatrix} \quad N^{\alpha} = \begin{Bmatrix} \frac{m}{A}\frac{\sqrt{2T}}{\sqrt{m^2\left(\frac{B}{A}\right)+n^2\left(\frac{A}{B}\right)}} & (TE) \\ \frac{n}{B}\frac{\sqrt{2T}}{\sqrt{m^2\left(\frac{B}{A}\right)+n^2\left(\frac{A}{B}\right)}} & (TM) \end{Bmatrix}$$

$$where \begin{cases} T = 1 & m \; or \; n = 0 \\ T = 2 & otherwise \end{cases}$$

A.4. PARALLEL PLATE WAWE-GUIDE BOUNDARY CONDITIONS

The rectangular domain is bounded by perfect electric boundary conditions at the top and bottom but perfect magnetic boundary conditions at side walls.

$$\vec{f}^{\alpha}(x,y) = \begin{cases} M^{\alpha} \sin\left(\frac{m\pi}{A}x\right) \sin\left(\frac{n\pi}{B}y\right)\vec{x} \\ N^{\alpha} \cos\left(\frac{m\pi}{A}x\right) \cos\left(\frac{n\pi}{B}y\right)\vec{y} \end{cases}$$

$$where\ \ \alpha = TE, TM\ \ A\ and\ B\ are\ the\ dimensions\ of\ the\ array$$

$$M^{\alpha} = \begin{Bmatrix} -\frac{n}{B}\frac{\sqrt{2T}}{\sqrt{m^2\left(\frac{B}{A}\right)+n^2\left(\frac{A}{B}\right)}} & (TE) \\ -\frac{m}{A}\frac{\sqrt{2T}}{\sqrt{m^2\left(\frac{B}{A}\right)+n^2\left(\frac{A}{B}\right)}} & (TM) \end{Bmatrix} \quad N^{\alpha} = \begin{Bmatrix} -\frac{m}{A}\frac{\sqrt{2T}}{\sqrt{m^2\left(\frac{B}{A}\right)+n^2\left(\frac{A}{B}\right)}} & (TE) \\ \frac{n}{B}\frac{\sqrt{2T}}{\sqrt{m^2\left(\frac{B}{A}\right)+n^2\left(\frac{A}{B}\right)}} & (TM) \end{Bmatrix}$$

$$where\ \begin{cases} T = 1 & m\ or\ n = 0 \\ T = 2 & otherwise \end{cases}$$

For m=n=0, we have a TEM mode, so in this case,

$$\vec{\mathrm{f}}^{\mathrm{TEM}}(x,y) = \frac{1}{\sqrt{\mathrm{AB}}}\vec{\mathrm{y}}$$

A.5. PERIODIC BOUNDARY CONDITIONS

A.5.1. Normal Incidence Case

The rectangular domain is bounded by periodic boundary conditions (Floquet conditions) at all sides.

$$\vec{f}^{\alpha}(x,y) = \begin{cases} M^{\alpha} \exp\left(j\frac{2m\pi}{A}x\right) \exp\left(j\frac{2n\pi}{B}y\right)\vec{x} \\ N^{\alpha} \exp\left(j\frac{2m\pi}{A}x\right) \exp\left(j\frac{2n\pi}{B}y\right)\vec{y} \end{cases}$$

$$where\ \ \alpha = TE, TM\ \ A\ and\ B\ are\ the\ dimensions\ of\ the\ array$$

$$M^{\alpha} = \begin{Bmatrix} j\frac{n}{B}\frac{1}{\sqrt{m^2\left(\frac{B}{A}\right)+n^2\left(\frac{A}{B}\right)}} & (TE) \\ j\frac{m}{A}\frac{1}{\sqrt{m^2\left(\frac{B}{A}\right)+n^2\left(\frac{A}{B}\right)}} & (TM) \end{Bmatrix} \quad N^{\alpha} = \begin{Bmatrix} -j\frac{m}{A}\frac{1}{\sqrt{m^2\left(\frac{B}{A}\right)+n^2\left(\frac{A}{B}\right)}} & (TE) \\ j\frac{n}{B}\frac{1}{\sqrt{m^2\left(\frac{B}{A}\right)+n^2\left(\frac{A}{B}\right)}} & (TM) \end{Bmatrix}$$

For m=n=0, we have two TEM modes, (or modes TE00 and TM00)

$$\vec{f}^{\mathrm{TEM1}}(x,y) = \frac{1}{\sqrt{AB}}\vec{x} \qquad \vec{f}^{\mathrm{TEM2}}(x,y) = \frac{1}{\sqrt{AB}}\vec{y}$$

A.5.2. Oblique Incidence Case

We redefine the modal basis for oblique incidence as follows:

$$\vec{f}^{\alpha} = \begin{cases} A^{\alpha} e^{j\left(\frac{2\pi m}{a_0}+\alpha\right)x} e^{j\left(\frac{2\pi n}{b_0}+\beta\right)y}\vec{x} \\ B^{\alpha} e^{j\left(\frac{2\pi m}{a_0}+\alpha\right)x} e^{j\left(\frac{2\pi n}{b_0}+\beta\right)y}\vec{y} \end{cases}$$

with

$$A = \begin{cases} j\left(\frac{2\pi m}{a_0}+\alpha\right)\frac{1}{\sqrt{\left(\frac{2\pi m}{a_0}+\alpha\right)^2+\left(\frac{2\pi n}{b_0}+\beta\right)^2}}\cdot\frac{1}{\sqrt{a_0 b_0}} & TM \\ j\left(\frac{2\pi n}{b_0}+\beta\right)\frac{1}{\sqrt{\left(\frac{2\pi m}{a_0}+\alpha\right)^2+\left(\frac{2\pi n}{b_0}+\beta\right)^2}}\cdot\frac{1}{\sqrt{a_0 b_0}} & TE \end{cases}$$

$$B = \begin{cases} j\left(\frac{2\pi n}{b_0}+\beta\right)\frac{1}{\sqrt{\left(\frac{2\pi m}{a_0}+\alpha\right)^2+\left(\frac{2\pi n}{b_0}+\beta\right)^2}}\cdot\frac{1}{\sqrt{a_0 b_0}} & TM \\ -j\left(\frac{2\pi m}{a_0}+\alpha\right)\frac{1}{\sqrt{\left(\frac{2\pi m}{a_0}+\alpha\right)^2+\left(\frac{2\pi n}{b_0}+\beta\right)^2}}\frac{1}{\sqrt{a_0 b_0}} & TE \end{cases}$$

Where,

$$A_{mn} = \frac{1}{\sqrt{a_0 b_0}}\cdot\frac{1}{\sqrt{\left(\frac{2\pi m}{a_0}+\alpha\right)^2+\left(\frac{2\pi n}{b_0}+\beta\right)^2}}$$

For m=n=0, we have two TEM modes, (or modes TE00 and TM00)

$$\vec{f}^{TEM1} = \begin{cases} f_x^{TE_{00}} = Ce^{j\alpha x}e^{j\beta x}\vec{x} \\ f_y^{TE_{00}} = -De^{j\alpha x}e^{j\beta x}\vec{y} \end{cases} \qquad \vec{f}^{TEM2} = \begin{cases} f_x^{TM_{00}} = De^{j\alpha x}e^{j\beta x}\vec{x} \\ f_x^{TM_{00}} = Ce^{j\alpha x}e^{j\beta x}\vec{y} \end{cases} \qquad \text{(A.12)}$$

Where,

$$C = \frac{j\beta}{\sqrt{a_0 b_0}}\cdot\frac{1}{\sqrt{\alpha^2+\beta^2}} \ , \qquad D = \frac{j\alpha}{\sqrt{a_0 b_0}}\cdot\frac{1}{\sqrt{\alpha^2+\beta^2}}$$

With,

$$\alpha = -k_o sin\theta cos\theta \ , \quad \beta = -k_o sin\theta sin\theta$$

Family isn't about whose blood you have. It's about who you care about.
Trey Parker

APPEDIX B

MODELING OF SOURCE HORN BY RECTANGULAR APERTURE

B.1. INTRODUCTION

This annex details the mathematical modeling of a pyramidal horn antenna of the dimensions shown in the Figure B.1. At the simulation frequency (12.5GHz), the feed-waveguide has only TE_{10} as the propagation mode. Therefore at the aperture of the horn the field distribution can be approximated to that of TE_{10} mode distribution.

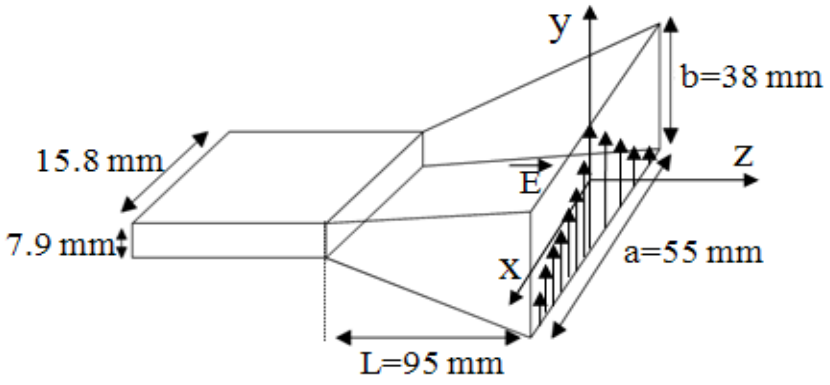

Figure B.1: Dimension of the pyramidal horn along with its aperture field distribution.

B.2. APPROXIMATION BY RADIATING APERTURE

The horn can be treated as an aperture antenna. To find its radiation characteristics, the equivalent principle techniques can be utilized [57]. The fields at the aperture of the horn can be found by treating the horn as a radial waveguide and it can be shown that if the fields of the feed waveguide are those of its dominant TE_{10} mode and horn length is large compared to the aperture dimensions, the field at the aperture of the horn can be approximated as follows:

$$E_a = \hat{a}_y E_0 \cos\left(\frac{\pi}{a}x'\right) \quad \begin{Bmatrix} -\frac{a}{2} \le x' \le +\frac{a}{2} \\ -\frac{b}{2} \le y' \le +\frac{b}{2} \end{Bmatrix}$$

The graphical representation of E_a at the aperture of the horn is shown in the following Figure B.1. Now the three-dimensional distributions of the far-zone fields radiated by the horn aperture are obtained by applying the equivalent principle techniques. In spherical components these fields are given by [57],

$$E_r = H_r = 0$$

$$E_\theta = -\frac{\pi}{2} C \sin\phi \frac{\cos X}{(X^2) - \left(\frac{\pi}{2}\right)^2} \frac{\sin Y}{Y}, \qquad E_\phi = -\frac{\pi}{2} C \cos\theta \cos\phi \frac{\cos X}{(X^2) - \left(\frac{\pi}{2}\right)^2} \frac{\sin Y}{Y}$$

$$H_\theta = -\frac{E_\phi}{\eta} \quad , \quad H_\phi = \frac{E_\theta}{\eta}$$

where

$$X = \frac{ka}{2}\sin\theta\cos\phi \;\; , \;\; Y = \frac{kb}{2}\sin\theta\sin\phi \;\; , \;\; C = j\frac{abkE_0 e^{-jkr}}{2\pi r} \;\; , k = w\sqrt{\mu_0\varepsilon_0} \;\; , \;\; \eta = \sqrt{\frac{\mu_0}{\varepsilon_0}}$$

B.3. TANGENTIAL COMPONENT OF FAR-FIELD

B.3.1. Horn Centered on the Planar Surface

Figure B.2 shows the tangential component E_{tg} of the radiated field on an incident planar surface located in the x-y plane at a distance z=660mm from the feed horn (in the far-field region).

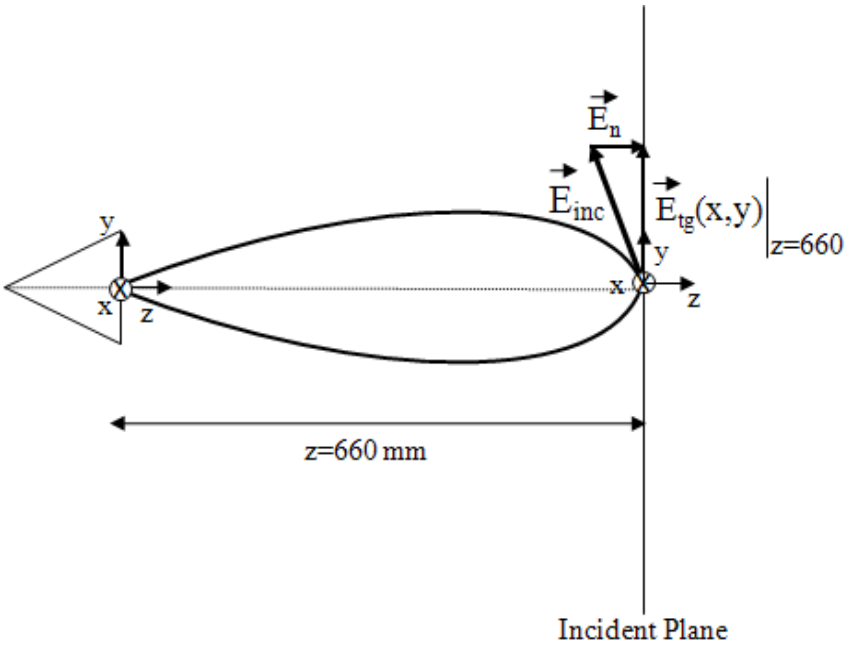

Figure B.2: Computation of the tangential component of the incident field of a horn centered on a planar domain

The incident field can be written in the planar-domain co-ordinate systems as

$$\vec{E}_{inc} = E_x\hat{x} + E_y\hat{y} + E_z\hat{z}$$

Where,

$$E_x = E_r \sin\theta \cos\phi + E_\theta \cos\theta \cos\phi - E_\phi \sin\phi$$

Using far-field expressions from section C.2 in the above equation:

$$E_x = 0 - \frac{\pi}{2} C \sin\phi \frac{\cos X}{(X^2) - \left(\frac{\pi}{2}\right)^2} \frac{\sin Y}{Y} \cos\theta \cos\phi + \frac{\pi}{2} C \cos\theta \cos\phi \frac{\cos X}{(X^2) - \left(\frac{\pi}{2}\right)^2} \frac{\sin Y}{Y} \sin\phi = 0$$

Similarly E_y and E_z can be written as under

$$E_y = E_r \sin\theta \sin\phi + E_\theta \cos\theta \sin\phi + E_\phi \cos\phi$$

$$E_y = 0 - \frac{\pi}{2} C \sin\phi \frac{\cos X}{(X^2) - \left(\frac{\pi}{2}\right)^2} \frac{\sin Y}{Y} \cos\theta \sin\phi - \frac{\pi}{2} C \cos\theta \cos\phi \frac{\cos X}{(X^2) - \left(\frac{\pi}{2}\right)^2} \frac{\sin Y}{Y} \cos\phi$$

$$E_y = -\frac{\pi}{2} C \frac{\cos X}{(X^2) - \left(\frac{\pi}{2}\right)^2} \frac{\sin Y}{Y} \cos\theta \left[\sin\phi^2 + \cos\phi^2\right]$$

$$E_y = -\frac{\pi}{2} C \frac{\cos X}{(X^2) - \left(\frac{\pi}{2}\right)^2} \frac{\sin Y}{Y} \cos\theta$$

$$E_z = E_r \cos\theta - E_\theta \sin\phi$$

$$E_z = \frac{\pi}{2} C \sin\phi \frac{\cos X}{(X^2) - \left(\frac{\pi}{2}\right)^2} \frac{\sin Y}{Y} \sin\theta$$

Now $\vec{E}_{inc}$ and $\vec{E}_{tg}$ can be computed from the following equations.

$$\vec{E}_{inc} = E_x\hat{x} + E_y\hat{y} + E_z\hat{z} = E_y\hat{y} + E_z\hat{z}$$

$$\vec{E}_{tg} = \left(E_y\hat{y} + E_z\hat{z}\right).(\hat{x} + \hat{y})$$

Since planar surface is normal to the plane of the horn's aperture-plane, the tangential field has only the y-component.

$$\vec{E}_{tg} = E_y\hat{y}$$

B.3.2. Horn with an OFF set and Inclination Angle

In most practical cases the horn antenna is not centered on the reflecting structure but placed at an offset to avoid the masking effect. The horn antenna is inclined at a certain angle to position its main beam at the centre of the planar structure. In the figure below the horn antenna is displaced a distance 'd' along the y-axis. Angle α represents the orientation of the feed horn with respect to the co-ordinate system of the incident plane. In this case the tangential electric field $\vec{E}_{tg}$ on the planar surface can be found as follows.

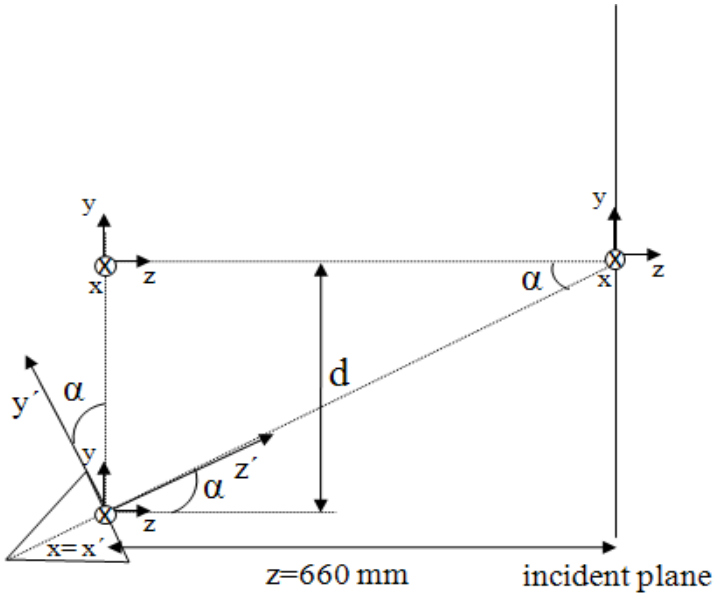

Figure B.3: Computation of the tangential component of the incident field of a horn with an offset and an inclination angle

The new observation point coordinates on the incident plane with respect to the new position and orientation of the feed horn are,

$$x = x'$$

$$y = y' \cos\alpha + z' \sin\alpha$$

$$z = z' \cos\alpha - y' \sin\alpha$$

So the tangential component $\vec{E}_{tg}$ of the field in this case is given by,

$$E_{tg} = \left(E_x \hat{x'} + E_y \hat{y'} + E_z \hat{z'}\right).(\hat{x} + \hat{y})$$

$$E_{tg} = E_x(\hat{x'}.\hat{x}) + E_y(\hat{y'}.\hat{y}) + E_z(\hat{z'}.\hat{y})$$

$$E_{tg} = 0 + E_y \cos\alpha + E_z \sin\alpha$$

$$E_{tg} = E_y \cos\alpha + E_z \sin\alpha$$

B.4. CALCULATION OF $[V_{inc}]$

With parallel-plate boundary conditions as the orthogonal modal basis of the rectangular incident plane, we have

$$[V_{inc}]_{TEM} = \langle \vec{f}, \vec{E}_{tg} \rangle = \iint_{x=0}^{A}\iint_{y=0}^{B} f_y^* \, E_y \, dx \, dy = \frac{1}{\sqrt{AB}} \iint_{x=0}^{A}\iint_{y=0}^{B} E_y \, dx \, dy$$

$$[V_{inc}]_{TE,TM} = \langle \vec{f}, \vec{E}_{tg} \rangle = \iint_{x=0}^{A}\iint_{y=0}^{B} f_y^* \, E_y \, dx \, dy.$$

$$[V_{inc}] = \iint_{x=0}^{A}\iint_{y=0}^{B} N^{\alpha} \cos\left(\frac{m\pi}{A}x\right)\cos\left(\frac{n\pi}{B}y\right) E_y \, dx \, dy$$

Where $\alpha = \text{TE}, \text{TM}$

By using the analytical expression of E_y in the above equation, we get the following integral. This integral is too complex to resolve analytically and therefore has been solved using numerical integration.

$$[V_{inc}]$$

$$= \iint_{x=0}^{A}\iint_{y=0}^{B} \left[N^{\alpha} \cos\left(\frac{m\pi}{A}x\right)\cos\left(\frac{n\pi}{B}y\right)\right]\left[-\frac{\pi}{2}\left(j\frac{abkE_0 e^{-jk\sqrt{x^2+y^2+z^2}}}{2\pi r}\right)\cos\left(\cos^{-1}\frac{z}{\sqrt{x^2+y^2+z^2}}\right)\right]$$

$$\left[\frac{\cos\left(\frac{ka}{2}\sin\left(\cos^{-1}\frac{z}{\sqrt{x^2+y^2+z^2}}\right)\cos\left(\tan^{-1}\frac{y}{x}\right)\right)}{\left(\frac{ka}{2}\sin\left(\cos^{-1}\frac{z}{\sqrt{x^2+y^2+z^2}}\right)\cos\left(\tan^{-1}\frac{y}{x}\right)\right)^2-\left(\frac{\pi}{2}\right)^2}\right]\left[\frac{\sin\left(\frac{kb}{2}\sin\left(\cos^{-1}\frac{z}{\sqrt{x^2+y^2+z^2}}\right)\sin\left(\tan^{-1}\frac{y}{x}\right)\right)}{\frac{kb}{2}\sin\left(\cos^{-1}\frac{z}{\sqrt{x^2+y^2+z^2}}\right)\sin\left(\tan^{-1}\frac{y}{x}\right)}\right]dxdy$$

B.5. RADIATION PATTERN PLOT

Now we plot the magnitude of the tangential component on the planar surface. There are two cases in this respect, first is, in which feed horn is placed normal to incident plane and the second is in which it is placed with some offset and inclination angle, both of these cases are described below.

B.5.1. Horn Centered

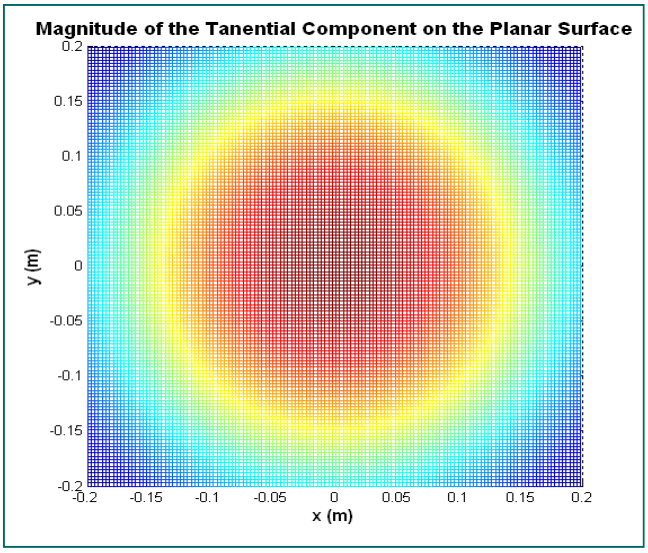

Figure B.4: Tangential field pattern of a horn antenna placed at the center of the planar surface at a distance (d) from it. d=660mm

B.5.2. Horn with an OFF set and Inclination Angle

If the Horn Antenna is at oblique angle α with an offset of d, then we have to simply replace the coordinates x, y and z in the above equation with x′, y′ and z′ as follows:

$$x' = -z\sin\alpha + (x + d)\cos\alpha$$

$$y' = y$$

$$z' = z\cos\alpha + (x + d)\sin\alpha$$

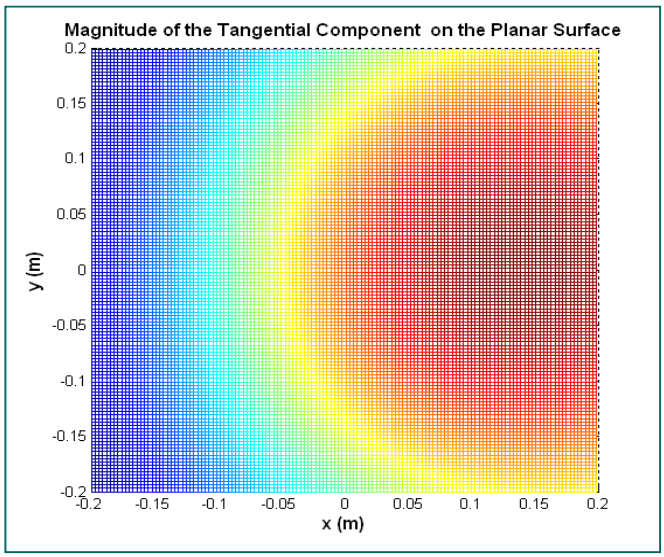

Figure B.5: Tangential field pattern of a horn antenna placed at an offset of 200mm from the center of the surface with an angle of inclination equal to 30º. d=660mm

It is the mark of an educated mind to be able to entertain a thought without accepting it.
Aristotle

REFERENCES

[1]. D. G. Berry, *et al.*, " *The Reflectarray Antenna*", IEEE Trans. Antennas Propagat., vol. AP-11, pp. 645-651, Nov. 1963.

[2]. H. Legay, Y. Cailloce, O. Vendier, G. Caille, J. P. Carrier, M. Lathi, J. P. Polizzi, U. Oestermann, P. and N. Raveu, *"Satellite antennas based on MEMS tunable reflectarrays,"* Proc. Antennas and Propagation, EuCAP 2007, pp. 1-6, Nov. 11-16, 2007.

[3]. R. E. Munson, H. Haddad, and J. Hanlen, *"Microstrip reflectarray antenna for satellite communication and RCS enhancement or reduction,"* US Patent 4684952, Aug. 1987.

[4]. D. M. Pozar and S. D. Targonski, *"A shaped-beam microstrip patch reflectarray,"* IEEE Trans. Antennas Propagat., vol. 47, pp. 1167–1173,Jul. 1999.

[5]. Kelkar, "FLAPS: Conformal phased reflecting surfaces," Proc. IEEE National Radar Conf., Los Angeles, CA, pp. 58–62, Mar. 1991.

[6]. J. Huang and R. J. Pogorzelski, *"A Ka-band microstrip reflectarray with elements having variable rotation angles,"* IEEE Trans. Antennas Propagat., vol. 46, pp. 650–656, May 1998.

[7]. R. D. Javor, X. D. Wu, and K. Chang, *"Design and performance of a microstrip reflectarray antenna,"* IEEE Trans. Antennas Propagat., vol. 43, pp. 932–939, Sept. 1995.

[8]. A. Rashid, H. Aubert, "Modeling of Electromagnetic Coupling in Finite Arrays Using Scale Changing Technique", *Progress In Electromagnetics Research Symposium,* Cambridge, USA, 5-8 Jul. 2010,

[9]. M. Riel and J.-J. Laurin, *"Design of an electronically beam scanning reflectarray using aperture-coupled elements,"* IEEE Trans. Antennas Propag., vol. 55, no. 5, pp. 1260–1266, May 2007.

[10]. Hum, S. V., M. Okoniewski, and R. J. Davies*, "Modeling and design of electronically tunable reflectarrays",* IEEE transactions on Antennas and Propagation, vol. 55, no. 8, pp. 2200-2210, Aug. 2007.

[11]. R. Romanofsky, *"Special issues and features of a scanning reflectarray antenna based on ferroelectric thin film phase shifters,"* Proc. European Conf. Antennas Propag. Nice, France, Nov. 2006.

[12]. A. Moessinger, R. Marin, J. Freese, S. Mueller, A. Manabe, and R. Jakoby, *"Investigations on 77 GHz tunable reflectarray unit cells with liquid crystal," Proc*. 1st European Conf. Antennas Propag. Nice, France, Nov. 2006.

[13]. M. Chaharmir, J. Shaker, M. Cuhaci, and A.-R. Sebak, *"Novel photonically-controlled reflectarray antenna,"* IEEE Trans. Antennas Propag., vol. 54, no. 4, pp. 1134–1141, Apr. 2006.

[14]. E. Perret, H. Aubert, and H. Legay, *"Scale-changing technique for the electromagnetic modeling of MEMS-controlled planar phase shifters,"* IEEE Trans. Microw. Theory Tech., vol. 54, pp. 3594–3601, Sep. 2006.

[15]. S. Hum, G. McFeetors, and M. Okoniewski, *"Integrated MEMS reflectarray elements,"* Proc. 1st European Conf. Antennas Propag, Nice, France, Nov. 2006.

[16]. H. Legay, B. Pinte, E. Girard, R. Gillard, M. Charrier, and A. Ziaei, "A low loss and steerable reflectarray antenna in Ka band," in *Proc. 27th ESA Antenna Technol. Worksh. Innovative Periodic Antennas*, Santiago de Compostela, Spain, 2004, pp. 281–288.

[17]. D. M. Pozar and D. H. Schaubert, *"Analysis of an infinite array of rectangular microstrip patches with idealized probe feeds,"* IEEE Trans. Antennas Propagat., vol. 32, pp. 1101-1107, Oct. 1984.

[18]. C. Wan and J. A. Encinar, "Efficient computation of Generalized Scattering Matrix for analyzing multilayered periodic structures," *IEEE Transactions on Antennas and Propagation*, vol. 43, pp. 1233-1242, Oct. 1995.

[19]. T. Cwik and R. Mittra, "The effects of the truncation and curvature of periodic surfaces: A strip grating," *IEEE Trans. Antennas Propagat.*, vol. 36, pp. 612-622, May. 1988.

[20]. J. Huang and J. A. Encinar, *Reflectarray Antennas*, New Jersey, USA: IEEE Press, 2007.

[21]. R. Mittra, H. C. Chan, and T. Cwik, "Techniques for Analyzing Frequency Selective Surfaces-a review," *Proc. IEEE,* vol.76, pp. 1593-1614, Dec. 1988.

[22]. W.L.Ko and R. Mittra, "Scattering by a truncated periodic array," *IEEE Trans. Antennas Propagat.*, vol. 36, pp. 496-503, Apr. 1988.

[23]. R. G. Kouyoumjian and R. Mittra, *"The geometrical theory of diffraction and its application," Numerical and Asymptotic Techniques in Electromagnetics*, Ed. Berlin, Germany: Springer, Verlag, 1975.

[24]. P. Y. Ufimtsev, "Elementary edge waves and the physical theory of diffraction," *Electromagnetics*, vol. 11, no. 2, pp. 125–159, Apr.Jun. 1991.

[25]. G. A. Thiele and G. A. Newhouse, "A hybrid technique for combining moment methods with the geometrical theory of diffraction," *IEEE Trans. Antennas Propag.*, vol. AP-23, pp. 551–558, Jul. 1975.

[26]. T.K. Sarkar, E. Arvas, S. M. Rao, "Application of FFT and the Conjugate Gradient Method for the solution of electromagnetic radiation from electrically large and small conducting bodies" *IEEE Trans. Antennas Propagat.*, vol. 33, pp. 635-640, 1986

[27]. R. Coifman, V. Roklin, and S. Wandzura, "The fast multipole method for the wave equation: a pedestrian prescription," *IEEE Antenna Propagat. Mag.*, vol. 35, pp. 7–12, Jun. 1993.

[28]. J. Song, C. Lu, W. C. Chew, "Multilevel fast multipole algorithm for electromagnetic scattering by large complex objects," *IEEE Trans. Antennas Propagat.*, vol. 45, pp. 1488–1493, Oct. 1997.

[29]. E. Suter, J. Mosig, "A subdomain multilevel approach for the MoM analysis of large planar antennas," *Microw. Opt. Technol. Lett.*, vol. 26, no. 4, pp. 270–277, Aug. 2000.

[30]. G. Tiberi, A. Monorchio, G. Manara, R. Mittra, "A spectral domain integral equation method utilizing analytically derived characteristic basis functions for the scattering from large faceted objects," *IEEE Trans. Antennas Propagat.*, vol. 54, pp. 258-2514, Sept. 2006.

[31]. R. Mittra, Ji-Fu Ma, E. Lucente, A. Monorhio, **"**CBMOM – an iteration free MoM approach for solving large multiscale EM radiation and scattering problems**,** "*IEEE AP-S International Symposium and USNC/URSI National Radio Science Meeting*, Vol. 2B, pp. 2-5, Jul. 2005

[32]. E. Lucente, A. Monorchio, R. Mittra, **"**Generation of Characteristic Basis Functions by using Sparse MoM Impedance Matrix to Construct the Solution of Large Scattering and Radiation Problems**,"** *IEEE AP-S International Symposium and USNC/URSI National Radio Science Meeting*, pp. 4091-4094, 2006.

[33]. D. Pilz and W. Menzel, "Full wave analysis of a planar reflector antenna", *Asia Pacific Microwave Conference*, Dec. 1997.

[34]. T. Itoh, *Numerical techniques for microwave and millimeter wave passive structures*, John Wily and Sons, New York, USA, 1989.

[35]. H. Aubert "The Concept of Scale-Changing Network in the Global Electromagnetic Simulation of Complex Structures," *Progress In Electromagnetics Research B*, vol. 16, page 127-154, 2009.

[36]. G. Conciauro, M. Guglielmi, R. Sorrentino, *Advanced Modal Analysis*, John Wiley & Sons, New York, USA, 1999.

[37]. D. Voyer, H. Aubert, J. David, "Scale-Changing Technique for the Electromagnetic Modeling of Planar Self-similar tructures," *IEEE Trans. Antennas Propagat*., Vol. 54, Issue 10, pp. 2783-2789, Oct. 2006.

[38]. D. Voyer, H. Aubert, J. David, "Radar Cross Section of Self-similar Targets," *Electronics Lett.*, vol. 41, no. 4, pp. 215-217, Feb. 2005.

[39]. D. Voyer, H. Aubert, J. David, "Radar Cross Section of discrete self-similar objects using a recursive electromagnetic analysis", *IEEE AP-S International Symposium and USNC/URSI National Radio Science Meeting, Monterey*, California, USA, 20-26 June 2004, Conference Proceedings volume 4, pp. 4260-4263.

[40]. E. Perret, H. Aubert, "Scale-Changing Technique for the computation of the input impedance of active patch antennas," *IEEE Antennas Wireless Propagat. Lett.*, vol. 4, pp. 326 – 328, 2005

[41]. E. Perret, Aubert, H., Legay, H., "Scale-Changing Technique for the Electromagnetic Modelling of MEMS-controlled Planar Phase-shifters," *IEEE Trans. Microwave Theory and Tech.*, Vol. 54, Issue 9, pp. 3594 – 3601, Sept. 2006.

[42]. F.A.Tahir, A. Rashid, E.B. Tchikaya, H. Aubert, "Full Wave Analysis of Planar Structures using Scale Changing Technique under Feed Horn Excitation", *Antennas and Propagation Conference* (LAPC), Loughborough, UK, 8-9,pp.445-448, Nov, 2010

[43]. F. A. Tahir, A. Aubert, "Scattering analysis of periodic microstrip reflectarrays using scale changing technique," *The Applied Computational Electromagnetics Symposium*, Virginia, USA, March 27-31, 2011.

[44]. A. Rashid, " Electromagnetic Modeling of Large and Non-uniform Planar Array Structures using Scale Changing Technique (SCT)", PhD Thesis, LAAS-CNRS Toulouse, France, Jul. 2010.

[45]. E. B. Tchikaya, F. Khalil, F. A. Tahir, H. Aubert, "Multi-scale approach for the electromagnetic simulation of finite size and thick frequency selective surfaces," *Progress In Electromagnetics Research* M, vol. 17, pp. 43-57, Feb. 2011.

[46]. C. Wan and J. A. Encinar, "Efficient computation of Generalized Scattering Matrix for analyzing multilayered periodic structures", *IEEE Transactions on Antennas and Propagation*, Vol. 43, pp. 1233-1242, October 1995.

[47]. J. A. Encinar, "Printed circuit technology multilayer planar reflector and method for the design thereof", *European Patent EP 1120856*, Jun. 1999.

[48]. J. A. Encinar , " Design of two - layer printed reflectarrays using patches of variable size , " *IEEE Transactions on Antennas and Propagation*, Vol. 49 , No. 10 , pp. 1403 – 14010 , Oct. 2001.

[49]. J. A. Encinar and J. A. Zornoza , " Broadband design of three - layer printed reflectarrays , " *IEEE Transactions on Antennas and Propagation*, Vol. 51, No. 7 , pp. 1662 – 1664 , July 2003

[50]. A. W. Robinson , M. E. Bialkowski , and H. J. Song , " An X - band passive reflect – array using dual - feed aperture - coupled patch antennas, " *Asia Pacific Microwave Conference* , pp. 906 – 909 , Dec. 1999.

[51]. M. G. Keller , M. Cuhaci , J. Shaker , and A. Petosa , A. Ittipiboon , and Y. M. M. Antar ," Investigations of Novel Reflectarray Configurations, "*Symposium on Antenna Technology and Applied Electromagnetics* , pp. 299 – 302 , 2000.

[52]. N. Marcuvitz, 'Waveguide Handbook' McGra-Hill, 1951.

[53]. R. Dubrovka, J. Vazquez, C. Parina and D. Moor, "Equivalent circuit method for analysis and synthesis of frequency selective surfaces", IEE Proc. Microw. Antennas Propag., vol. 153, no. 3, pp.213-220, Jun. 2006.

[54]. C.K. Lee, B.Sc., and R. J. Langley, "Equivalent-circuit models for frequency-selective sufaces at oblique angles of incidence", IEE Proceedings, vol. 132, no. 6, Oct. 1985.

[55]. M. Ohira, H. Deguchi, M. Tsuji and H. Shigesawa, "Analysis of frequency selective surfaces with arbitrarily shaped element by equivalent circuit model", Electronics and Communications in Japan, Part 2, vol. 88, no. 6, 2005.

[56]. R. J. Langley and e. A. Parker, "Equivalent circuit model for arrays of square loops", Electronic Letters, vol 18, no. 7, Apr. 1982

[57]. C.A. Balanis, "Antenna Theory: Analysis and Design", 3rd Ed., Jhon wiley and Sons, 2005.

[58]. H. Legay, *et al*.,"A steerable reflectarray antenna with MEMS controls," IEEE Int. Phased Array Syst. Technol. Symp., pp. 494-499, Oct. 14-17, 2003.

[59]. H. Legay, *et al*., "MEMS controlled linearly polarised reflectarray elements", 12th Int. Antenna Technol. Appl. Electromagn. Symp., Montréal, QC, Canada, Jul. 2006, pp. 16-19.

[60]. H. Legay, *et al*., "A steerable reflectarray antenna with MEMS controls," IEEE Int. Phased Array Syst. Technol. Symp., pp. 494-499, Oct. 14-17, 2003.

[61]. C. L. Goldsmith, Z. Yao, S. Eshelman, and D. Denniston, "Performance of low-loss RF MEMS capacitive switches", IEEE Microwave and Guided Wave Letters, vol. 8, no. 8, pp. 269-271, Aug. 1998.

[62]. D. Peroulis, S. Pacheco, K. Sarabandi, and L. P. B. Katehi, " Tunable lumped components with applications to reconfigurable MEMS filters", IEEE Int. Microw Symp. Digest, vol. 1, pp. 341-344, May 20-25, 2001.

[63]. M. Nadarassin, H. Aubert and H. Baudrand, "Analysis of Planar Structures by an Integral Approach using Entire Domain Trial Functions, "IEEE Trans. Microw. Theory Tech., vol. 43, no. 10, pp. 2492-2495, Oct. 1995.

[64]. A. Carton, C. G. Christodoulou, C. Dyck, and C. Nordquist, "Investigating the impact of Carbon Contamination on RF MEMS Reliability", IEEE Antennas and Propagation International Symposium, Jul. 2006 pp.193-196.

[65]. D. Voyer, "Modélisation Electromagnétique par Changement d'Echelle appliquée aux Structures Fractales Planaires", *Thèse Laboratoire d'Electronique de l'ENSEEIHT,* Toulouse France, 2005.

[66]. R. E. Collin, "*Field Theory of Guided Waves"*, IEEE Press, Second Edition, 1991.

[67]. D. Cadoret, A. Laisne, R. Gillard, and H. Legay, "Design and measurement of new reflectarray antenna using microstrip patches loaded with slot," *Electronic Letters*, vol. 41, No. 11, 623-624, May 2005.

[68]. E. Perret, "Application de l'Approche par Changements d'Echelle aux Circuits Planaires Hyperfréquences", *Thèse Laboratoire d'Electronique de l'ENSEEIHT,* Toulouse, France, 2005.

[69]. S.W. Lee, W.R. Jones, J. J. Campbell, "Convergence of numerical solutions of iris-type discontinuity problems", *IEEE Transactions on Microwave Theory and Techniques*, vol. MTT-19, No. 6, June 1971, pp.528-536.

[70]. H. Aubert and H. Baudrand : *L'Electromagnétisme par les Schémas Equivalents*, Cepaduès Editions, Collection Polythèque, France, 2003.

[71]. www.cst.com

[72]. www.feko.info

[73]. www.mentor.com/electromagnetic-simulation

[74]. F. Khalil, C. Barrios-Hernandez, A. Rashid, H.Aubert et al. *"Parallelization of the Scale Changing Technique in Grid Computing environment for the Electromagnetic Simulation of Multi-scale Structures",* Wiley International Journal of Numerical Modeling, vol. 24, pp. 57-76, 2010.

[75]. www.ansoft.com/products/hf/hfss/

Women are made to be loved, not understood.
Oscar Wilde

PUBLICATIONS

International Journal Publications

- F.A. Tahir, H. Aubert and E. Girard, *"Equivalent Electrical Circuit for Designing MEMS-Controlled Reflectarray Phase Shifter"*, Progress in Electromagnetic Research, Jan. 2010, PIER 100, pp. 1-12.
- F.A. Tahir, H. Aubert and E. Girard, *"Optimization of MEMS-Controlled Reflectarray Phase Shifter Cell"*, IET Microwaes, Antennas and Propagation, vol. 5, Iss. 3, pp. 271-276, Feb 2011
- E. B. Tchikaya, F. Khalil, F. A. Tahir, and H. Aubert, *"Multi-scale approach for the electromagnetic simulation of finite size and thick frequency selective surfaces", Progress In Electromagnetics Research* M, vol. 17, pp. 43-57, Feb. 2011.
- F. A. Tahir and H. Aubert, *"Electromagnetic Modeling of Microstrip Reflectarrays using Scale Changing Technique"*, Under Review: IEEE Transactions on Antennas and Propagation.

International Conference Publications

- F.A.Tahir, A. Rashid, E. B. Tchikaya, and H.Aubert, *"Full Wave Analysis of Planar Structures using Scale Changing Technique under Feed Horn Excitation"*, IEEE *Antennas and Propagation Conference* (LAPC), pp.445-448, 8-9 Nov 2010, Loughborough, UK
- F. A. Tahir, and H. Aubert, "*EM Modeling of periodic microstrip reflectarrays using scale changing technique"*, IEEE International Symposium on Antennas, Propagation and EM Theory (ISAPE), pp. 905-908, Nov 29- Dec 2, 2010, Guangzhou, China
- Euloge Budet Tchikaya, Farooq Ahmad Tahir, and Hervé Aubert, *"Full Wave Analysis of Finite Uniform Metallic Grid FSS under Oblique Incidence Using Scale Changing Technique"*, Progress in Electromagnetic Research Proceedings, 689-692, March 20-23, 2011, Marrakesh, Morocco
- F. A. Tahir, and H. Aubert, *"Scattering analysis of periodic microstrip reflectarrays using scale changing technique"*, Progress in Applied Computational Electromagnetics Conference, pp. 677-622, March 27-31, 2011, Virginia, USA.
- F. A. Tahir, and H. Aubert, *"Efficient Electromagnetic Simulation of Periodic Microstrip Reflectarrays",* 5th IEEE European Conference on Antennas and Propagation, pp. 1503-1505, Apr 11-15, 2011, Rome, Italy
- F.A. Tahir, H. Aubert and E. Girard , *"Equivalent Electrical Circuit Model for Design and Optimization of MEMS-Controlled Reflectarray Phase Shifter Cells"*, 5th IEEE European Conference on Antennas and Propagation, pp. 257-260, Apr 11-15, 2011, Rome, Italy.

National Conference Publications

- F. A. Tahir, and H. Aubert, *"Phase Shifter Cell Optimization for MEMS-based Reflectarrays using Equivalent Circuit Model"*, National RF Engineering and Microwave Conference (JNM-2011), May 18-20, 2011, Brest, France.

Author's Biography

FAROOQ AHMAD TAHIR was born in Faisalabad, Pakistan, in April 1983. He completed his FSc examination in 2001 and received silver medal and prestigious Quaid-e-Azam scholarship for BS Engineering Studies. He received BS degree in Electrical Engineering from the University of Engineering and Technology Lahore, Pakistan in 2005. From April 2006 to April 2007, he served as a faculty member at the Electrical Engineering Department of the "University of Lahore", Pakistan. He received his MS degree in Telecommunication, RF and Microelectronics (TRFM) in 2008 from the University of Nice, Sophia-Antipolis, France.

From September 2008 to September 2011, FAROOQ was working towards his PhD degree in the Research Group "Micro and Nanosystems for Wireless Communications" at the Lab LAAS-CNRS (Laboratoire d'Analyse et d'Architectures des Systèmes-Centre National de la Recherche Scientifique) Toulouse, France. He received his PhD degree (with high honors) in September 2011 from National Polytechnique Institute of Toulouse (INPT), University of Toulouse, France. The thesis has been nominated for the "Best Thesis Prize of the Year 2011" at National Polytechnique Institute Toulouse, University of Toulouse France.

His research interests include design and implementation of microwave integrated circuits and reflectarray antennas, computational electromagnetics, electromagnetic modeling of complex (multi-scale) antenna structures & reconfigurable circuits for RF and microwave applications, modeling and implementation of electronically tunable microstrip antennas and high performance computing by Scale Changing Technique.

During the thesis, author was affiliated to IEEE TAP (Transactions on Antennas and Propagation) Society and the IEEE AP-S (Antennas and Propagation Symposium) society. He was a regular reviewer for the international journal of "Progress in Electromagnetic Research (PIER)".

To send an e-mail: tahir463@gmail.fr